

'Questions are the answers we might need'

Noel Gallagher – Oasis



**Unravelling xylem-transported CO<sub>2</sub> dynamics in poplar branches and leaves  
using positron emission tomography and autoradiography**

**Ontrafelen van het dynamisch gedrag van xyleem-getransporteerd  
CO<sub>2</sub> in takken en bladeren van populier gebruikmakende van  
positron emissie tomografie en autoradiografie**

ir. Jens Mincke

Promotors: Prof. Dr. ir. Kathy Steppe, Prof. Dr. Stefaan Vandenberghe

Thesis submitted in fulfilment of the requirements for  
the degree of doctor (PhD) of Bioscience Engineering



Plants and Crops - Electronics and Information Systems  
Faculty of Bioscience Engineering - Faculty of Engineering and Architecture

Academic year 2019 – 2020

**Illustration on cover:**

Autoradiographic image of a poplar branch that has taken up a radioactive solution containing dissolved  $^{11}\text{C}$ . The lower part of the branch was in a dark container whereas the upper part was illuminated with photosynthetically active light. Branch parts showing the brightest colour (white and yellow) have assimilated the  $^{11}\text{C}$ -tracer from the sap.

**To be cited as**

Mincke, J. (2020) Unravelling xylem-transported  $\text{CO}_2$  dynamics in poplar branches and leaves using positron emission tomography and autoradiography, PhD thesis, Ghent University, Belgium.

**Funding**

Jens Mincke was supported by a fellowship of Research Foundation - Flanders (FWO-Vlaanderen, PhD-SB grant G.0319.13N).

**ISBN**

978-94-6357-290-3

*The author and the promoters give the authorisation to consult and copy parts of this work for personal use only. Every other use is subject to the copyright laws. Permission to reproduce any material contained in this work should be obtained from the author.*

### **Members of the Jury**

Prof. Dr. ir. Pascal Boeckx (Chairman)

Department of Green Chemistry and Technology

Faculty of Bioscience Engineering, Ghent University

Prof. Dr. ir. Wouter Maes (Secretary)

Department of Plants and Crops

Faculty of Bioscience Engineering, Ghent University

Prof. Dr. ir. Roel Van Hohen

Department of Electronics and Information Systems

Faculty of Engineering and Architecture, Ghent University

Dr. ir. Roberto L. Salomón

Department of Plants and Crops

Faculty of Bioscience Engineering, Ghent University

Prof. Dr. David T. Hanson

Department of Biology

University of New Mexico

### **Promoters**

Prof. Dr. ir. Kathy Steppe

Laboratory of Plant Ecology

Department of Crops and Plants

Faculty of Bioscience Engineering

Ghent University

Prof. Dr. Stefaan Vandenberghe

Medical Image and Signal Processing

Department of Electronics and Information Systems

Faculty of Engineering and Architecture

Ghent University

### **Dean of the Faculty**

Prof. Dr. ir. Marc Van Meirvenne

### **Rector of the University**

Prof. Dr. ir. Rik Van de Walle



# A

## ACKNOWLEDGMENTS

Wat is de tijd voorbijgevlogen... Na alle etappes te hebben doorstaan vanaf het experimenteren, schrijven en verbeteren zijn we aanbeland bij de laatste stadium, het dankwoord, ofte het hoofdstuk dat als laatste geschreven wordt maar toch helemaal bovenaan staat. De verklaring: het werk dat hierin beschreven staat kon onmogelijk verzet zijn door één man. Ik zou hierbij dan ook iedereen uitdrukkelijk willen bedanken die me heeft bijgestaan tot het verwezelijken van dit boekje.

Allereerst wil ik mijn beide promotoren prof. Stefaan Vandenberghe en prof. Kathy Steppe prijzen voor het aanreiken van de mogelijkheid tot het uitvoeren van een doctoraat. Ik ben vooral opgelucht dat ik vijf minuten na mijn mondeling examen bij Stefaan nog eens mijn hoofd om de deur stak om te melden dat ik geïnteresseerd was in het uitvoeren van een PhD. En toeval of niet, er was recent een samenwerking met Kathy op poten gezet die zowel het biomedische als het bio-ingenieurs aspect bevatte. Hoewel ik nog geen praktische ervaring had met plantwetenschappen was Kathy haar aanstekelijk enthousiasme genoeg om van het vervolg intussen geschiedenis te maken.

Aan allebei, heel erg bedankt voor de talloze inzichten, het nalezen en verbeteren van mijn manuscripten, en de vele babbels en constructieve vergaderingen.

Met betrekking tot het beeldvormingsaspect gaat evenveel lof naar prof. Christian Vanhove en dr. Benedict Descamps (i.e. Chris en Bene) van Infinity waar ik al mijn experimenten heb mogen uitvoeren. Heel erg bedankt voor mijn introductie in de wondere wereld van positron beeldvorming alsook om toe te staan dat ik de PET-ruimte met behulp van speciale belichting meermaals mocht omtoveren tot een *kabberdoeske*. Door jullie deskundigheid eindigden nagenoeg alle experimenten succesvol. Ik wens hierbij ook een grote bos pluimen op de hoed steken van de cyclotron afdeling en in het bijzonder Jan Courty. Het eindeloos puzzelen in je werkagenda om radioactief CO<sub>2</sub> te voorzien werd hierbij ten zeerste geapprecieerd. Daarnaast wil ik ook mijn dank toe'lichten' aan de knappe koppen van Molecubes omdat ik gepast en vooral ongepast telkens de werkruimte tijdelijk mocht donker maken voor mijn experimenten.

Mijn liefste collegae op de Coupure en het UZ mogen zeker niet mankeren in deze lofbetuiging, onder andere omdat jullie beurtelings mijn afwezigheid moesten verwerken wanneer ik op de andere vakgroep vertoefde en misschien ook omwille van de grapjes (van om het even welke aggregatietoestand) waarmee ik jullie belaagde. Het gemis was wederzijds ;). Hierbij is een ereplaats weggelegd voor volgende top dames: Inge, Ann, Pui Yi, en Saskia. Dikke merci voor me te helpen het administratieve bos door de bomen te zien en vooral voor de gezellige babbels! Op gelijk niveau komen de super heren Philip, Geert, Erik en Jurgen! Bedankt voor jullie vakkundigheid, deze is bewonderenswaardig en maken van MacGyver een hobbykluns! Over naar de sloebers Jonas (stonks ↑) en Jonathan (DAB-lord), jullie zijn de max (i.e. level 4☺ maar vooral irl) en het was ronduit jolig om met jullie een eiland te vormen. Hetzelfde geldt voor Jeroen en Sarah die het eiland vervulde en ook met fierheid een groene das droegen op de eerste lentedag. Ook Fran verdient een speciale vermelding, je coaching en alle daden die je verzette voor van de labogroep een (bowling)ploeg te maken waren telkens geslaagd! Furthermore, I would like to thank the other desk sitters (old and new) to make the lab a nice place, these are: Bart, Ben (jouje), Hans, Jōnas (Apple boy), Linus (proficiat!), Michiel (ping pong), (papa) Niels, Richa(a)rd, Selwyn (Fiji master), Simon en Willem (de volwaardig nieuwste eilandaanwinst) as well as the Spanish Conquistadoras Adrián, Carmen, Jesús and Roberto. Op naar het zuiden van Gent. Kim, samen starten in een voor ons allebei onbekende vakgroep was aangenamer dankzij jou. Ratten een hersentrauma bezorgen om



ze daarna spelletjes te laten spelen was dan weer jou manier om ermee om te gaan, al moet ik bekennen dat planten in een PET-scanner steken ook niet alledaags is. Misschien daarom dat men ons apart gezet heeft? Thibault, Willeke en Pieter, door jullie voelde ik me meteen thuis op het 5<sup>de</sup> verdiep van de B-blok. Na jullie (voor Pieter tijdelijk buitenlands) vertrek was het niet meer hetzelfde. Al moet ik bekennen dat de nieuwe generatie jullie waardig is. It was my pleasure to traverse Ghent for both the old and the new generation: Ashkan, Carmen, Charlotte (de kalmheid zelve), Emma (de echte kalmheid zelve), Ester, Gert, Gregor, Gwenaëlle, Jens, Jolan (EMG auto man), Lara, Mariële (selbstverständlich), Marec (Tatratea), Milan, Nathalie, Paulo (almost there man!!), Prakash, Radek, Stijn en Tim (Icetea Green addict). Daarnaast wil ik ook de collega's van BioMMeda aan de overkant van de gang bedanken en in het bijzonder Gerlinde en Mathias! Altijd veel lachen en opvallend weinig stiltes in jullie bijzijn! Boodschap aan iedereen: ik vond het zalig dat ik jullie 'zo nu en dan' eens mocht storen met mijn gezever.

Naast mijn toffe collegas kon ik gegarandeerd ook mijn hoofd verzetten bij mijn doldwaze vriendenbende waar plezier maken zegevierd, absurditeit koning is en Vandewalle "den besten" is (regelet). Op ski/surfreis vertrekken met Dré, Jeroen, Gert, Tijs, Tim, Stef, Giel-Jan, Jano, Timon, Hans en Ruark is dan ook iets om naar uit te kijken wanneer de vorige gedaan is. Daarnaast mag team Brakel ook niet ontbreken, zijnde Simon, Thibaut Sanne en Jo. Onze samenkomsten zijn misschien limited editions maar telkens memorabel! Finaal wil ik lego/gitaar virtuoos Brecht prijzen. Een toevallig gesprek in de gang mondde gegarandeerd uit in minimum een half uur leuteren, waarvoor dank.

Ik heb ook het genoeg gehad om in een bijzonder warm gezin opgegroeid te zijn met fantastische ouders, grootouders en schoonfamilie. Bedankt mama en papa voor de onvoorwaardelijke steun en de vele schouderklopjes, jullie hebben mij altijd alle kansen gegeven waarvoor ik jullie heel erg dankbaar ben! De bezoekjes aan het thuisfront zijn misschien beperkt, maar altijd een schot in de roos. Alvorens terug naar Gent te vertrekken heb ik dan ook altijd minstens een uur mijn jas aan omdat we niet kunnen stoppen met kletsen. Mijn double trouble counterpart, Stein. Niemand kan zich voorstellen wat het is om een *bro* te hebben waarmee je echt al je passies en interesses deelt gedurende je volledige leven, behalve jij. Ik had me deze two-player life hack niet zaliger kunnen bedenken! ;) 2020 zal spannend worden voor ons allebei, een nieuwe wind

na het doctoraat en veel optredens en festivals die we vanaf nu niet meer verlaten zonder memorabilia.

Pas op het laatste speel ik mijn joker-kaart kwijt aan mijn wonder woman. Lotte, altijd ben je er voor me, mijn schouder door dik en dun, ook wanneer het doctoraat minder goed opschoot. Ik wil je op een voetstuk plaatsen voor alle opbeurende woorden, onze onverstaaanbaar onnozele momenten, je eindeloze geduld en de vele attenties die ik kreeg als ik eventjes naar beneden kwam tussen het schrijven door, maar vooral bedankt voor steeds in mij te geloven! Je bent een TOP vrouwtje!!

Januari 2020, Gent

Jens Mincke

# T

## TABLE OF CONTENTS

<b>Table of Contents</b> .....	<b>xi</b>
<b>List of abbreviations and symbols</b> .....	<b>xv</b>
<b>1 Introduction and thesis outline</b> .....	<b>1</b>
1.1 Studying the fate of respired CO <sub>2</sub> .....	4
1.2 Basics of positron-based imaging.....	8
1.3 Thesis outline .....	10
<b>2 Guide to plant-PET imaging using <sup>11</sup>C</b> .....	<b>13</b>
2.1 Introduction and overview.....	15
2.2 Experimental design of plant-PET studies .....	15
2.2.1 Communication and planning .....	15
2.2.2 Production and formulation of radiotracers.....	17
2.2.3 Working safely with gaseous radioactivity.....	19
2.2.4 PET data acquisition.....	22
2.2.5 Image reconstruction.....	24

2.2.6	Image processing and quantification.....	27
2.3	Conclusion.....	30
<b>3</b>	<b>High-resolution <i>in vivo</i> imaging of xylem-transported CO<sub>2</sub> in leaves based on real-time <sup>11</sup>C-tracing.....</b>	<b>33</b>
3.1	Abstract.....	35
3.2	Introduction.....	36
3.3	Materials and methods.....	38
3.3.1	Plant material.....	38
3.3.2	Experimental setup and <sup>11</sup> C-labelling.....	39
3.3.3	<sup>11</sup> C-imaging techniques.....	41
3.3.4	Manipulation experiments.....	43
3.4	Results.....	43
3.4.1	Microclimate.....	43
3.4.2	Images.....	45
3.4.3	Tracer dynamics.....	46
3.5	Discussion.....	46
3.5.1	<sup>11</sup> C-based tracing of xylem CO <sub>2</sub> transport and fixation.....	46
3.5.2	Why should we measure xylem CO <sub>2</sub> transport in plants?.....	49
3.5.3	The power of imaging <sup>11</sup> C-labeled compounds in plant research.....	50
3.6	Conclusion.....	51
<b>4</b>	<b>Assimilation of xylem-transported CO<sub>2</sub> by woody tissue photosynthesis unravelled through <sup>11</sup>C-positron autoradiography enforced with <sup>13</sup>C-labelling....</b>	<b>53</b>
4.1	Abstract.....	55
4.2	Introduction.....	56
4.3	Materials and methods.....	58
4.3.1	Plant material.....	58
4.3.2	Experimental set-up and radioactive <sup>11</sup> C- and <sup>18</sup> F-labelling.....	60
4.3.3	Positron autoradiography.....	62
4.3.4	Image analysis.....	62
4.3.5	Manipulation experiments.....	65
4.3.6	Activity profile plot processing.....	66
4.3.7	Experimental set-up <sup>13</sup> C-labelling.....	67

---

4.3.8	Sugar extraction and LC-MS analysis .....	68
4.3.9	Sugar quantification.....	69
4.4	Results .....	70
4.4.1	<sup>11</sup> C positron autoradiographic imaging to assess woody tissue photosynthesis and water transport.....	70
4.4.2	<sup>13</sup> C-sugar analysis .....	72
4.5	Discussion .....	74
4.5.1	Assimilation of xylem-transported CO <sub>2</sub> in woody tissues.....	74
4.5.2	<sup>11</sup> C-autoradiography to visualise assimilation of xylem-transported CO <sub>2</sub> 76	
4.5.3	Effect of light on <i>P<sub>wet</sub></i> dynamics in <i>P. tremula</i> .....	78
4.6	Conclusion .....	79
<b>5</b>	<b>Studying <i>in vivo</i> dynamics of xylem-transported <sup>11</sup>CO<sub>2</sub> using PET.....</b>	<b>81</b>
5.1	Abstract.....	83
5.2	Introduction .....	84
5.3	Materials and methods.....	86
5.3.1	Plant material .....	86
5.3.2	Production and formulation of <sup>11</sup> CO <sub>2</sub> .....	87
5.3.3	Experimental set-up and <sup>11</sup> C-labelling.....	87
5.3.4	PET scanner, image reconstruction and analysis .....	89
5.3.5	Compartmental modelling to compute characteristics of xylem- transported CO <sub>2</sub> .....	92
5.3.6	Data processing and terminology .....	94
5.3.7	Assessing the fate of xylem-transported CO <sub>2</sub> using PET and compartmental modelling .....	95
5.4	Results .....	96
5.4.1	PET images.....	96
5.4.2	Modelling xylem-transported carbon dynamics .....	97
5.5	Discussion .....	99
5.5.1	Plant-PET to unravel dynamics in woody tissue photosynthesis.....	99
5.5.2	Dependency of internal CO <sub>2</sub> fluxes on transport speed .....	101
5.6	Conclusion .....	102

---

<b>6</b>	<b>Conclusions &amp; perspectives .....</b>	<b>105</b>
6.1	Can medical imaging techniques be used to study the dynamic fate of internal CO <sub>2</sub> .....	107
6.2	What is the relevance of xylem-transported CO <sub>2</sub> ? .....	109
6.3	Why should we expand positron-based imaging in plant studies? .....	112
6.4	What are the challenges and future prospects for plant-PET.....	113
	<b>Bibliography.....</b>	<b>115</b>
	<b>Summary .....</b>	<b>137</b>
	<b>Samenvatting .....</b>	<b>143</b>
	<b>Curriculum vitae .....</b>	<b>149</b>

# L

## LIST OF ABBREVIATIONS AND SYMBOLS

$^{11}\text{C}$	Carbon-11 (short-lived isotope)
$^{11}\text{CO}_2$	Short-lived radioactive carbon dioxide
$^{13}\text{C}$	Carbon-13 (naturally occurring stable)
$^{13}\text{CO}_2$	Stable carbon dioxide
$^{13}\text{N}$	Nitrogen-13 (short-lived isotope)
$^{14}\text{CO}_2$	Long-lived radioactive carbon dioxide
$^{14}\text{C}$	Carbon-14 (long-lived isotope)
$^{15}\text{O}$	Oxygen-15 (short-lived isotope)
$^{18}\text{F}$	Fluorine-18 (short-lived isotope)
$^{18}\text{FDG}$	2-Fluoro-2-deoxy-D-glucose (short-lived molecule)

## *Abbreviations and symbols*

---

2D	Two-dimensional
3D	Three-dimensional
4D	Four-dimensional
$a$	Net CO <sub>2</sub> exchange parameter between sap and parenchyma and apoplastic spaces
$A_0$	Starting radioactivity
$A_X$	Photosynthetic assimilation of xylem-transported CO <sub>2</sub>
$A_X^{\%}/CO_{2,X}$	Relative amount of xylem-dissolved CO <sub>2</sub> that is photosynthetically assimilated
$A(t)$	Radioactivity at time $t$
ARQ	Apparent respiratory quotient
a.u.	Arbitrary units
aq	Aqueous
$b$	Net CO <sub>2</sub> exchange parameter between photosynthetic cells and parenchyma and apoplastic spaces
$c$	Net CO <sub>2</sub> exchange parameter between atmosphere and parenchyma and apoplastic spaces
CAM	Crassulacean acid metabolism
Chl	Chlorophyll
[CO <sub>2</sub> ]	CO <sub>2</sub> (g) concentration
[CO <sub>2</sub> *]	Concentration of CO <sub>2</sub> species (CO <sub>2</sub> (aq), HCO <sub>3</sub> <sup>-</sup> and CO <sub>3</sub> <sup>2-</sup> ) dissolved in the sap solution
[CO <sub>2,P&amp;A</sub> ]	CO <sub>2</sub> concentration in xylem and phloem parenchyma and apoplastic spaces
CO <sub>2,X</sub>	Xylem-transported CO <sub>2</sub>
CT	Computed tomography
d	Deuteron



---

Da	Branch segment that was not illuminated
DM	Dry matter
DPG	Dew point generator
e <sup>-</sup>	Electron
$E_A$	CO <sub>2</sub> transport flux from the sap to the atmosphere
$E_A^{\%}/CO_{2,X}$	Relative amount of xylem-dissolved CO <sub>2</sub> that is directed from the sap to the atmosphere via efflux
$F_{H2O}$	Sap flow
FOV	Field of view
$F_T$	CO <sub>2</sub> transport flux through xylem
$F_T^{\%}/CO_{2,X}$	Relative contribution of xylem-dissolved CO <sub>2</sub> to the sap transport flux
g	Gaseous
H <sup>+</sup>	Proton
ICRP	International Commission for Radiation protection
IRGA	Ininfra-red gas analyser
$l$	ROI length
LC-MS	liquid chromatography–mass spectrometry
$L_{CO2}$	Contribution of locally respired CO <sub>2</sub> to $E_A$
LED	Light-emitting diode
LGSO	Lu <sub>0.4</sub> Gd <sub>1.6</sub> SiO <sub>5</sub> :Ce
Li	Branch segment that was illuminated
LOR	Line of response
LYSO	Lu <sub>1.9</sub> Y <sub>0.1</sub> SiO <sub>5</sub> :Ce
MLEM	Maximum Likelihood Expectation Maximisation
MRI	Magnetic resonance imaging
n	Neutron

---

*Abbreviations and symbols*

---

N	Number of measurements
NT <sub>H</sub>	Non-treated leaf halve
OSEM	Ordered Subset Expectation Maximisation
<i>p</i>	Proton
P	P-value (probability value)
PAR	Photosynthetically active radiation
PET	Positron emission tomography
<i>P<sub>wt</sub></i>	Woody tissue photosynthesis
R <sup>2</sup>	Coefficient of determination
RAMLA	Row-action maximum-likelihood algorithm
RH	Relative humidity
ROI	Region of interest
<i>R<sub>S</sub></i>	Respiratory CO <sub>2</sub> flux
RuBisCo	Ribulose-1,5-bisphosphate carboxylase/oxygenase
ΔS	Transport flux to CO <sub>2</sub> (g) storage within tissues
ΔS <sup>%</sup> /CO <sub>2,x</sub>	Relative amount of xylem transported CO <sub>2</sub> that is stored as CO <sub>2</sub> (g) in tissues
SD	Standard deviation
SE	Standard error
SNR	Signal to noise ratio
SOP	Standard operating procedure
SPECT	Single photon emission computed tomography
<i>t</i>	time
<i>t</i> <sub>1/2</sub>	Half-life
<i>T</i> <sub>CO2</sub>	Contribution of xylem-transported CO <sub>2</sub> to <i>E<sub>A</sub></i>
<i>T</i> <sub>C<sub>i</sub></sub> <sup>x</sup>	Amount of tracer in compartment <i>x</i> of ROI <i>i</i>

$T_{c_{total}}$	Total amount of carbon tracer in input ROI
$T_H$	Treated leaf halve
TTC	Time-tracer curve
V	Stem volume
$v_{CO_2}$	Model-estimated CO <sub>2</sub> transport speed in xylem conduits
$v_{CO_2}^*$	Image-estimated CO <sub>2</sub> transport speed in xylem conduits
VOCs	Volatile organic compounds
$\alpha$	Alpha particle
$\beta_0$	Intercept
$\beta_1$	Slope
$\beta^+$	Positron
$\gamma$ -photon	Gamma photon
$\nu_e$	Electron neutrino
$\lambda$	Isotope decay constant



# 1

## INTRODUCTION AND THESIS OUTLINE



Life on Earth can be attributed to the continued thermonuclear events taking place at the heart of a middle-aged, mid-sized star — our sun. Those thermonuclear events produce energy that arrives as sunlight on our planet, where photosynthetic systems have evolved to capture and convert the light energy to chemical energy (Evert *et al.* 2013). In that respect, more than 250 billion metric tons of sugar are produced worldwide each year by photosynthetic conversion of atmospheric carbon dioxide ( $\text{CO}_2$ ) and water ( $\text{H}_2\text{O}$ ) (Fig. 1.1). Multiple photosynthetic pathways exist (Text box 1.1) with leaves being the dominant photosynthetic organ in most  $\text{C}_3$  and  $\text{C}_4$  plants, although photosynthesis can occur in every plant organ, including stems, fruits, flowers, and in some rare cases also roots (e.g. orchids) (Nilsen 1995). Specifically, stems can often be the primary photosynthetic organ in some species from arid and semiarid ecosystems, which remain leafless most of the year (Nilsen 1995; Ávila *et al.* 2014). Additionally, green stems of herbaceous and crassulacean acid metabolism (CAM – Text box 1.1) plants are photosynthetic, nevertheless, the significance of chloroplast presence in woody stems has only recently become clearer (Teskey *et al.* 2008) and will be the focus of this thesis.

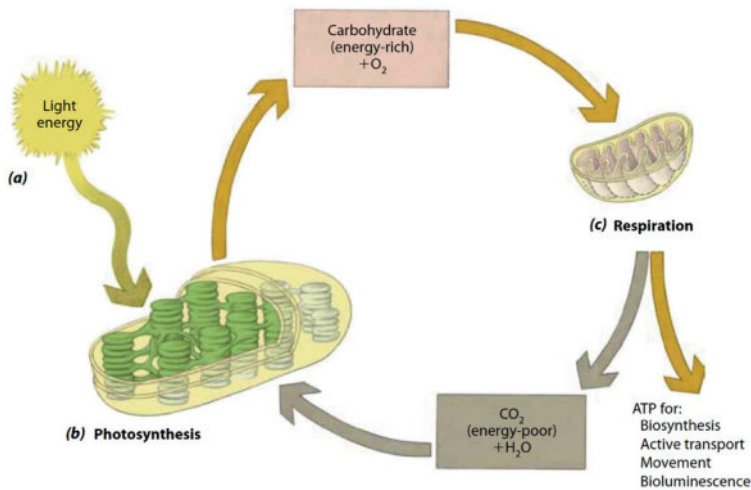


**Figure 1.1** Energy flow in the biosphere (a) The radiant energy of sunlight is produced by nuclear fusion reactions taking place in the sun. (b) Chloroplasts capture the radiant energy of sunlight and use it to convert water and carbon dioxide into carbohydrates, such as glucose, sucrose, or starch. Oxygen ( $\text{O}_2$ ) is released into the air as a by-product of the photosynthetic reactions. (c) Mitochondria, present in eukaryotic cells, carry out the final steps in the breakdown of these carbohydrates and capture their stored energy in ATP molecules. This process, cellular respiration, consumes  $\text{O}_2$  and produces  $\text{CO}_2$  and  $\text{H}_2\text{O}$ , completing the cycling of the molecules. Adapted from Evert *et al.* (2013)

**Text box 1.1 Photosynthetic reactions in C<sub>3</sub>, C<sub>4</sub> and CAM plants**

Due to adaptation to their respective growth conditions over evolutionary time scales, plants have developed different photosynthetic characteristics and can be categorised in three groups according to the followed pathway, i.e. C<sub>3</sub>, C<sub>4</sub> and CAM (crassulacean acid metabolism) (Taiz & Zeiger 2010). Species with C<sub>3</sub> photosynthesis represent the largest group with 85 % of all higher plant species (including almost all tree species) whereas C<sub>4</sub> species account for about 5 %, and CAM species make up the remaining 10 %. C<sub>4</sub> plants are thought to have originated in relatively arid regions, where high temperatures occur in combination with drought stress, whereas desert CAM plants are adapted to drought in arid regions, where day and night temperatures can show drastic swings (although some CAM species occur in tropical rainforests as epiphytes) (Yamori *et al.* 2014).

In all plants, CO<sub>2</sub> diffuses through the stomata and the intercellular air spaces, and eventually arrives in the chloroplast. Regarding C<sub>3</sub> plants, CO<sub>2</sub> is subsequently used for the carboxylation of ribulose-1,5-bisphosphate (RuBP) which is catalysed by the enzyme Rubisco (ribulose-1,5-bisphosphate carboxylase/oxygenase). This reaction produces 3-phosphoglyceric acid (PGA), i.e. a molecule composed of three carbon atoms and the origin for the name of C<sub>3</sub> plants. This reaction occurs in the Calvin cycle where PGA is both used for the regeneration of RuBP and the production of sugars and starch which requires energy in the form of ATP and NADPH. Note that Rubisco can serve as an oxygenase as well as it can catalyse O<sub>2</sub>. This reaction is known as photorespiration and results in release of CO<sub>2</sub>.

C<sub>4</sub> and CAM photosynthesis, on the other hand, have a biochemical CO<sub>2</sub> concentrating mechanism at the catalytic sites of Rubisco which reduces photorespiration (Jenkins *et al.* 1989; Furbank *et al.* 1997). Both C<sub>4</sub> and CAM plants hereby separate the process of CO<sub>2</sub> uptake and the Calvin cycle (C<sub>4</sub> spatially and CAM temporally). Specifically, in C<sub>4</sub> plants CO<sub>2</sub> is first converted into an intermediary molecule (typically malate, i.e. a molecule having four carbon atoms) by phosphoenolpyruvate carboxylase (PEPC). Malate is subsequently transported to the vascular bundle sheath cells where CO<sub>2</sub> is released again which can be processed by Rubisco and have a normal Calvin cycle, as in C<sub>3</sub> plants. The biochemical CO<sub>2</sub> concentrating mechanism in CAM photosynthesis requires separation of the C<sub>3</sub> and C<sub>4</sub>



components in time, compartmentalised within a common cellular environment. During the night, stomata are open, CO<sub>2</sub> is taken up and converted to malate in the vacuoles. During the day, stomata are closed but CO<sub>2</sub> is released internally when light reactions provide energy so that the Calvin cycle can operate. By opening stomata and incorporating CO<sub>2</sub> at night when transpiration rates are low, CAM plants can achieve high water use efficiencies that are three- to six-fold greater than for C<sub>4</sub> and C<sub>3</sub> species, respectively (Yamori *et al.* 2014).

### 1.1 Studying the fate of xylem-transported CO<sub>2</sub>

During cell respiration carbon substrates are oxidized by mitochondria which release CO<sub>2</sub> (Fig. 1.1). Outer tissues of the stem present substantial barriers to radial CO<sub>2</sub> diffusion (Steppe *et al.* 2007), so that locally respired CO<sub>2</sub> builds up in the xylem and dissolves in the sap solution while reaching a substantially higher concentration (often between 3 and 10 % and sometimes up to 26 %, reviewed by Teskey *et al.* 2008) than that in the atmosphere (~ 0.04 %). Xylem CO<sub>2</sub> concentration ([CO<sub>2</sub>]) in the gaseous phase is hereby in equilibrium with CO<sub>2</sub> species (CO<sub>2</sub> (aq), HCO<sub>3</sub><sup>-</sup> and CO<sub>3</sub><sup>2-</sup>) dissolved in the sap solution (sap [CO<sub>2</sub>\*]) (Hari *et al.* 1991; Levy *et al.* 1999; McGuire & Teskey 2004). Upon dissolution in xylem sap, CO<sub>2</sub> is transported upward with the transpiration stream throughout the plant ( $F_T$ ) (McGuire & Teskey 2004). Internally transported (respired) CO<sub>2</sub> can then diffuse to the surrounding xylem parenchyma and apoplastic spaces from where it has two main pathways: it can either radially diffuse into the atmosphere via stem CO<sub>2</sub> efflux ( $E_A$ ) which is facilitated by the [CO<sub>2</sub>] gradient across the xylem – atmosphere or be fixed by chloroplasts present in the bark, xylem rays and pith tissues ( $\Delta S$ ) (McGuire & Teskey 2004; Teskey *et al.* 2008; Bloemen *et al.* 2016b). This latter process can be regarded as a recycling mechanism (brown arrows in Fig. 1.1) and is therefore referred to as stem recycling photosynthesis, as described by Ávila *et al.* (2014). In contrast, another type of CO<sub>2</sub> assimilation by stems exists being net uptake of atmospheric CO<sub>2</sub> realised through stomata present in the epidermis of stems (Comstock & Ehleringer 1990; Nilsen *et al.* 1993; Nilsen 1995) and is referred to as stem net photosynthesis (Ávila *et al.* 2014). Typically, stem recycling photosynthesis is characteristic for stems with low stomatal density or with periderm, and thus generally no net CO<sub>2</sub> assimilation occurs in these stems (Nilsen 1995; Aschan & Pfanz 2003). In this PhD thesis, stem recycling photosynthesis

performed by woody tissues will be investigated and will therefore be referred to as woody tissue photosynthesis ( $P_{wt}$ ), as described by Saveyn *et al.* (2010). Anaplerotic fixation of  $\text{CO}_2$  via CAM or  $\text{C}_4$  photosynthesis (Berveiller & Damesin 2008; Hilman *et al.* 2019) will not be discussed.

Recent research has shown that  $\text{CO}_2$  derived from above- and belowground respiration is transported with the transpiration stream in trees (Teskey *et al.* 2008, 2017; Aubrey & Teskey 2009; Bloemen *et al.* 2013b, 2016a; Steppe *et al.* 2015) thereby representing a second important transport pathway of the plant carbon cycle. However, our understanding of respired  $\text{CO}_2$  and its contribution to each of the carbon fluxes (i.e. upward transport with the sap ( $F_T$ ), assimilated by woody tissue photosynthesis ( $P_{wt}$ ), stored in the sap ( $\Delta S$ ) and efflux to the atmosphere ( $E_A$ )) is still far less advanced than our knowledge of e.g. water transport or leaf photosynthesis (Amthor 2000; Atkin & Macherel 2009; Thornley 2011). A substantial amount might move with the transpiration stream ( $F_T$ ) into foliage (McGuire & Teskey 2002), but the relative proportion of respired  $\text{CO}_2$  that diffuses into the atmosphere ( $E_A$ ) or that is re-assimilated in chlorophyll-containing tissues during xylem transport ( $A_x$ ), is still ambiguous and open for debate. Consequently, recycling of  $\text{CO}_2$  by  $P_{wt}$  is often overlooked with respect to the plant carbon budget as it could pay for local carbon demands (Aschan & Pfanz 2003; Teskey *et al.* 2008; Saveyn *et al.* 2010). Moreover, if a big portion of internally transported  $\text{CO}_2$  is assimilated within trees, then the contribution of leaf photosynthesis is overestimated. Regarding its significance, carbon recycling by  $P_{wt}$  results in a more efficient carbon fixation and, hence, an increase in the overall plant water use efficiency (Cernusak & Marshall 2000; Teskey *et al.* 2008; Wittmann & Pfanz 2008). Moreover, it raises the internal  $\text{O}_2$  concentration, which avoids hypoxia (Pfanz *et al.* 2002; Aschan & Pfanz 2003). Additionally, this unaccounted source of carbon might become important under drought as  $P_{wt}$  is suggested to play a role in the plant hydraulic performance. Under drought, stomatal conductance is reduced not only limiting uptake and assimilation of airborne  $\text{CO}_2$  but also sugar transport (Sevanto 2014). In this way, local assimilation of xylem-transported  $\text{CO}_2$  ( $A_x$ ) to sugars by  $P_{wt}$  could compensate for the reduced long-distance carbohydrate transport from the leaves to the sinks (Sevanto 2014; Cernusak & Cheesman 2015; Vandegehuchte *et al.* 2015). This holds especially for young trees, as because of their smaller carbon storage reserves it is expected that they are more adapted to efficiently recycle  $\text{CO}_2$  given their green shoot tissues and thinner bark layer (Vandegehuchte *et al.* 2015). Furthermore, it

is believed that young trees are able to confer lower xylem vulnerability to embolism via sugar-mediated mechanisms (Schmitz *et al.* 2012; De Baerdemaeker *et al.* 2017).  $P_{wt}$  may as such be regarded as a link between xylem and phloem by contributing to both plant energy as well as hydraulic performance.

Despite the beneficial traits of  $A_x$  by  $P_{wt}$ , there is still uncertainty about this phenomenon as well as about the other internal CO<sub>2</sub> fluxes in woody tissues which might arise from the methodological constraints of the techniques that have been used so far to study xylem-transported CO<sub>2</sub> in relation to stem respiration (Teskey *et al.* 2008). Mainly <sup>13</sup>C- and <sup>14</sup>C-labelling or gas-exchange methods have been applied on petioles, branches or stems. These methods offer limited temporal and/or spatial resolution and therefore hinder estimation of the fate of internally-transported CO<sub>2</sub>, which is important when it boils down to the assessment of their dynamics (Teskey *et al.* 2008). Exactly this is the focus of this PhD thesis.

Radioactive <sup>11</sup>CO<sub>2</sub>-based experiments on branches and leaves of poplar (*Populus tremula* L. and *Populus × canadensis* Moench “Robusta”) have been proposed in combination with medical imaging techniques, such as positron emission tomography (PET) and positron autoradiography. PET has become one of the most common and useful imaging modalities for tumour detection and treatment monitoring of human diseases because of its high diagnostic efficacy and accuracy (Saha 2016). Additionally, this imaging technique is used in preclinical studies on rodents and nonhuman primates for research on drug development linked to e.g. cardiology or neurology (Ametamey *et al.* 2008). Positron autoradiography on the other hand, has increasingly been employed for the analysis of radioactive samples in molecular biology, pharmacology, and receptor binding and quantitative biopsy analysis under PET/CT guidance (Sihver *et al.* 1999; Maguire *et al.* 2012; Zanzonico 2012) due to its high spatial resolution (~ 0.05 mm). Note that this is higher than the anatomical data provided by CT (~ 0.5 mm). Both of the postiron-based technique can be applied in plant science by means of a non-invasive *in vivo* approach, making them very promising to study the dynamics of complex metabolic processes (Minchin & Thorpe 2003; Hubeau & Steppe 2015).

Another medical imaging technique that could potentially be used to study CO<sub>2</sub> dynamically and at high spatial resolution (~ 1 mm) is <sup>13</sup>C-based magnetic resonance imaging (MRI). Carbon-13 is naturally occurring and not radioactive making it safer to use

with respect to  $^{13}\text{C}$ . Additionally,  $^{13}\text{C}$ -based magnetic resonance spectroscopy provides chemical information about the molecular arrangement of the  $^{13}\text{C}$ -atom. A different signal is obtained if a  $^{13}\text{C}$ -atom would be incorporated into e.g.  $\text{HCO}_3^-$ , fructose or glucose which would be a big advantage to study biological pathways. However, a standard MRI setting is rarely equipped with transmitting and receiving coils for detection of  $^{13}\text{C}$ . Additionally,  $^{13}\text{C}$ -atoms give a limited signal as their prevalence is only 1% of all naturally occurring carbon. Imaging carbon-13 by means of MRI is therefore only possible using hyperpolarized  $^{13}\text{C}$ . Through hyperpolarization, which is typically done at a very low temperature (2 K), the nuclear spin polarization of a material in a magnetic field is far beyond thermal equilibrium (Merritt *et al.* 2007; Kishimoto *et al.* 2019). However, once the polarized substance has left the polarizer, an irreversible decay of the polarization ensues. In the case of  $^{13}\text{C}$ -pyruvate the decay time is  $\sim 55$  sec as long as the substance is kept in a water solution (Golman *et al.* 2008). Consequently,  $^{13}\text{C}$ -based MRI was therefore not considered for studying dynamic carbon processes.

## 1.2 Basics of positron-based imaging

PET and positron autoradiography are both medical imaging techniques that measure the distribution and concentration of radiotracers in a non-invasive manner. Radiotracers are molecules that contain two moieties, or functional groups, an agent and a label. The agent is a molecule that has a high affinity for a specific target that needs to be imaged, while the label is a positron emitter (e.g.  $^{11}\text{C}$ ,  $^{18}\text{F}$ ,  $^{15}\text{O}$ ) in the case of positron-based imaging (Kiser *et al.* 2008; Saha 2016). The emitted positron  $\beta^+$  (antimatter of an electron) will react with an electron in its close environment and annihilate. The mass of both particles is hereby converted into energy manifesting as two gamma ( $\gamma$ ) photons, which are emitted in opposite directions ( $180^\circ$ ). Detection of these  $\gamma$ -photons within a ring of detectors forms the basis of PET imaging (Fig. 1.2) (Ametamey *et al.* 2008; Kim *et al.* 2013). Namely, when a pair of detectors each detect a  $\gamma$ -photon within a short time frame (e.g. 4 ns), it is assumed that annihilation took place along the line connecting both detectors, a process referred to as coincidence. Since millions of coincidences are detected during a PET scan, this information can be used to reconstruct a 3D image of the distribution of the radiotracer within the subject/object that is positioned inside the ring of detectors (i.e. the field of view or FOV). With regard to positron autoradiography, the object under study is exposed to a phosphoric plate which will be excited principally by positron radiation.

The resulting 2D image shows the integrated tracer activity detected during the exposure time in the tissue and has a spatial resolution that is about 20 times higher compared to PET ( $\sim 0.05$  vs. 1 mm).

A positron-emitting nucleus can be incorporated in naturally occurring molecules, such as  $\text{H}_2\text{O}$  or  $\text{CO}_2$  (Hubeau & Steppe 2015). In that respect, this thesis is focused around  $^{11}\text{C}$ -labelled  $\text{CO}_2$ . According to the tracer principle, labelled molecules are absorbed via normal metabolism and are distributed similarly throughout the study object as non-labelled molecules (Saha 2016). Moreover, radiotracers are administered in very small concentrations (nanomolar to picomolar range) in order not to alter or perturb the system (Turkheimer *et al.* 2014). Furthermore, positron-based imaging allows to study and even visualise processes *in vivo*, in real-time and with high spatial resolution, which is not possible by means of  $^{13}\text{C}$ - or  $^{14}\text{C}$ -based experiments, making them exquisite to study the dynamics of xylem-transported  $\text{CO}_2$ .

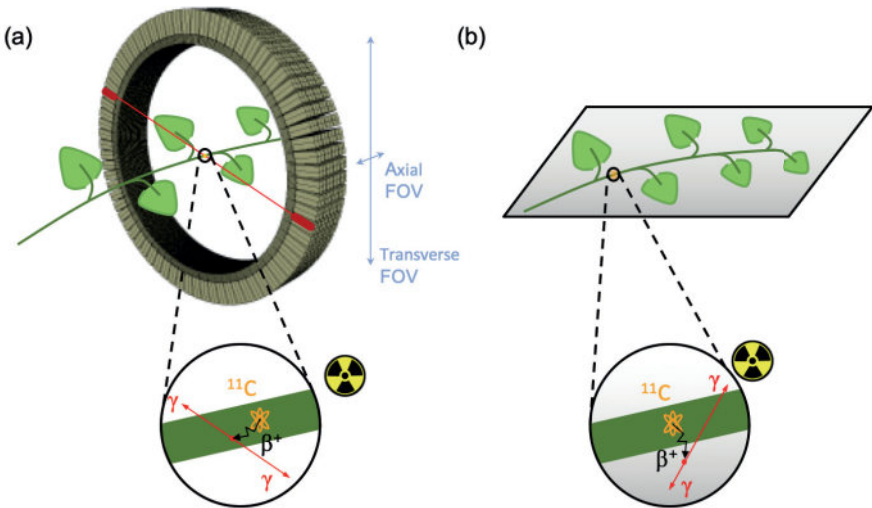


**Figure 1.2** (a) Schematic of a branch inside a PET detector ring. Positron decay of the (orange)  $^{11}\text{C}$ -nucleus in the branch is shown in the enlarged circle. The positron is travelling a certain distance (typically 1.1 mm in condensed matter- black arrow) known as the positron range to eventually collide with an electron and annihilate to produce two  $\gamma$ -photons (red arrows) travelling in opposite ( $180^\circ$ ) direction. Subsequently, these  $\gamma$ -photons can be detected by two different PET detectors (red ovals) in the detector ring. (b) Schematic of a branch exposed to a phosphoric autoradiographic plate that detects positrons.

### 1.3 Thesis outline

Since the first *in situ* measurements of internal CO<sub>2</sub> by McGuire & Teskey (2002), an increasing number of studies have been reporting on the significance of xylem-transported CO<sub>2</sub> in trees (e.g. McGuire & Teskey 2002, 2004; Aubrey & Teskey 2009; Maier *et al.* 2010; De Roo *et al.* 2019; Hubeau *et al.* 2019; Salomón *et al.* 2019). Therefore, investigation of internal CO<sub>2</sub> is of topical interest in plant sciences and we applied positron-based imaging to further push the boundaries on our understanding of its fate at high spatial and temporal scale.

Comparable to the breakthroughs induced by the clinical and pre-clinical application of positron-based imaging, we are convinced that these techniques have immense potential in the way that they could contribute extensively to plant science as well. However, only a limited number of research groups worldwide report plant studies using positron-based techniques as the complexity involved might form an obstacle for some research groups. Additionally, application of these techniques to study photosynthesis is challenging as it requires the use of radioactive <sup>11</sup>CO<sub>2</sub>. Under ambient pressure and temperature CO<sub>2</sub> is gaseous which imposes problems with regard to radiation safety. Hence special measures need to be taken regarding airtightness of the methodological set-up and introduction of the label to the plant tissue as to prevent radioactivity entering the atmosphere. Therefore, this PhD thesis will start by providing a broad outline on how to design and execute positron-based experiments on plant tissues in **Chapter 2**. Given its pivotal role in plants, the focus will be on tracing <sup>11</sup>CO<sub>2</sub> using PET. Hereby, the different steps toward quantitative imaging are considered as well as the related opportunities and challenges. Additionally, the use of positron autoradiography in plant science is hinted in this chapter.

To follow a thorough assessment of internal CO<sub>2</sub> reassimilation in stem tissues, subsequent chapters will focus on poplar species (i.e. *Populus × canadensis* Moench “Robusta” and *Populus tremula* L.). *P. × canadensis* is the ornamental hybrid between *P. deltoides* and *P. nigra* and has been planted in large numbers along river banks and urban areas in Europe, America and some parts of Asia (Hodoušek *et al.* 2017). *P. tremula* is a widespread Eurasian species, growing in temperate and boreal forests (Caudullo & de Rigo 2016). *Populus* species, commonly called aspen, are angiosperm and a member of the Salicaceae family. Furthermore, they are characterized by rapid growth and a naturally

high bark chlorophyll concentration (4.15 mg dm<sup>-2</sup> which is similar to that of the leaves; Kharouk *et al.* 1995), making *Populus* species well suited for the measurements performed in this PhD work. In the face of climate change, it is suggested that photosynthetic stems would be a major asset with respect to tree survival during long periods of drought (Cernusak & Marshall 2000; Vandegehuchte *et al.* 2015) which might increase the importance of *Populus* species.

The investigation of xylem-transported CO<sub>2</sub> was started by *in vivo* tracing of xylem-transported CO<sub>2</sub> in excised poplar leaves using <sup>11</sup>C in combination with PET and positron autoradiography and is described in **Chapter 3**. Therefore, a new method was developed to study plants in a half-open set-up supplying air to the leaves as to maintain regular photosynthesis while taking into account the hazards concerning radioactive <sup>11</sup>CO<sub>2</sub>. To show the applicability of both PET and autoradiography in visualising and quantifying CO<sub>2</sub> transport dynamics, the tracer was administered via the cut petiole and transport through the xylem was manipulated by excluding light or preventing transpiration.

As measurements in **Chapter 3** are based at leaf level, we aimed to get more insight into the photosynthetic properties of branch tissues. Consequently, **Chapter 4** describes visualisation of xylem-transported <sup>11</sup>CO<sub>2</sub> in 1-year-old poplar branches by means of positron autoradiography. The methods developed in **Chapter 3** are applied. Positron autoradiography is especially suitable for imaging thin branches because <sup>11</sup>C-positrons are detected with autoradiography, which travel an average distance of only ~ 1.1 mm in condensed matter upon annihilation (conversion to gamma rays). To allow mutual comparison of different autoradiographic experiments a normalization method was developed. Additionally, to date it has merely been assumed that retention/accumulation of xylem-transported CO<sub>2</sub> in woody tissues is related to assimilation by  $P_{wt}$  through exposure of photosynthetically active radiation (PAR) as described by experiments using <sup>13</sup>C- and <sup>14</sup>C-labelling in branches and leaves (e.g. Stringer & Kimmerer 1993; McGuire *et al.* 2009; Bloemen *et al.* 2015; Stutz *et al.* 2017; Stutz & Hanson 2019a, b) and CO<sub>2</sub> gas exchange measurements (e.g. Wittmann *et al.* 2001; Salomón *et al.* 2018; De Roo *et al.* 2019; Stutz & Hanson 2019a, b). Moreover, actual photosynthetic conversion of CO<sub>2</sub> into sugars was not tested for woody tissues in these studies. Therefore, <sup>13</sup>C-based measurements were performed and analysed using liquid chromatography–mass

spectrometry (LC-MS) to unambiguously attribute carbon tissue enrichment under light exposure to  $P_{wt}$ .

In **Chapter 5** the dynamics of xylem-transported  $\text{CO}_2$  are assessed through PET. By means of compartmental modelling, the dynamic data obtained from the PET images was used to retrieve the relative contribution of xylem-transported  $\text{CO}_2$  ( $\text{CO}_{2,X}$ ) to each of the carbon fluxes in woody species, i.e. radial efflux to the atmosphere  $E_A/\text{CO}_{2,X}$ , upward transport with the sap  $F_T/\text{CO}_{2,X}$  and assimilation  $A_X/\text{CO}_{2,X}$  and storage  $\Delta S/\text{CO}_{2,X}$ . The applied methodology in this chapter also allowed to retrieve a direct measure of the transport speed of internal  $\text{CO}_2$ . Both high spatial and temporal resolution of PET resulted in new observations regarding the fate of internal  $\text{CO}_2$  in 1-year-old branches of *P. tremula*.

From **Chapters 1-5**, new insights were acquired which enables us to discuss the applicability of both positron-based imaging methods PET and autoradiography to study xylem-transported  $\text{CO}_2$ . Hence, **Chapter 6** contains the main conclusions that may be inferred from the data presented in this PhD thesis, but also the main areas of uncertainty surrounding these conclusions. Additionally, it aims to identify potential areas of future research using positron-based imaging through identification of knowledge gaps and research opportunities. In this final chapter the following questions are dealt with:

- Can medical imaging techniques be used to study the dynamic fate of internal  $\text{CO}_2$ ?
- What is the relevance of xylem-transported  $\text{CO}_2$ ?
- Why should we expand positron-based imaging in plant studies?
- What are the challenges and future prospects for plant-PET?



# 2

## GUIDE TO PLANT-PET IMAGING USING $^{11}\text{CO}_2$



## **2.1 Introduction and overview**

Molecular imaging is a type of medical imaging that has the ability to trace or identify specific molecules within a specific anatomic location and can provide insight into metabolic pathways, tissue components, and tracing solute transport mechanisms (Wickline & Lanza 2002; James & Gambhir 2012). Today, molecular imaging is an established tool in both a clinical setting as well as in research facilities, where it is either used for diagnostic imaging and treatment, or for clinical research and drug development. Fuelled by the advances and developments of new radioactive labelled probes, functional imaging techniques such as positron emission tomography (PET) and single photon emission computed tomography (SPECT), in combination with computed tomography (CT) or magnetic resonance imaging (MRI) have become increasingly important (Levin 2005). Due to its high sensitivity and specificity for tumour detection, PET has become a standard and widely used medical imaging technique. Given the popularity of PET, both clinical and preclinical, its use has been extended to study plants (Minchin & Thorpe 2003; Jahnke *et al.* 2009; Hubeau & Steppe 2015; Karve *et al.* 2015). However, only a limited number of research groups worldwide report PET-based studies, while we believe that this technique has much more potential and could contribute extensively to plant science. The limited application of PET may be related to the complexity of putting together methodological developments from multiple disciplines, such as radio-pharmacology, physics, mathematics and engineering, which may form an obstacle for some research groups. By means of this manuscript, we want to encourage researchers to study plants using PET. The main goal is to provide a clear description on how to design and execute PET scans, process the resulting data and fully explore its potential by quantification via compartmental modelling. The different steps that need to be taken will be discussed as well as the related challenges. Hereby, the main focus will be, although not limited to, on tracing  $^{14}\text{C}$  given its key role in plants.

## **2.2 Experimental design of plant-PET studies**

### **2.2.1 Communication and planning**

The objective of PET imaging is to acquire (quantitative) images of the distribution of a certain radiotracer in the object under study. To obtain these images a multidisciplinary

trajectory is followed within a PET centre (Fig. 2.1). It starts with the production of the positron emitting isotope in a cyclotron. Subsequently, this isotope is linked to the desired molecule by radiopharmacists to obtain the required radiotracer, which is then transported to the PET scanner. Due to the short half-life of PET isotopes (see Table 2.1), the PET scanner and cyclotron units are generally in close proximity. The PET system is typically operated by a high-level technician or researcher, while a medical physicist keeps track of the quality assurance of the PET system. Once the acquired PET data are reconstructed into 3D images, image analysis and quantification can take place.

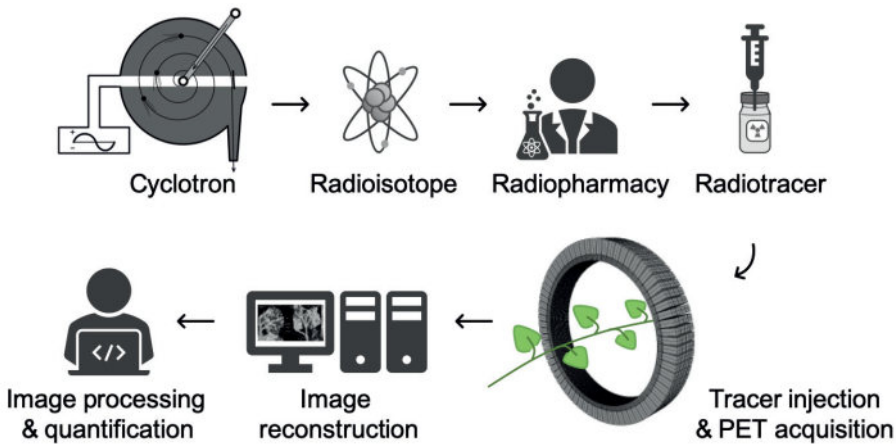


**Figure 2.1** Schematic showing the multidisciplinary nature of PET imaging.

PET centres are growing in large numbers worldwide and can be found in academic institutes as well as in smaller and larger hospitals. Smaller hospitals usually do not have a cyclotron, generally have a single PET scanner (typically combined with CT) and purchase their PET radiopharmaceuticals from commercial vendors that have a cyclotron facility (which is only possible for longer-lived radioisotopes, e.g.  $^{18}\text{F}$ ). Larger hospitals and academic institutes have PET centres that can accommodate one or more cyclotrons, a radiochemistry laboratory and often several (multimodal) PET scanners, including laboratory animal (e.g. Alexoff *et al.* 2011; Hubeau *et al.* 2019b), clinical (e.g. Garbout *et al.* 2012; Karve *et al.* 2015) or self-designed imaging systems (e.g. Uchida *et al.* 2004; Jahnke *et al.* 2009; Weisenberger *et al.* 2012). In these larger centres the integral multidisciplinary workflow can be followed. Because of the strict regulations regarding radiation exposure, PET centres are heavily shielded to minimise radiation exposure to

workers (Saha 2016). This usually implies that the rooms do not have windows and thus have a limited availability of sunlight. By consequence, it is advised to provide (timed) lighting to maintain regular plant functioning when performing plant-PET imaging. Additionally, due to the seasonal dependence of plant material, it is advised to plan experiments well in advance (~ two months, although depending on the number of scans) as these medical imaging devices are generally well occupied.

**Table 2.1** Production and application of positron emitting tracers used in plant science. The mean positron range is the distance connecting the place of decay and the place of annihilation with a straight line.

Radio-nuclide	Target material	Nuclear reaction	Potential tracers for plant experiment	Half-life (min)	Mean positron range (mm)
$^{11}\text{C}$	$\text{N}_2 + 5\% \text{H}_2$ $\text{N}_2 + 0.1\% \text{O}_2$	$^{14}\text{N}(\text{p},\alpha)^{11}\text{C}$	$^{11}\text{CO}_2$ , $^{11}\text{C}$ -methyl jasmonate	20.36	1.1
$^{18}\text{F}$	$\text{H}_2^{18}\text{O}$	$^{16}\text{O}(\text{p},\text{n})^{18}\text{F}$	$^{18}\text{F}$ -fluoro-deoxy-glucose ( $^{18}\text{F}$ FDG) $^{18}\text{F}$ Fluorine (aq)	109.74	0.6
$^{13}\text{N}$	$\text{H}_2^{16}\text{O}$	$^{16}\text{O}(\text{p},\alpha)^{13}\text{N}$	$^{13}\text{NO}_3^-$	9.96	1.5
$^{15}\text{O}$	$\text{N}_2$	$^{14}\text{N}(\text{d},\text{n})^{15}\text{O}$	$\text{H}_2^{15}\text{O}$	2.03	2.5

### 2.2.2 Production and formulation of radiotracers

Whereas nowadays radioactive tracers are inherently linked to clinical practice, their first application to study biological processes made use of plants and was described by de Hevesy (1923). He played a key role in the development of radiotracers, which has indirectly led to the development of nuclear medicine and PET imaging. As indicated earlier, the production of radiotracers for PET imaging starts with a cyclotron, where a charged particle (usually a hydrogen ion, e.g.  $\text{H}^+$ ) is accelerated to a high velocity to bombard a target molecule, eventually creating an unstable nucleus that decays by positron emission. Depending on the target molecule a different radionuclide can be produced (Table 2.1). The most widely used positron-emitting nuclide in plant science is carbon-11 ( $^{11}\text{C}$ ), which is usually administered as gaseous  $^{11}\text{CO}_2$  to study long-distance transport of photosynthates (Minchin & Thorpe 2003; Karve *et al.* 2015; Hubeau *et al.* 2018) or can also be administered in an aqueous solution to study xylem-transported  $\text{CO}_2$

(Bloemen *et al.* 2015; Mincke *et al.* 2018; Hubeau *et al.* 2019b).  $^{11}\text{CO}_2$  is generally produced in two different ways depending on the target material, i.e.  $\text{N}_2/\text{O}_2$  (Karve *et al.* 2015) or  $\text{N}_2/\text{H}_2$  (Hubeau *et al.* 2018). In the former case, the nuclear reaction results immediately in the formation of  $^{11}\text{CO}_2$ , however, with the undesired by-product  $^{11}\text{CO}$  (Saha 2016). Application of  $\text{N}_2/\text{H}_2$  results in the formation of  $^{11}\text{CH}_4$  which subsequently needs to be oxidised via cobalt oxide column to yield  $^{11}\text{CO}_2$  as described by Landais & Finn (1989). This last step involves heating to 500 °C, requiring the use of a tube furnace that might not be a part of the standard equipment in a cyclotron unit.

Depending on the research objective of the experiment,  $^{11}\text{CO}_2$  can be trapped in a NaOH solution to be applied as a gas (e.g. Hubeau *et al.* 2018), or bubbled through a slightly acidic buffer (e.g. Tris, phosphate or citric acid) to obtain an aqueous solution (e.g. Mincke *et al.* 2018). In the former case, the dissolved  $^{11}\text{CO}_2$  can be released from the NaOH solution as a gas, by injection into an excess acidic solution (e.g.  $\text{H}_2\text{SO}_4$ ), which can subsequently be directed towards the plant tissue. With regard to the formulation of a radioactively-enriched buffered solution that has to be exposed to the xylem (regardless the radioisotope), the buffer's pH is allowed to deviate slightly from the pH of xylem sap of the species under study. Specifically, once the tracer is taken up equilibrium reactions will occur, creating the right pH inside the tissue (Butler 1991). Hence, the pH of an  $^{11}\text{CO}_2$ -enriched aqueous solution can be slightly more acidic than the xylem sap to favour the  $^{11}\text{C}$ -label being dissolved as  $\text{CO}_2$  (aq.) over bicarbonate.

The use of  $^{11}\text{C}$  is not limited to  $\text{CO}_2$  as it can also be built into other traces like methyl jasmonate, auxin or salicylic acid (Thorpe *et al.* 2007; Agtuca *et al.* 2014). Other positron-emitting isotopes applied in plant studies are fluorine-18 ( $^{18}\text{F}$ ), nitrogen-13 ( $^{13}\text{N}$ ) and oxygen-15 ( $^{15}\text{O}$ ), which can be incorporated into biologically active molecules like  $^{18}\text{F}$ -fluoro-deoxy-glucose ( $^{18}\text{FDG}$ ),  $^{13}\text{NO}_3^-$  and  $\text{H}_2^{15}\text{O}$ , respectively. Therefore, the use of these radiolabelled molecules include, but is not limited to, investigating sugar transport (e.g. Fatangare & Svatoš 2016), nitrogen distribution (e.g. Siddiqi *et al.* 1989; Liang *et al.* 2011) and water transport (e.g. Mori *et al.* 2000; Kiyomiya *et al.* 2001), respectively. Application of  $^{18}\text{F}$  is also described as a proxy for tracing water transport (e.g. Ishioka *et al.* 1999).

The above-mentioned radiotracers are only a few examples of molecules, together with their involved pathways, that can be studied in plants using PET imaging. By making use of organic (radio)chemistry, radionuclides can be incorporated in many other

dedicated molecules. However, due to the short half-life, the isotope needs to be labelled to the required molecule by a radiopharmacist in a short time frame (Fig. 2.1). After the labelling, the radiotracer is ready to be exposed to the plant material and can be scanned.

### 2.2.3 Working safely with gaseous radioactivity

Since  $^{11}\text{CO}_2$  is a gas under standard temperature and pressure, extra attention should be paid to the experimental set-up to reduce the risk of radioactive gas being released into the atmosphere. Concerning the set-up, airtightness must be achieved and maintained throughout the entire experiment. However, this is challenging since plants require continuous supply of  $\text{CO}_2$  to maintain photosynthesis. Therefore, most systems enclose the plant, or part of it, in a labelling chamber that is connected to a gas circulation system (e.g. Kawachi *et al.* 2011; Dirks *et al.* 2012; Agtuca *et al.* 2014; Hubeau *et al.* 2018). A straightforward method to detect leaks in the labelling chamber is to measure the in- and outflowing air using flow meters (Hubeau *et al.* 2018). However, the main challenge remains to enclose the plant tissue in an airtight way. When studying or labelling a photosynthesising organ, the labelling chamber usually has to be made out of translucent material (e.g. plexiglass or see-through plastic) to allow illumination of the plant material with photosynthetically active radiation (PAR). Airtight constructions enclosing an entire plant can easily be made of plexiglass (e.g. Karve *et al.* 2015), whereas enclosing a part of a plant (e.g. leaf or branch) can be done using both plexiglass (e.g. Kawachi *et al.* 2011) or plastic bags (e.g. Hubeau *et al.* 2018). When enclosing only a part of the plant, damaging the tissue should be avoided to not disturb plant functioning. An elegant way is to envelop the plant tissue with a small cylindrical piece of flexible rubber which is lubricated with vacuum grease on the inside (Fig. 2.2a,b). The labelling chamber can then be closed by using small straps for a bag (Fig. 2.2a) over this piece of rubber without pinching off the phloem and xylem tissue to maintain regular sugar and water transport, respectively. Alternatively, malleable polysiloxan material like Terostat-IX (Henkel AG & Company, KGaA, Düsseldorf, Germany – Fig. 2.2c) can be used to enclose the plant tissue while separating two compartments from each other (e.g. labelling from monitored compartment). A drawback of using small labelling chambers is the difficulty to control their microclimate, especially relative humidity tends to be higher at lower air flows (i.e. lower air renewal rate) due to transpiration of the plant tissue. To avoid  $^{11}\text{CO}_2$  that is not

taken up by the plant to enter the atmosphere, the outflowing air system can be connected to a CO<sub>2</sub> scrubbing column, containing soda lime pellets (Hubeau *et al.* 2018).

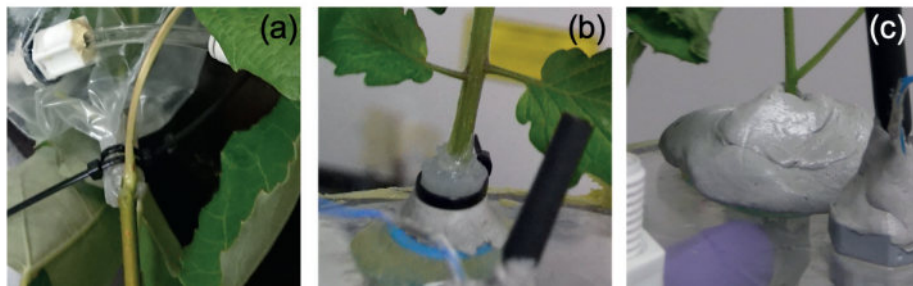


**Figure 2.2** Methods of enclosing a branch part in (a) a bag or (b,c) a plexiglass chamber while hermetically sealing the branch part that will be labelled from (a) the atmosphere and/or (b,c) other parts of the plant without damaging the plant tissue. One method to do this is enveloping the branch by a small cylindrical flexible piece of rubber, which is lubricated with vacuum grease on the inside (a,b). To (a) close the plastic branch bag or (b) to fix the plant position in a plexiglass chamber straps can then be tightened upon the rubber without damaging the plant tissue. Alternatively, (c) plant tissues can be fixed within a plexiglass chamber while separating two compartments using malleable polysiloxan material.

With regard to radiation safety on the experimental site it is advised, if not obligated, to make a standard operating procedure (SOP) to indicate and assess risks of executing <sup>11</sup>CO<sub>2</sub> experiments. Furthermore, exposure to radiation can be minimised according to the triad of “Time-Distance-Shielding” (Lakhwani *et al.* 2019). Each factor has a different impact on the absorbed dose. Time is related to the exposure opportunities to a source of radioactive radiation as well as the time of exposure, and it is obvious that these should be reduced. Additionally, radiation exposure is inversely proportional to the square of the distance from the source. This means that doubling the distance reduces the exposure to one quarter. The International Commission for Radiation protection (ICRP) recommended a distance of at least 2 m from the source of radiation, which may be considered safe. Furthermore, the use of shielding is most effective to reduce radiation exposure. Appropriate stopping material for  $\gamma$ -photons are lead or concrete and allow reduction of exposure that is exponential to the thickness of the material (Table 2.2) (Turkheimer *et al.* 2014). However, note that  $\gamma$ -photons are far more energetic than X-rays (Fig. 2.3) so traditional protective clothing, such as lead aprons, lead goggles or lead gloves are far less



effective if not useless in a PET environment. Information about radioactivity and the standard international unit to measure radioactivity is summarised in Text box 2.1.

**Table 2.2** The thickness of an absorbing material required to reduce the intensity or exposure of a radiation beam (in this case 1 MeV  $\gamma$ -rays) to one-half of the initial value when placed in the path of the beam.

Material	Half-value layer [cm]
Wood	29
Packed soil	9.1
Concrete	6.1
Lead	0.8

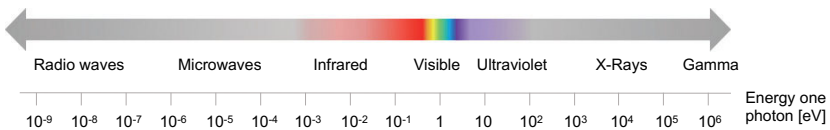


**Figure 2.3** Electromagnetic spectrum ranging from radio waves to gamma ( $\gamma$ ) rays with their corresponding energy level in electron volt. In PET imaging high energetic  $\gamma$ -photons (511 keV) are detected.

### Text box 2.1 Measuring radioactivity

Radioactive decay of a PET isotope occurs by the emission of a positron from a nucleus. The amount of radioactivity of a radiotracer is measured by the number of nuclei that decay per unit time. The standard international unit of radioactivity is Becquerel (Bq). One Bq corresponds with one disintegration per second. Curie (Ci) is the original unit of radioactivity and corresponds with the amount of radiation that is produced by one gram of radium ( $^{226}\text{Ra}$ ). This is an enormous unit as it equals 37 GBq compared to the clinical used activities for PET imaging, which is in the range of 37 – 740 MBq (1-20 mCi). In clinical practice, it is of interest to quantify the radiation energy absorbed by biological tissues, i.e. ‘absorbed dose’. Eventually, to evaluate the harmful effect of a radiation dose to an organism the ‘effective dose’ can be calculated. Therefore, the

absorbed dose is corrected for the radiation type ( $\alpha$ ,  $\beta$  or  $\gamma$  radiation) and the radiosensitivity of the organ receiving the radiation (Turkheimer *et al.* 2014; Lakhwani *et al.* 2019). For PET-imaging, annihilation of a positron and an electron generates two  $\gamma$ -photons, each having an energy of 511 keV. This energy is higher than the energy of X-rays (Fig. 2.3) that are produced in computed tomography (CT) to create anatomical images or 'slices' of specific areas of the body. However, in general, we can state that the dose absorbed during a PET or CT is approximately the same. A CT uses X-ray photons with less energy, but many photons are required to obtain a good CT scan. While for a PET scan, a small amount of radioactivity is administered to a patient, so that a smaller number of  $\gamma$ -photons are involved, but each photon has more energy. Both absorbed and effective dose are not common in plant sciences.

#### 2.2.4 PET data acquisition

As mentioned above, PET is based on the detection of two photons (511 keV each) that originate from  $\beta^+$  emitting radiotracers (e.g.,  $^{11}\text{CO}_2$ ). The two photons are detected electronically within a short time window (e.g., 4 ns), i.e. coincidence events, using a ring of detectors. When two photons are detected by two different detectors from the detector ring, it is assumed that the annihilation occurred along the straight line connecting the centers of both detectors, called the line of response (LOR). During a PET-scan millions of LORs are detected that are used to reconstruct a 3D image of the *in vivo* distribution of a radiotracer. Despite this simple concept, different factors can degrade the image obtained by a PET scanner due to physics or system performance. These effects include photon acolinearity, attenuation of photons by tissue, scatter coincidence and random coincidence (Saha 2016). However, the most challenging image degrading factor with regard to imaging plants is related to the positron range. This is the distance that the positron travels through the object to lose enough kinetic energy before annihilation takes place (black zigzag pattern in Fig. 1.2). The mean distance between decaying nucleus and the site of annihilation for common types of radionuclides used in plant science is generally larger than 1 mm (Table 2.1 – Jodal *et al.* 2012), which poses challenges upon imaging leaves whose thickness is in the range of tens of  $\mu\text{m}$  for mesophyll and hundreds of  $\mu\text{m}$  up to some mm for veins (Witkowski & Lamont 1991). Particularly, leaves of most plants are so thin that a large fraction of positrons emitted from PET isotopes escape the

tissue before annihilation. Alexoff *et al.* (2011) found that the fractions of positrons that escaped the leaf parenchyma of tobacco plants (200 – 250  $\mu\text{m}$ ) were  $64 \pm 4\%$ ,  $59 \pm 1\%$  and  $67 \pm 2\%$  for  $^{11}\text{C}$ ,  $^{18}\text{F}$  and  $^{13}\text{N}$ , respectively. Because the probability of annihilation increases with thickness, escape fractions were lower in thicker leaf areas like the midrib (1 – 2 mm) (Alexoff *et al.* 2011). When studying single leaves, an approach to increase the detection of positrons actually emitted inside the plant material but escaped from it before annihilating includes the use of thin plexiglass plates that can be positioned parallel with the leaf blade, while ensuring not to limit air contact with the leaf (Alexoff *et al.* 2011; Hubeau *et al.* 2019b). The escaped positrons are likely to annihilate on the plexiglass plates which will show up on the PET image and can as such be taken into account. When comparing tissues with variable size, the percentage of positron annihilation along a given tissue thickness (assumed water) can empirically be estimated as described by Jødal *et al.* (2012). This can subsequently be used to correct annihilation in the tissue during post-processing of the images. Being aware of these limitations the PET experiment can be executed.

Another possible advantage of PET is the complementarity with positron autoradiography, as demonstrated by Hubeau *et al.* (2019b). After the PET experiment the plant tissue is hereby exposed to an imaging phosphor plate for typically 10-15 min, depending on the remaining radioactivity in the plant tissue. The resulting 2D image gives a high-resolution snapshot in time showing the integrated tracer activity detected during the exposure time in the plant tissue. Positron autoradiography has a much higher spatial resolution ( $\sim 24 \text{ pixels mm}^{-1}$ ) compared to PET ( $\sim 0.3 - 1 \text{ pixel mm}^{-1}$  for PET) (Fig. 2.4).

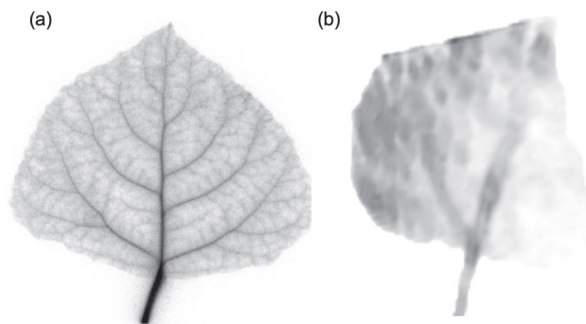


**Figure 2.4** Example of (a) an autoradiographic image and (b) a PET image of a leaf of *Populus tremula* L.. In the PET image (b) the secondary veins are barely visible whereas the autoradiogram clearly depicts them as well as the tertiary veins.

Positron autoradiography has however rarely been applied in plant science which might be linked to its limited availability. Nonetheless, due to its superior resolution it has been used as a proof of principle to acquire detailed tracer distribution of xylem-transported CO<sub>2</sub> in leaves in addition to <sup>13</sup>C tissue enrichment analysis with elemental analysis coupled to isotope ratio mass spectrometry (Bloemen *et al.* 2015). A dissolved <sup>11</sup>CO<sub>2</sub> or <sup>13</sup>CO<sub>2</sub> label was hereby provided to detached leaves. Whereas the spatial resolution of <sup>13</sup>C-based analysis was constrained to the leaf tissue component level, positron autoradiography showed a more detailed spatial distribution within a single tissue, in particular in secondary veins. Additionally, this techniques has been successfully applied to characterise phloem loading strategies (passive or active) in contrasting plant species (i.e. temperate and tropical tree species and herbaceous crops) when allowing them to assimilate gaseous <sup>11</sup>CO<sub>2</sub> (Hubeau *et al.* 2019a). Aside from the above-mentioned studies where radiography was used directly to image the experimental tissues, also indirect useage is described. Moreover, it has been used in a creative way to assess carbon partitioning to the major non-sturctural carbohydrates (i.e. fructose, glucose, sucrose and starch) in leaves of several species (i.e. maize, tabocco, sorghum and Arabidopsis) (Babst *et al.* 2013). Hereby leaves were labelled using gaseous <sup>11</sup>CO<sub>2</sub> of which tissue extracts were analysed by high-performance thin-layer chromatography (HPTLC) to separate the soluble sugars. The TLC plates were subsequently exposed to an autoradiographic plate to determine the metabolic partitioning of assimilated <sup>11</sup>C to soluble sugars. In all of these studies positron autoradiography allowed studying rapid metabolic responses of plant tissues that occur on a time scale of minutes.

### 2.2.5 Image reconstruction

During a PET scan every recorded LOR in the field of view (FOV) is stored (Saha 2016). An image cannot be directly obtained, because it is not possible to determine exactly where the annihilation took place along the LOR. Therefore, an additional reconstruction step is needed. In nuclear medicine, iterative reconstruction algorithms are used for this purpose (Vandenberghe *et al.* 2016). The most frequently used iterative reconstruction method for PET is Maximum Likelihood Expectation Maximisation (MLEM). In this algorithm the solution (actual image) is found by taking into account the stochastic character of radioactivity (Shepp & Vardi 1982). Note that several variations of the MLEM algorithm exist, including Ordered Subset Expectation Maximisation (OSEM - Boellaard *et*

*al.* 2001) and the row-action maximum-likelihood algorithm (RAMLA - Browne & De Pierru 1996). A 2D- and 3D-variant exist of the MLEM method which both result in a 3D image but differ in the way the data from detector rings are used for reconstruction. In 2D-MLEM reconstruction coincidences are counted only within a few consecutive rings of detectors (e.g. two or three rings). Moreover, coincidences within each small group of detector rings results in a transverse slice of the final image, which allows to obtain quantifiable images (in Bq/ml). The 3D-version allows coincidence counts between any of the detector rings, resulting in an image with a higher resolution compared to the 2D-MLEM. Because of the positron range, resolution of the 2D-reconstructed images of plant leaves or branches is often limited making it appropriate to use 3D-MLEM reconstruction.

Decay correction for the applied radioisotope is generally executed during image reconstruction. However, several other factors affect the acquired PET data, which include photon attenuation, scattered coincidences, random coincidences and require image corrections. The extent of these data corrections is dependent on the size, shape and composition of the object being imaged and can be estimated by making use of a phantom (i.e. a volume of material artificially made, resembling the size/dimensions of the plant tissue under study, to simulate its properties when exposed to radiation). Karve *et al.* (2015) described the impact of these effects using a phantom when imaging sorghum and found that scatter correction had little effect (< 1%) on the stem and shoot, while attenuation of the  $\gamma$ -photons (due to energy loss to the irradiated tissue) led to an error of 30% in the stem and 55% in the root. It is thus especially important to investigate the impact of these effects when comparing plant tissues of different sizes as well as larger tissues (e.g. stems) given the half-value layer of 29 cm for wood (Table 2.2).

By correcting for image degrading effects, such as photon attenuation, scatter and random coincidences, quantitative images can be obtained where each voxel is expressed in Bq/ml. However, if the specific activity, i.e. the activity per quantity of the radionuclide, is known for the applied radiotracer inside the phantom, then image analysis software enables quantitative analysis (e.g.  $\text{g mL}^{-1}$ ) as the specific concentration of radiotracer inside the tissue can be deduced from it.

Image reconstruction is demanding in terms of computational power and time, especially when the stored LORs have to be reconstructed into different time frames to monitor a dynamic process, which is called dynamic or 4D PET. In dynamic PET, it is also

advised to reconstruct a static image that is the mean/sum of the all the individual time frames. This static 3D image has a higher signal to noise ratio (SNR) than the individual time frames (Turkheimer *et al.* 2014) and it is particularly useful for visual assessment of the entire dynamic process in one 3D image. This is demonstrated in Fig. 2.5, where the static image is shown in the upper left corner along with some dynamic time frames of 20 min. To this end, a *Populus tremula* L. branch was exposed to gaseous  $^{11}\text{C}\text{O}_2$ . The static image shows  $^{11}\text{C}$ -tracer accumulation in the complete branch segment inside the FOV in contrast to the dynamic images, where only part of the branch segment is visible due to dynamic nature of the process. Aside from the higher SNR, the reconstruction time of such a static image is also much shorter than the dynamic reconstruction time (min vs. h).

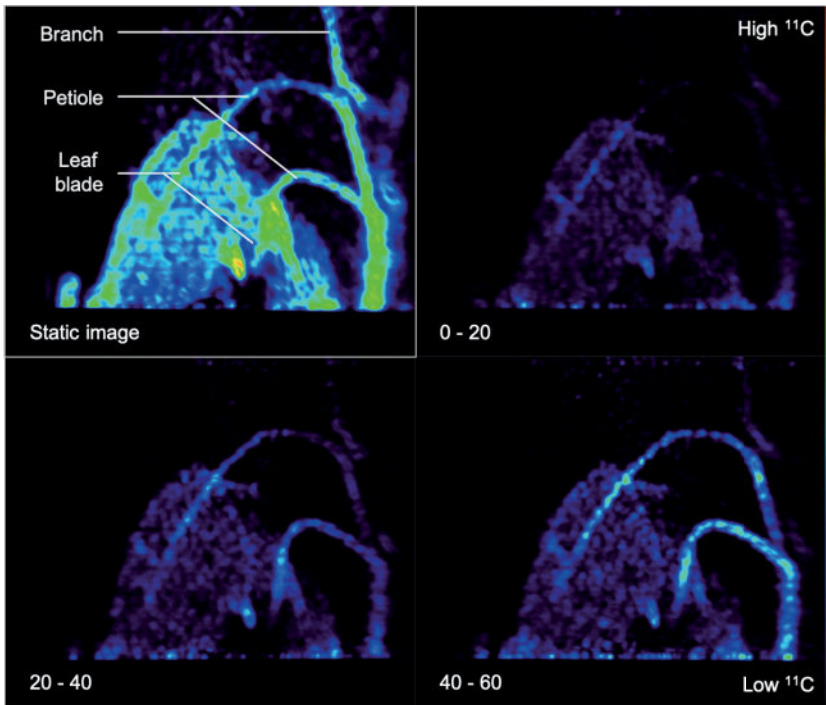


**Figure 2.5** Example of a static (upper left rectangle) and three dynamic PET images (showing timestamp in minutes in the lower left corner) of a *Populus tremula* branch that was exposed to gaseous  $^{11}\text{C}\text{O}_2$  during a 60 minutes PET acquisitions. The static PET image (i.e. sum of dynamic images) has a better SNR and can be used for image analysis, i.e. drawing ROIs. These ROIs can then be copied on the dynamic PET images to obtain tracer concentrations per ROI over time, i.e. TTCs. Note that transport of the label via the petioles to the branch is visualised by dynamic PET images.

## 2.2.6 Image processing and quantification

After image reconstruction, while applying the necessary corrections (if needed), 3D or 4D images are obtained, which can be analysed using image analysis software. Commonly used software includes OsiriX (Rosset *et al.* 2004 – commercial), Horos (<https://horosproject.org>, GNU Lesser General Public License, Version 3.0 (LGPL 3.0) – open-source) and AMIDE (Loening & Gambhir 2003 – open-source). These software packages allow to reduce noise by smoothing or blurring the images, which can be executed on both static and dynamic reconstructed images. A common approach is the application of a gaussian filter, whereby a gaussian curve is applied to calculate the intensity of each voxel by using a fixed number of voxels around it. However, reducing noise will also result in poorer spatial resolution. Finding the ideal trade-off between noise and spatial resolution is usually performed on the static image when a dynamic process needs to be quantified. Subsequently, this static 3D image can be used to draw regions of interest (ROIs) onto the plant tissue of interest (Fig. 2.6a). In Fig. 2.6a, xylem-transported  $^{14}\text{C}$  in a branch segment of *P. tremula* is imaged. When the plant tissue is visualised and the ROIs are drawn, these ROIs can be copied the dynamically reconstructed PET data (e.g. series of PET images per 5 or 10 minutes of the acquisition time) to obtain a number of time-tracer curves (TTCs – one for each ROI) which can be used for further quantification. An example of measured TTCs (circles) for four consecutive ROIs (Fig. 2.6a) is shown in Fig. 2.6b.

TTCs can then be used to retrieve physiological properties of the plant like phloem transport speed (based on the time of first tracer arrival, e.g. Karve *et al.* (2015)), uptake and distribution of plant nutrients like  $\text{NO}_3$  (e.g. Kawachi *et al.* 2008; Liang *et al.* 2011),  $\text{NH}_4$  (e.g. Kiyomiya *et al.* 2001b) or Fe (e.g. Tsukamoto *et al.* 2009), photoassimilate translocation to storage organs (e.g. Kikuchi *et al.* 2008; Hidaka *et al.* 2019), xylem-transported  $\text{CO}_2$  (Hubeau *et al.* 2019b), as well as changes in whole-plant carbon allocation (e.g. Karve *et al.* 2015).

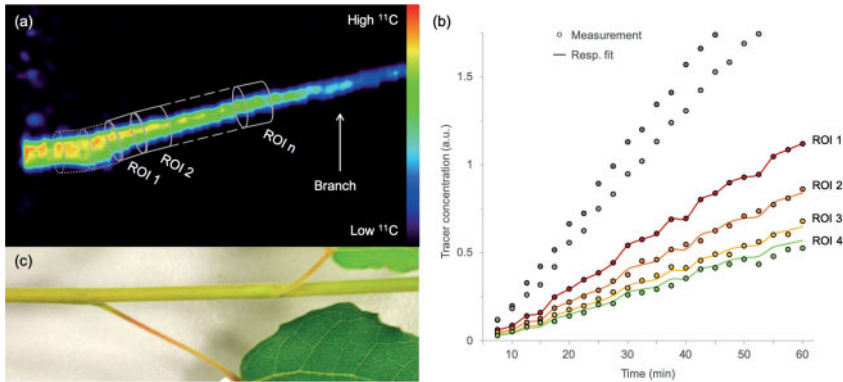


**Figure 2.6** Example of (a) a static volume rendered PET image showing xylem-transported  $^{11}\text{C}$  in a branch of *Populus tremula*. By extracting the tracer concentrations within e.g. four consecutive ROIs of the corresponding dynamic PET images (b) TTCs are obtained (circles). Time is expressed in minutes after pulse-labelling aqueous  $^{11}\text{C}$  to the cut end of the branch. By means of mathematical frameworks a model, representing the molecular system under study, can be fitted (continuous lines) to the measured TTCs. Identification of the corresponding (c) plant part inside the FOV is critical to achieve good ROI drawing practices. Moreover, without (c) it would be straightforward to draw ROI 1 on the branch segment having the highest tracer concentration (dotted ROIs in (a)). However, a petiole originates on the branch segment enclosed in these ROIs, which cannot be resolved from the branch itself due to the limited spatial resolution of the PET system. Corresponding TTCs (grey measurements in (b)) show an incorrect higher signal because the  $^{11}\text{C}$ -tracer within the branch and petiole is added in these ROIs. Note that PET image (a) shows the side view whereas the branch (c) is shown from above.

Additionally, dynamic PET measurements can be used as input for mathematical frameworks to retrieve physiological plant parameters that are difficult to measure with other techniques. This can be achieved by means of an input-output framework, as developed by Minchin and co-workers (Minchin & Thorpe 2003; Minchin 2007, 2012; Kiser *et al.* 2008), or by mechanistic compartmental modelling (Bühler *et al.* 2011a, 2014, 2018; Hubeau *et al.* 2018). An input-output-model is a type of black box model, based on empirical equations which do not describe the underlying mechanisms. As a consequence, these models are not valid out of the range of observations as they are based on historical data so that predictions about future scenarios involving structural changes are not valid. Compartmental models, on the other hand, are a type of mechanistic models since the system under study is described by the underlying mathematical equations. Therefore, compartmental models have an advantage over input-output models because they restrict



model outcomes with physical boundaries, allowing to restrict the involved model parameters/characteristics to realistic ranges (Bühler *et al.* 2011a; Hubeau & Steppe 2015). Therefore, compartmental models are of high interest to study long-distance transport in plants for the investigation of functional traits, especially under diverse environmental conditions (Jahnke *et al.* 2009). This boils down to translating the tracer dynamics (i.e. TTCs) by a model that represents the system under study. The model is composed of mass balances (i.e. differential equations) defined by tracer concentrations and kinetic rate constants to describe the exchange between compartments. This method has usually been implemented with the assumption that the system under study does not change during the experiment (Minchin & Thorpe 2003). An example of fitted tracer profiles to measured TTCs is shown in Fig. 2.6b as continuous lines. The goal of fitting a model to dynamic tracer data (i.e. model calibration) is to derive specific parameters that have a physiological meaning, which are difficult to obtain by direct measurement. Specifically, due to the limited spatial resolution of PET ( $\sim 1 - 3$  mm), physiological processes in several tissues are integrated into the measured TTCs. Compartmental modelling has been applied in  $^{14}\text{C}$ -based plant studies, mainly to investigate phloem characteristics (Fares *et al.* 1988; Bühler *et al.* 2011b, 2014; Hubeau *et al.* 2018). Specifically, mechanical agitation of cotton seedling's leaves was found to reduce carbon export rate by 33% (Fares *et al.* 1988). In the same study carbon storage and export rates of  $\text{C}_4$  bunch grasses (i.e. pangola grass, little bluestem and brownseed paspalum) were higher in the afternoon than in the morning inspite of a decreased photosynthetic activity. Bühler *et al.* (2011b, 2014) developed a mechanistic compartmental tracer transport model, to allow a quantitative data analysis and comparison of PET experiments. This model simplifies the complexity of axial transport and lateral exchanges in the transport pathways of plants (e.g. the phloem) by simulating transport and reversible exchange within  $n$  compartments. The model was adapted Hubeau *et al.* (2018) to investigate the vulnerability of phloem speed to drought under climatic change. It was found that well-watered trees grown under elevated  $\text{CO}_2$  concentrations ( $T_E$ ) had higher phloem speed than trees grown under ambient  $\text{CO}_2$  levels ( $T_A$ ). However, for the same level of drought the phloem speed of  $T_E$  trees strongly reduced by 81%, whereas phloem speed reduced by 61% in  $T_A$  trees. The main advantage offered by PET in these studies is related to its *in vivo* nature. Moreover, individual plants could be scanned multiple times making it easier to detect (sometimes even subtle) differences in the resulting model parameter values as

a result of external experimental conditions, e.g. drought (Hubeau *et al.* 2018) or recovery from mechanical agitation (Fares *et al.* 1988). Software packages that allow implementation of plant models include MATLAB (MathWorks, Inc, Natick, MA, USA - commercial) and the plant modelling software PhytoSim (Phyto-IT, Gent, Belgium - commercial).

It is clear that good and reliable ROI data is a prerequisite when fitting TTC data to a model. Therefore, it is of great importance to know which part of the plant is being imaged inside the FOV. PET imaging systems that are combined with a CT or MRI module facilitate this process because anatomical images can be obtained aside from the functional PET data. The importance of good ROI-drawing practices is exemplified in Fig. 2.6c which shows the branch segment that was imaged in Fig. 2.6a. It seemed obvious to start drawing ROIs from the point where the highest activity was measured (dotted ROIs). However, in these ROIs a petiole originates from the branch and due to the limited spatial resolution of the PET system ( $\sim 1 - 3$  mm), the tracer uptake inside the petiole and branch could not be resolved, resulting in TTCs with a higher tracer uptake for these ROIs (grey circles in Fig. 2.6b). This would inevitably prompt incorrect parameter values upon model calibration. Therefore, it is advisable to select a branch segment without ramifications for ROI analysis.

### 2.3 Conclusion

PET imaging is one of the key diagnostic tools used clinically to follow-up and treat diseases by making use of positron-emitting radioisotopes. The *in vivo* nature of this technique in combination with the ability to monitor dynamic processes has led to its application in plant science. Specifically, this imaging technique has already successfully shown its applicability to investigate the dynamic transport of nutrients, phytohormones as well as photoassimilates. However, in contrast to the numerous studies using laboratory animals and humans, the number of studies on plants is still limited. Therefore, the aim of this manuscript is to provide general insights on the opportunities of PET imaging as a tool for plant experiments and to guide the reader to start PET experiments on plants. To fully grasp PET imaging along with its potential and limitations, it is advised to have a profound read on the principles of PET or to follow a course on PET or biomedical imaging in general. Besides explaining the basics of PET imaging, this guide

starts from planning the experiment, elucidates the different steps to execute plant-PET scans and completes with the quantification of the obtained data by means of mathematical frameworks. In this way, physiological parameters can be obtained that can otherwise not be measured *in vivo*, indicating the potential of plant-PET. We believe that *in vivo* imaging in combination with modelling, both at cell and organ scale, are necessary to advance our mechanistic understanding of plant physiology, including dynamics of xylem-transported CO<sub>2</sub> and its relation to woody tissue photosynthesis, phloem characteristics as well as the effects of nutrients, hormones and both micro and macro environmental changes.



# 3

## HIGH-RESOLUTION *IN VIVO* IMAGING OF XYLEM-TRANSPORTED CO<sub>2</sub> IN LEAVES BASED ON REAL-TIME <sup>11</sup>C-TRACING

Parts of this chapter have been published in:

M. Hubeau, M.R. Thorpe, J. Mincke, J. Bloemen, I. Bauweraerts, P.E.H. Minchin, V. De Schepper, F. De Vos, C. Vanhove, S. Vandenberghe, K. Steppe, *High-resolution in vivo imaging of xylem-transported CO<sub>2</sub> in leaves based on real-time <sup>11</sup>C-tracing*. *Front. For. Glob. Chang.* **2019**, *2*.



### **3.1 Abstract**

Plant studies using the short-lived isotope <sup>11</sup>C have greatly advanced our knowledge about the allocation and transport of photosynthates from leaves to sinks. However, delivery of respired CO<sub>2</sub> within the transpiration stream has been recognised as a second pathway of carbon supply to leaves. Here, we use *in vivo* tracing of xylem-transported <sup>11</sup>CO<sub>2</sub> to increase our knowledge on whole plant carbon cycling. We developed a new method for *in vivo* tracing of xylem-transported CO<sub>2</sub> in excised poplar leaves using <sup>11</sup>C in combination with positron emission tomography (PET) and autoradiography. We administered the tracer via the cut petiole and manipulated the transport by excluding light or preventing transpiration to show the applicability of both techniques in visualising and quantifying CO<sub>2</sub> transport dynamics. Irrespective of manipulation, some tracer was found in main and secondary veins, little of it was fixed in minor veins or mesophyll, while most of it diffused out the leaf. Transpiration, phloem loading and CO<sub>2</sub> recycling were identified as mechanisms that could be responsible for the transport pathways of internal CO<sub>2</sub>. Both <sup>11</sup>C-PET and autoradiography can be successfully applied to study xylem-transported CO<sub>2</sub>, towards better understanding of leaf and plant carbon cycling, and its importance in different growing conditions.

## 3.2 Introduction

Within trees, the flow of carbon between organs and metabolic processes or storage pools plays an important role for the overall plant carbon cycle (Litton *et al.* 2007; Epron *et al.* 2012). Since the main pathway for carbon transport considered in research on carbon allocation is the phloem, which distributes sugars to sink tissues, a multitude of techniques have been designed to monitor the fate of assimilated sugars. In particular, isotopic techniques, either based on tracing of stable or unstable isotopes, have recently gained increased interest (Epron *et al.* 2012; Bahn *et al.* 2013; Hubeau & Steppe 2015).

Recent research has shown that CO<sub>2</sub> derived from above- and belowground respiration is transported with the transpiration stream in trees (Teskey *et al.*, 2008; Aubrey & Teskey, 2009; Bloemen *et al.*, 2013b; Steppe *et al.*, 2015; Bloemen *et al.* 2016a; Teskey *et al.* 2017), thereby representing a second important transport pathway of the plant carbon cycle. CO<sub>2</sub> in solution is in equilibrium with other carbonate species. It reacts with water to form carbonic acid (H<sub>2</sub>CO<sub>3</sub>) which, in turn, can dissociate to bicarbonate (HCO<sub>3</sub><sup>-</sup>) and carbonate (CO<sub>3</sub><sup>2-</sup>) by losing one or two hydrogen ions (H<sup>+</sup>), respectively. The concentration of these species in solution is depending on the pH with the dominant form being CO<sub>2</sub> and bicarbonate for the reported xylem pH (4.5-7.4) of woody species (Teskey *et al.*, 2008). A fraction of the respired CO<sub>2</sub> is fixed (Stringer & Kimmerer 1993; McGuire *et al.* 2009; Bloemen *et al.* 2013c, 2015; Steppe *et al.* 2015; Tarvainen *et al.* 2017; Wittmann & Pfanz 2018), potentially contributing to the amount of carbon available for metabolic processes. Bloemen *et al.* (2013b) have pulse-labelled the transpiration stream of field-grown poplar trees using the stable isotope <sup>13</sup>C to trace respired CO<sub>2</sub> transport at the tree level, finding that 3 to 17 % of the tracer was immobilised in the tree, including 0.3 to 2% in the leaves. Similar experiments have been performed at the level of branch (McGuire *et al.*, 2009; Bloemen *et al.*, 2013c) and leaf (Bloemen *et al.* 2015; Stutz *et al.* 2017; Stutz & Hanson 2019a, b).

The impossibility of <sup>13</sup>C-tissue analysis to allow measurements in real-time during experimental manipulations at high spatial and temporal resolution currently hinder our understanding of the importance of xylem-transported CO<sub>2</sub> in plant carbon cycling. Studies investigating the dynamics of xylem-transported CO<sub>2</sub> are therefore scarce. Here, we investigate whether short-living radioactive isotopes can help (Hubeau & Steppe 2015). <sup>11</sup>C has a half-life of 20.4 min and has been exploited mostly for dynamic studies



aiming to understand the controls on distribution of recent photosynthates (Minchin & Thorpe, 2003). Several methodologies can be used. Using scintillation detectors, with radiation shielding to delineate regions of interest (ROI), a range of phenomena has been studied concerning phloem physiology, for example in root apices (Pritchard *et al.* 2004), roots (Farrar *et al.* 1995), properties of the long-distance transport pathway (Troughton *et al.* 1974; Minchin & Thorpe 1984), in leaves (Pickard *et al.*, 1993), and in reproductive organs (Roeb & Britz 1991; Thorpe *et al.* 1993). The low spatial resolution of this method is not a problem for measurement of long-distance tracer transport since the flow at the boundary from one contiguous region to another can be inferred (e.g. Minchin & Thorpe, 2003). With positron autoradiography, complementary snapshots can show tracer distribution at a much higher spatial resolution (Pritchard *et al.*, 2004), which has also been demonstrated by our group (Bloemen *et al.*, 2015; Hubeau *et al.*, 2019b; Epila *et al.* 2018; Mincke *et al.*, 2018). With PET imaging, it is possible to combine good spatial resolution (0.7 – 4 mm) with high time resolution (5 – 60 s), and ROIs can be generated after data collection, both for dynamic studies (Jahnke *et al.*, 2009) and to help choose tissue for chemical analysis (Dirks *et al.*, 2012). These studies using <sup>11</sup>C are however few in number, as most plant biology laboratories do not have access to a hospital's radiology department having a cyclotron to generate <sup>11</sup>C. Also, the short half-life of <sup>11</sup>C limits its use to short-term processes, in contrast to the longer-lived carbon isotope <sup>14</sup>C (half-life of 5730 years). On the positive side, <sup>11</sup>C-tracing allows an *in vivo* observation of tracer movement, which has led to significant research progress in topics such as phloem sectoriality (De Schepper *et al.*, 2013), unloading characteristics (Jahnke *et al.*, 2009), leakage-retrieval of photoassimilates along the transport pathway (Minchin & Thorpe, 1987), phloem functioning under changing climate regimes (Hubeau *et al.*, 2018) and carbon allocation to root and fruit parts (Jahnke *et al.*, 2009; Wang *et al.*, 2014). Importantly, non-invasive measurements allow dynamic aspects of a process to be studied, and <sup>11</sup>C therefore provides a powerful tool to reveal the mechanisms of physiological processes (Minchin & Thorpe, 2003; Jahnke *et al.*, 2009; Bühler *et al.*, 2011; Hubeau *et al.*, 2018). Here, we demonstrate another use of this tool, studying CO<sub>2</sub> transport in the xylem.

To this end, we designed a new method that allows *in vivo* monitoring of xylem CO<sub>2</sub> transport in leaves based on <sup>11</sup>C-tracing and PET in combination with autoradiography. In nearly all previous plant studies, <sup>11</sup>C has been supplied to the plant as airborne <sup>11</sup>CO<sub>2</sub>,

with the aim of gaining insight into photoassimilate production and transport, and phloem functioning. Here, we utilized a PET scanner to dynamically trace  $^{11}\text{C}\text{O}_2$  in excised leaves that had received aqueous  $^{11}\text{C}\text{O}_2/\text{H}^{11}\text{C}\text{O}_3^-$  buffer via the cut petiole to investigate and unravel the interplay between xylem architecture and xylem-transported  $\text{CO}_2$  as a substrate for photosynthesis in leaves (Stringer & Kimmerer 1993; Bloemen *et al.* 2015; Stutz *et al.* 2017; Stutz & Hanson 2019a, b). The  $^{11}\text{C}$ -PET technique was complemented by  $^{11}\text{C}$ -positron autoradiography, giving a snapshot in time with a much higher spatial resolution. Simple manipulations were performed to highlight both the high amount of process-level knowledge that can be extracted through this technique, and also the applicability of both imaging techniques. The overall goal was to shed light on the interplay and importance of  $\text{CO}_2$  flows in a leaf after arrival in leaf xylem: convection in xylem, diffusion within the leaf and photochemical fixation. To that end, we performed two manipulation experiments regarding photosynthesis and gas exchange within one half of a leaf, hypothesising that (i) excluding light would stop  $\text{CO}_2$  fixation in the dark region, and (ii) stopping gas exchange and thus transpiration within a region would prevent the local convective movement of  $\text{CO}_2$  resulting in no fixation. The aims of this study were therefore to indicate: (i) the feasibility of  $^{11}\text{C}$ -PET for plants using a small-animal PET scanner, (ii) the research potential of  $^{11}\text{C}$ -PET to trace short-term transport processes in plants, (iii) the complementarity of  $^{11}\text{C}$ -PET and autoradiography, and (iv) new insights into xylem-transported  $\text{CO}_2$  fixation by the use of diagnostic treatments.

### **3.3 Materials and methods**

#### **3.3.1 Plant material**

For this study, 20-cm long poplar cuttings (*Populus × canadensis* Moench 'Robusta') were planted early April 2012 in 4-L pots containing a commercial potting mixture (DCM, Grobbendonk, Belgium) and slow-releasing fertiliser (Basacote Plus 6M, Compo Benelux nv, Deinze, Belgium), and were grown within a growth chamber at the Faculty of Bioscience Engineering, Ghent University, Belgium. Temperature was controlled day and night at 25°C and photosynthetically active radiation (PAR) was provided with densely packed fluorescent lamps (TLD 80, Philips Lighting NV, Eindhoven) from 8 h until 22 h. The cuttings were watered every two days. The leaves used for the experiments were selected to be similar in age and size.

### 3.3.2 Experimental setup and $^{11}\text{C}$ -labelling

Since  $^{11}\text{C}$  is a short-living isotope, the experiment was performed close to a cyclotron (18/9 MeV, IBA, Belgium). The proximity allowed quick transport of the produced  $^{11}\text{C}$  to the INFINITY imaging lab of Ghent University, Ghent, Belgium. There,  $^{11}\text{CH}_4$  produced from the  $(p, \alpha)$  nuclear reaction in the cyclotron on a nitrogen target was oxidised in a synthetic train to yield  $^{11}\text{CO}_2$  as described by Landais & Finn (1989). The captured  $^{11}\text{CO}_2$  gas was immediately bubbled through “carrier solution” (50 mM KOH with 500 mM TRIS buffer at pH 6.4) giving  $^{11}\text{C}$ -labelled  $\text{CO}_2$  solution, which was subsequently supplied to the cut petiole of an excised leaf. Under these conditions 90% of the  $^{11}\text{C}$  is present as  $\text{HCO}_3^-$  and 10% as  $\text{CO}_2$  in a dynamic equilibrium.

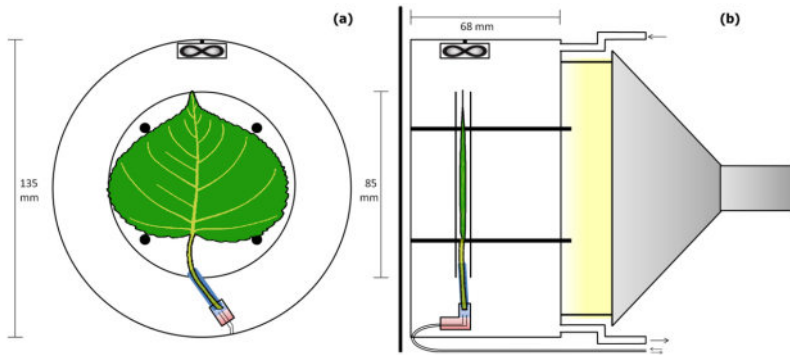


**Fig. 3.1** PET imaging setup with the leaf inside the cuvette. (a) Transversal view of the cuvette. The four screws kept the leaf lamina in place, while the blue polysiloxan kept the petiole fixed in the plastic container. The pink-red two-component glue was used to fix the 0.6 mm tubes inside the plastic container. (b) Sagittal view of the cuvette. The leaf was surrounded by two plexiglass plates to increase positron retention. Air flowing into the cuvette passed by the fan to maximise air mixing throughout the cuvette, and air flow across the leaf lamina. The light source was attached to the cuvette using three metal screws. Tubes were guided along the bottom of the cuvette.

Real-time  $^{11}\text{C}$ -tracing was performed on an excised leaf in a plexiglass cylindrical airtight labelling cuvette (135 mm inner diameter and 68 mm depth, Fig. 3.1), which was kept just below atmospheric pressure to avoid leakage of  $^{11}\text{CO}_2$  out of the leaf cuvette. Air flow ( $1.5 \text{ L min}^{-1}$ ) was generated using a pump (model 2-Wisa, Hartmann & Braun, Frankfurt am Main, Germany) at the end of the pathway (Fig. 3.2). Before entering a dew point generator (Li-610, Li-COR, Lincoln, TE, USA), air entered a 50 L buffer vessel. Relative

humidity (RH) and temperature of the air entering the cuvette were controlled using the dew point generator. RH and air temperature averaged ( $\pm$  SD) over the labelling periods were  $28.4 \pm 0.8\%$  and  $30.2 \pm 0.6^\circ\text{C}$ , respectively. A small fan (20 x 20 x 7.5 mm; Sunon, Kaohsiung, Taiwan) was installed close to the air inlet, so as to stir and direct airflow over both surfaces of the leaf (Fig. 3.1). For radiation safety, air exiting the leaf cuvette was bubbled through KOH solution (50 mM) to remove  $^{11}\text{CO}_2$ , before passing to the pump. A fibre-optic light source (Model FL-4000, Walz Mess und Regeltechnik, Effeltrich, Germany) provided PAR of  $926 \mu\text{mol m}^{-2} \text{s}^{-1}$  at the leaf surface (Fig. 3.1b).

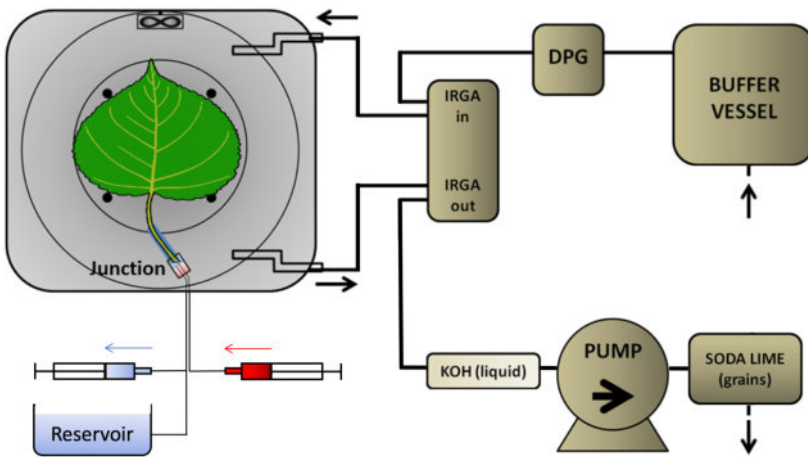


**Fig. 3.2** Flow schedule of the PET imaging setup. The PET detectors (dark-grey around the leaf cuvette) were shielded from most of the tubing in which  $^{11}\text{CO}_2$  was likely present. Ambient air was drawn by a pump that was placed near the end of the pathway to prevent leaks of radioactive gas. The air passed through a 30-L buffer vessel, a dew point generator (DPG), to and from the leaf cuvette via two infra-red gas analyser channels (IRGA), to a KOH trap. As a final safety measure, all air passed from the pump through a granular soda lime trap. The excised leaf received non-labelled solution from a reservoir open to the atmosphere, which was large enough to maintain a constant pressure at the leaf. Tracer was delivered to a small volume in the junction from the 3-mL syringe (red) while simultaneously withdrawing unlabelled solution from the junction into the other syringe (blue). Solution from the reservoir then continued to supply the leaf xylem.

The leaf petiole was cut under water to avoid air entry. Before leaf excision, the leaf petiole was collared with polysiloxane material (Xantopren, Heraeus Kulzer, GmbH, Hanau, Germany) and, immediately after excision, the cut end of the petiole was sealed using the

polysiloxane to a solution-filled junction (elbow shaped – 1.5 mL volume), thereby connecting the petiole to two vinyl tubes (Fig. 3.2). The two tubes (inner diameter of 0.6 mm) were connected to the junction using two-component glue (Loctite, Düsseldorf, Germany). With two tubes connected to the leaf, carrier solution could be continuously available to the leaf from a reservoir, and labelled solution could be delivered directly to the petiole via the other. The latter was typically done two hours after leaf excision. To minimise the delay for decaying tracer to reach the leaf, two 3-ml syringes were used (Fig. 3.2). Simultaneously, carrier solution in the junction was withdrawn into one syringe, while about 2 mL labelled solution (7.4 MBq) was delivered from the other. After that, carrier solution from a reservoir, which was connected to the same tubing as the withdrawing syringe using a three-way valve, was still a source for transpiration. For trouble-shooting, arrival of the <sup>11</sup>C label to the leaf petiole was assessed through the PET scanner's real-time decay event counter. In order to reduce random coincident events in the scanner, the syringe of <sup>11</sup>C labelled solution, together with the water source and most of the tubing, were shielded from the PET detector using stackable lead blocks (Fig. 3.2).

### 3.3.3 <sup>11</sup>C-imaging techniques

<sup>11</sup>C-imaging is based on the radioactive decay of <sup>11</sup>C, which occurs with a half-time of 20.4 minutes. <sup>11</sup>C decays to <sup>11</sup>B through emission of a positron (β<sup>+</sup>-radiation), with a maximum energy of 0.96 MeV, and a neutrino (ν<sub>e</sub>) (Eq. (3.1)) (Bailey *et al.* 2005):



This positron moves along a random path, suffering collisions by which its energy reduces until it can annihilate with an electron (Fig. 1.2). In water - and in tissue - that zig-zag path is about 5 mm long, but the radial range for an <sup>11</sup>C-nuclide is less, 1.1 mm, and 90 % of the positrons stop within 2.2 mm (Cho *et al.* 1975; Jødal *et al.*, 2003). Annihilation results in two high-energy photons, which move off in opposite directions (Fig. 1.2 in Chapter 1) (Bailey *et al.*, 2005). These photons (γ-rays) each have an energy of 511 keV and can easily penetrate thick layers of plant tissues: e.g. the thickness of wood that is required to reduce the intensity of a beam by one half is approximately 29 cm as indicated in Chapter 2 (Bailey *et al.*, 2005). In PET, these γ-rays are registered, whereas in autoradiography, mainly the positrons are detected.

### <sup>11</sup>C-PET analysis

In this study, a LabPET8 scanner (TriFoil Imaging, Chatsworth, CA, USA) was used which was located at the INFINITY imaging lab of Ghent University, Ghent, Belgium. This scanner has been designed to image small animals (mice and rats) for preclinical research. Detectors consist of LGSO ( $\text{Lu}_{0.4}\text{Gd}_{1.6}\text{SiO}_5:\text{Ce}$ ) and LYSO ( $\text{Lu}_{1.9}\text{Y}_{0.1}\text{SiO}_5:\text{Ce}$ ) scintillation crystals and avalanche photodiodes which are sensitive to a determined range of photon energy and placed along a cylindrical surface. When an <sup>11</sup>C-atom decays inside this cylinder, and the positron-electron annihilation results into two  $\gamma$ -photons, two opposing detectors register an incoming photon. Dedicated software filters such co-occurring photons, indicative of a decay event, and generates spatial probability graphs of all decay events (Fig. 1.2 in Chapter 1) over a certain time frame. Technical advances (such as the time-of-flight PET or enhanced reconstruction algorithms) are continuously increasing spatial and temporal resolution of these scanners. A significant portion of <sup>11</sup>C-positrons can escape the leaf lamina and therefore reduce sensitivity and spatial resolution (Alexoff *et al.* 2011; Partelová *et al.* 2016). The leaf was therefore additionally fixed between two circular plexiglass plates (diameter of 85 mm and thickness of 2.5 mm) spaced 0.5 cm from each other, improving the sensitivity, but reducing the resolution of the images. These plates were attached concentrically to the cuvette by four plastic screws (Fig. 3.1).

LabPET software version 1.12.1 (TriFoil Imaging, Chatsworth, CA, USA) was used to reconstruct the PET data with a temporal resolution of 5 min, and the resulting output was analysed using AMIDE (<http://amide.sourceforge.net>, GNU General Public License version 2.0 (GPLv2)). Since radioactivity is characterized by an exponential decay, it is required to apply decay-correction when evaluating tracer activity over time. This correction is automatically implemented in the LabPET software for all reconstructions. Hence, the obtained PET images as well as the derived ROI tracer profiles derived therefrom are mutually comparable at different time stamps over the course of the experiment. To avoid ambiguity, we use the term “tracer” to mean “decay-corrected activity”, reserving the term activity for the detected events. Voxel tracer values were normalized to the maximum voxel value in the time-series. The PET images map average tracer density within a slice of specified thickness, centred on the leaf. In this work, we used a 30 mm thickness, enclosing both leaf and discs, to ensure that all annihilations were accounted for. A background ROI outside the leaf was used to subtract a background

count-rate. PET data was recorded for 60 and 100 min for control and treated leaves, respectively.

#### *<sup>11</sup>C-autoradiography setup*

At the end of the experiment, the cuvette was taken out of the PET scanner. After removing the leaf from the cuvette and from the petiole container, the leaf was wrapped in transparent cellophane to prevent contamination of the imaging plate while radioactivity was imaged by positron autoradiography, exposing the adaxial side of the leaf by direct contact with an imaging phosphor plate for 5 min, after which the plate was digitally scanned (Cyclone Plus Phosphor imager, Perkin Elmer, Waltham, MA, USA) and visualised using OptiQuant version 5.0 (Perkin Elmer, Waltham, MA, USA) (Hubeau *et al.* 2019b; Mincke *et al.* 2018). Images are not mutually corrected for radioactivity.

### **3.3.4 Manipulation experiments**

To test the robustness of our setup and to demonstrate the applicability of both techniques (PET and autoradiography) to visualise and quantify dynamics of internal CO<sub>2</sub> transport and fixation, experiments were conducted on three different leaves: (i) not treated; (ii) half-shaded, with one half of the leaf lamina (including midrib) shaded by covering half of the plexiglass plate closest to the light source (Fig. 3.1b), aiming to minimise photosynthetic activity; (iii) half-greased, with one half of the leaf greased on both the abaxial and adaxial surfaces using translucent petrolatum (i.e. petroleum jelly or vaseline) before the leaf was installed in the labelling cuvette to prevent gas exchange.

## **3.4 Results**

### **3.4.1 Microclimate**

The microclimate of each experiment is characterized by an average vapour pressure deficit of  $3.02 \pm 0.12$ ,  $2.70 \pm 0.19$ , and  $2.51 \pm 0.04$  kPa in the non-treated, shaded, and greased leaves, respectively. Average transpiration rates of the non-treated, shaded, and greased leaf were  $1.877 \pm 0.819$ ,  $1.050 \pm 0.526$ , and  $1.483 \pm 0.232$  mmol m<sup>-2</sup> s<sup>-1</sup>, respectively, and photosynthetic rates averaged around  $18.59 \pm 5.63$ ,  $13.10 \pm 3.96$  and  $11.42 \pm 1.48$  μmol CO<sub>2</sub> m<sup>-2</sup> s<sup>-1</sup>, respectively. The half-shaded and half-greased leaves thus

transpired 48 % and 21 % less water, and assimilated 33 % and 42 % less carbon, respectively, compared to the control leaf.

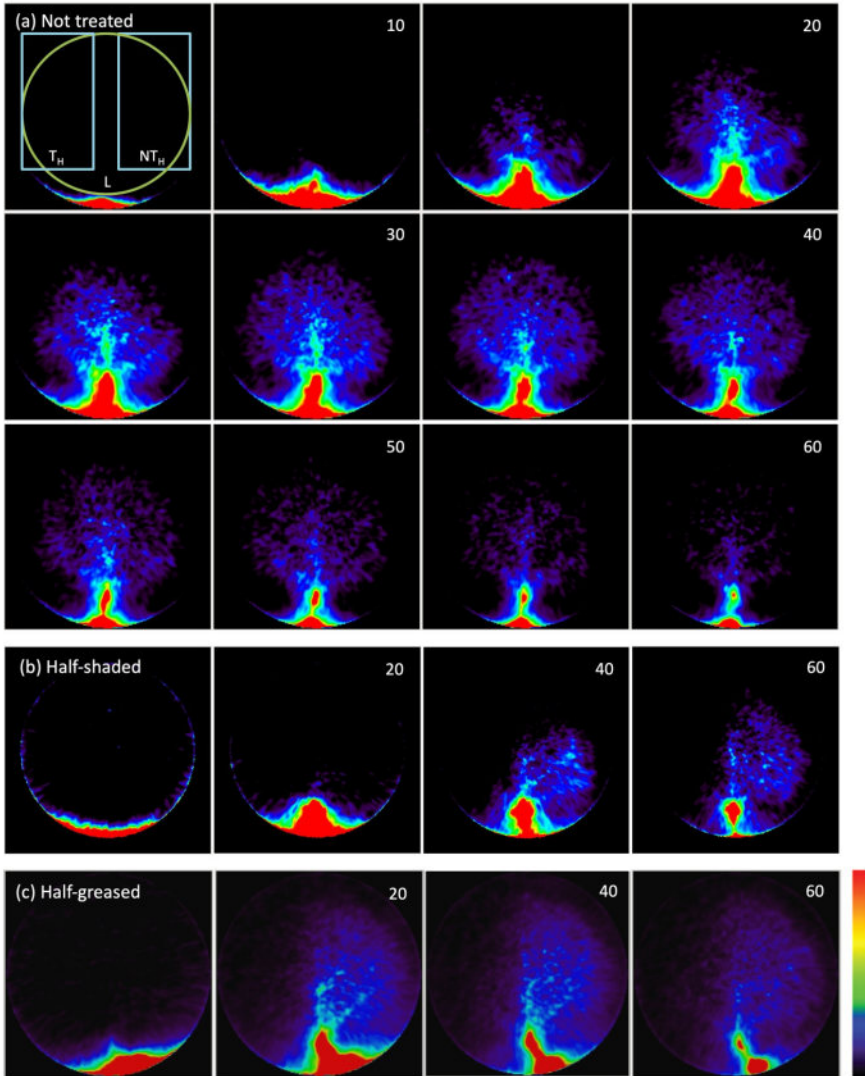


**Fig. 3.3**  $^{11}\text{C}$  PET images of a (a) non-treated leaf, (b) half-shaded leaf, (c) half-greased leaf. Numbers in the upper right corner show time (minutes) after the start of labelling. Each image shows the decay-corrected sum of all decay events in the last 5-min (a) or 20-min (b,c) interval. The first PET image of (a) displays the ROIs of the leaf (L), treated ( $T_H$ ) and non-treated ( $NT_H$ ) halves that were used to create time-series (Figure 6) for all conditions (non-treated, shading and grease). Colours varying from black to red represents no to high tracer activity as indicated by the colour bar.



### 3.4.2 Images

The PET image sequence of tracer density for each leaf (Fig. 3.3a-c) shows tracer moving from the petiole through the leaf to gradually reveal both the main vein and basal secondary veins in the non-treated regions of all leaves. Little was visible in the shaded leaf-half (Fig. 3.3b), but surprisingly, there were indications of tracer in the greased leaf-half (Fig. 3.3c). The PET image sequences showed that most tracer was not fixed, as it declined steeply after passing a maximum, showing loss of tracer, presumably by outgassing via stomata.

Autoradiographs showed that some activity remained in each leaf (Fig. 3.4). The labelling pattern of non-treated regions was similar, and activity extended all the way to the perimeter of the leaves in minor veins, with little to none in the mesophyll. In the shaded region, all minor veins were labelled, but density declined towards the leaf perimeter much more in comparison with the non-treated half. In the half-greased leaf, the tracer was visible over the greased region, but hardly any tracer reached the leaf perimeter. The labelling pattern of the non-greased region was more intense compared to exposed regions in the other leaves, suggesting that tracer was fixed in minor veins and even mesophyll. However, replications are needed to further confirm our results.

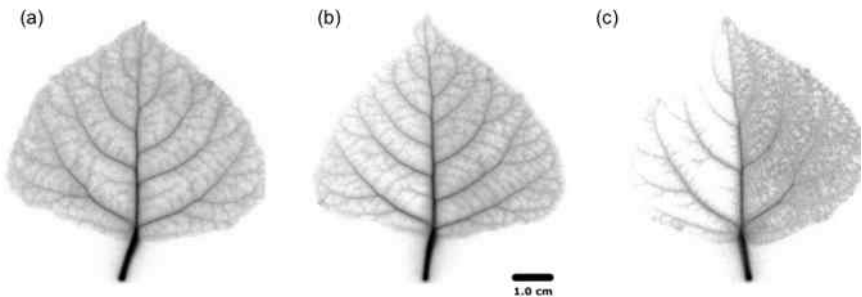


**Fig. 3.4** <sup>11</sup>C positron autoradiograms for the three differently leaves; (a) non-treated leaf, (b) half-shaded leaf, (c) half-greased leaf.

### 3.4.3 Tracer dynamics

More details of tracer dynamics were derived from the time-series of tracer within specified regions (regions are shown in Fig. 3.3). Profiles of tracer within each leaf and its two halves (Fig. 3.5a-c) showed that most of the tracer entering a leaf was in due course lost from it by the end of the experiments (in particular observable in the longer experiments of 100 min). It is also obvious that movement was much slower in the half-shaded leaf than in either the non-treated or half-greased leaves. Tracer concentration within each ROI reached a peak around 25, 45 and 20 min for the non-treated, half-shaded and half-greased, respectively. After that, the ROI content was found to be well-described by an exponential.

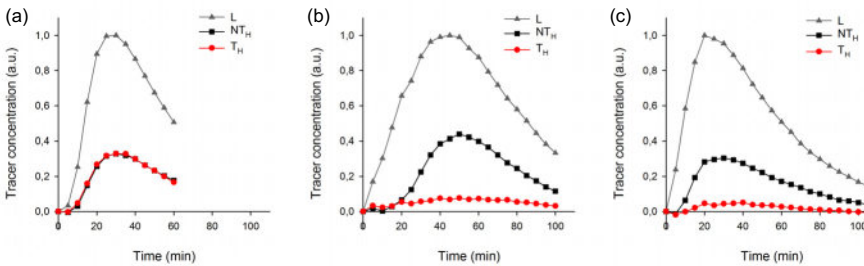


**Fig. 3.5** The temporal decay-corrected activity profiles of the ROIs L, T<sub>H</sub> and NT<sub>H</sub> (as indicated on Figure. 4a) for all conditions: (a) non-treated leaf, (b) half-shade leaf, and (c) half-greased leaf. The activity was summed per 5 minutes for each ROI.

## 3.5 Discussion

### 3.5.1 <sup>11</sup>C-based tracing of xylem CO<sub>2</sub> transport and fixation

So far, the role of xylem CO<sub>2</sub> transport in plants has been mainly studied using unstable <sup>14</sup>C (Stringer & Kimmerer, 1993; Hibberd & Quick, 2002) and stable <sup>13</sup>C (McGuire *et al.* 2009; Bloemen *et al.* 2013b, c; Stutz *et al.* 2017; Stutz & Hanson 2019a, b) isotopes. Opposed to the destructive sampling procedures to investigate <sup>13</sup>C- or <sup>14</sup>C-tissue enrichment, both of these labelling methods allow collecting dynamic data. Specifically, a combination of <sup>13</sup>C-labelling and gas exchange measurements coupled to a tunable diode laser absorption spectroscope permits to study assimilation and efflux of xylem-transported CO<sub>2</sub> in real-time (Stutz *et al.* 2017; Stutz & Hanson 2019a). Additionally, it has been recognised that Bremsstrahlung radiation from <sup>14</sup>C-atoms is energetic enough to be detected *in vivo* by scintillation detectors (Black *et al.* 2012). However, these studies suffer

from a poor spatial resolution as measurements are performed on organ-level. Here, we have demonstrated that xylem CO<sub>2</sub> transport in tree leaves can be traced continuously *in vivo* and with high spatial resolution (~ 1 mm) when PET-based <sup>11</sup>C-analysis is used, mimicking the transport and fixation of respired CO<sub>2</sub>. It is important to gain better insights into the movement and fixation of respired CO<sub>2</sub> to develop a comprehensive framework on carbon cycling and its implications in leaves and plants.

Most of the <sup>11</sup>C-label applied at the leaf petiole was distributed throughout the leaf via the leaf veins. Water and sugar transport mainly occur through the main vein because of the heterobaric vein structure in poplar, which causes a strong compartmentalization of the leaf mesophyll by bundle sheath extensions (McClendon 1992). Highest activity is retained in the petiole and veins which can be explained by the fact that xylem-transported <sup>11</sup>CO<sub>2</sub> is being assimilated. These findings correspond with the results of McGuire *et al.* (2009) where branches were allowed to transpire water enriched with <sup>13</sup>CO<sub>2</sub>. In that study, 35 % (SE = 2.4) of the label got assimilated via woody tissue photosynthesis and little was found in the leaves and petioles. Reduction in assimilated label with distance from the source can be related to assimilation of xylem-transported CO<sub>2</sub> ( $A_x$ ) in proximal parts and outgassing. After activity curves reached a maximum, there was a decline, showing that, apart from  $A_x$ , CO<sub>2</sub> in the xylem diffused out of the leaf, presumably through stomata, which can be related to the slightly acidic pH of xylem sap. This is safe to assume because the activity profiles are decay-corrected, meaning that a difference in perceived activity can solely be attributed to metabolic changes, i.e. in- or outflow of tracer in the ROI.

To test the applicability of the proposed <sup>11</sup>C-labelling for studying xylem CO<sub>2</sub> transport dynamics, we manipulated xylem CO<sub>2</sub> transport rates in one leaf half using shading or grease treatments while keeping the other leaf half untreated as reference. Both PET and autoradiographic image analyses showed differences in xylem CO<sub>2</sub> transport between leaf halves, with a substantially lower amount of label in the treated leaf half ( $T_H$ ) as compared with the untreated one ( $NT_H$ ) (Fig. 3.5b-c). Interestingly, the amount of tracer measured in secondary veins on the autoradiographs was hardly influenced by the treatments (Fig. 3.4). Further transport to minor veins and mesophyll was however clearly reduced by both treatments. Shading half of the leaf surface reduced transpiration by half compared to the control leaf. With half the transpiration and half the

leaf shaded, transpirational water flow into the leaf reduced, reducing the amount and flow velocity of  $^{11}\text{C}$ -labeled solution into the unshaded half. Accumulation of  $^{11}\text{C}$  in the shaded half (Fig. 3.4b) indicated that water was also flowing into this region despite the exclusion of light. This can be explained by limited transpiration under dark conditions comparable to nocturnal transpiration, which is not uncommon and known to occur in poplar (Caird *et al.* 2007; Dawson *et al.* 2007; Zeppel *et al.* 2014). Transpiration in the darkened leaf half will even be stronger compared to a nocturnal leaf as atmospheric conditions in the cuvette were drier than during a typical night. The treatment with grease completely blocks leaf transpiration (as observed in for example Gribaudo *et al.* (2001) and Shackel *et al.* (1990)) and was therefore expected to stop local convective movement of  $^{11}\text{CO}_2$  into the greased leaf half. According to the cohesion-tension theory, the driving force for water transport disappears in the absence of transpiration, but interestingly we observed that the  $^{11}\text{C}$ -label did enter the secondary veins of the greased leaf half, but that import into the minor veins and mesophyll was hampered (Fig. 3.4c). Diffusion within the secondary veins cannot be the explanation as  $\text{CO}_2$  would have been able to diffuse only 0.06 mm in one hour, given the diffusion coefficient of  $\text{CO}_2$  in water of only  $1.6 \times 10^{-9} \text{ m}^2 \text{ s}^{-1}$  (Nobel 2009; Steppe *et al.*, 2007), and leaves of poplar are heterobaric, hindering any gas transport. We suggest three mechanisms that could be responsible. Firstly, the petiole of the cut leaf was submerged in the label solution that had a water potential close to zero. This is higher than the water potential present in the transpiring leaf. Given the induced water potential difference between label solution and leaf blade, the label-containing solution was most likely transported into the greased half of the leaf. Secondly, any ongoing phloem loading and transport of sugars from the leaf lamina towards the petiole would generate a small counter-flow of water in the xylem (Tanner & Beevers 2001; Windt *et al.* 2006) explaining the  $^{11}\text{C}$ -label in the greased leaf half (Fig. 3.4c). Thirdly, with no transpiration, but in the presence of light, some locally respired  $\text{CO}_2$  in the cells near the secondary veins might have been recycled and photosynthesised into sugars, producing an osmotic gradient, which drove the transport of labelled  $^{11}\text{C}$  from the petiole to the leaf veins (Nikinmaa *et al.*, 2013, Stroock *et al.*, 2014). Fixation of respired  $\text{CO}_2$  has indeed been shown to occur in bundle sheath cells, surrounding the vascular bundle, as has been described by (Griffiths *et al.* 2013).

### 3.5.2 Why should we measure xylem CO<sub>2</sub> transport in plants?

Within trees, the transport of locally respired CO<sub>2</sub> via the transpiration stream represents an additional pathway of carbon transport, counterflowing the phloem transport of recent photosynthates from leaves to sink tissues (Teskey *et al.*, 2008). Aubrey & Teskey (2009) measured xylem CO<sub>2</sub> transport at the bottom of *Populus deltoides* trees as an estimate of internally transported belowground respired CO<sub>2</sub> and estimated that half of belowground respired CO<sub>2</sub> was transported internally instead of diffusing into the soil environment thereby showing that current soil CO<sub>2</sub> efflux-based methods underestimate the autotrophic component of soil respiration. Bloemen *et al.* (2013b,c) used stable isotope <sup>13</sup>C labelling approaches to trace respired CO<sub>2</sub> in field-grown trees and detached branches, respectively. They observed that the applied <sup>13</sup>C label was assimilated in different tissues, indicating that xylem-transported CO<sub>2</sub> can be fixed and hence contribute to tree biomass. At leaf level, such fixation occurred in the petiole mainly (Bloemen *et al.*, 2013b,c). However, a fraction of xylem-transported CO<sub>2</sub> was also transported in the leaf vasculature and into the leaf mesophyll (Bloemen *et al.*, 2015). This way, photosynthetically active cells lying adjacent to the transpiration stream might be fed with carbon from a different source than the atmospheric one (Hibberd and Quick, 2002; Griffiths *et al.*, 2013). In our study, we also observed patterns in the half-shaded and half-greased leaf that point to the importance of fixing internally cycled CO<sub>2</sub>. A substantial amount of internally transported CO<sub>2</sub> remained in the vasculature where it could be fixed by cells adjacent to the veins. With PET, it is not possible to detect in what molecular structure <sup>14</sup>C is present (e.g. dissolved CO<sub>2</sub> or <sup>14</sup>C-sucrose). Dirks *et al.* (2012) therefore used a set-up with a combination of <sup>14</sup>C and <sup>13</sup>C labelling to acquire both dynamic tracer images and molecular structure information (from NMR analysis). Janacek *et al.* (2009) showed that photosynthesis near veins, presumably utilising xylem-transported CO<sub>2</sub>, is important for plant fitness, by comparing untreated plants with plants with silenced chlorophyll synthase in the veins, which showed a marked reduction in growth. This process of CO<sub>2</sub> recycling is receiving increasingly more attention as more evidence accumulates to support this as an important mechanism to sustain both carbon supply and hydraulic functioning under drought conditions (Schmitz *et al.* 2012; Vandegehuchte *et al.*, 2015; Cernusak & Cheesman 2015; Bloemen *et al.*, 2016b; De Baerdemaeker *et al.*, 2017, Chen *et al.* 2018).

### 3.5.3 The power of imaging $^{11}\text{C}$ -labeled compounds in plant research

The potential of  $^{11}\text{C}$ -positron emission tomography ( $^{11}\text{C}$ -PET) in plant studies remains largely untapped (Hubeau & Steppe, 2015). In past studies,  $^{11}\text{C}$ -tracing has been used to study the transport speed of phytomolecules such as plant hormones (e.g. methyl jasmonate in Thorpe *et al.*, 2007) and photoassimilates (Kikuchi *et al.*, 2008), and  $^{11}\text{C}$ -imaging has been used to visualise the phloem pathway for part of the plant (Kawachi *et al.* 2006 ; Jahnke *et al.*, 2009; De Schepper *et al.*, 2013; Hubeau *et al.*, 2019b) or the entire plant (Kawachi *et al.*, 2011). The acquired tracer profiles can be implemented in mathematical models to study sugar loading, sugar translocation, radial sugar leakage and sugar unloading (Bühler *et al.*, 2011; Minchin, 2012; Bühler *et al.*, 2013; Hubeau *et al.*, 2019b).

Those studies that have applied radio-isotopes to trace xylem  $\text{CO}_2$  transport used almost exclusively the long-living  $^{14}\text{C}$  isotope. For instance, Stringer & Kimmerer (1993) allowed excised leaves to transpire dissolved  $^{14}\text{C}$  label. Using autoradiography, they confirmed that xylem  $\text{CO}_2$  was transported in the leaf vasculature to different leaf sections. In addition, Stringer & Kimmerer (1993) performed light manipulation experiments and observed that a large amount of the  $^{14}\text{C}$  label applied to the leaf diffused into the atmosphere. Our group performed  $^{11}\text{C}$ -based autoradiography to analyse  $A_x$  which resulted in a static autoradiogram (Bloemen *et al.*, 2015; Hubeau *et al.*, 2019a; Epila *et al.*, 2018; Mincke *et al.*, 2018). In this study, our PET  $^{11}\text{C}\text{CO}_2$  imaging method provides the first continuous *in vivo* data on xylem  $\text{CO}_2$  transport, allowing us to study the transport pathways of xylem  $\text{CO}_2$  transport in plants at high temporal resolution. With a relatively simple set of manipulation experiments we could already see detailed differences between treatments and gathered detailed spatial and temporal carbon distribution maps. Due to their fine spatial and temporal resolution, and the fast decay of the activity, the PET images appear noisy and mottled (for the 7.4 MBq activity we used), but signal to noise was markedly improved for time-series of ROI content (Fig. 3.5), integrating large volumes of the PET images.

The high energy (511 keV) of the photons resulting from  $^{11}\text{C}$ -decay penetrates tissue and allows *in vivo* detection of tracer in thick plant tissues. This would allow our observations of xylem  $\text{CO}_2$  transport at leaf level to be expanded to branch or tree level, as performed already to study photosynthate allocation in the phloem of small trees

(Jahnke *et al.* 1998; De Schepper *et al.*, 2013). Also, since <sup>11</sup>C is a short-living isotope with a half-life of 20.4 min, it allows repeated pulse labelling on the same plant so that changes in transport properties can be monitored. A next step would be to design a set-up in which the imaged leaf remains attached to the tree branch or stem (Hubeau & Steppe, 2015), although higher <sup>11</sup>C-activity than the 7.4 MBq that we used in our experiment would be necessary in order to resolve different tissues. For thicker samples, such as woody stems, the high energy of  $\gamma$ -rays in PET would give useful results, using phantoms to account for attenuation.

### **3.6 Conclusion**

Our results highlight the potential importance of internal CO<sub>2</sub> for the plant in the production of local sugars in the vasculature with an important impact on water transport in the study leaves. With <sup>11</sup>C-PET we were able to extract valuable information, both qualitative (high-resolution images) and dynamic (tracer profiles), on the movement of internal CO<sub>2</sub>. A combination of PET with positron autoradiography, which took little additional effort, resulted in even more information on the distribution of carbon inside a leaf under different conditions. Although, more replications are needed to further confirm our findings, the obtained results yields promising outlooks for future experiments, potentially in combination with related techniques such as micro-CT for structural information, SPECT for functional information with heavier isotopes and MRI to visualise and quantify water flow in xylem and phloem.





# 4

## ASSIMILATION OF XYLEM-TRANSPORTED CO<sub>2</sub> BY WOODY TISSUE PHOTOSYNTHESIS UNRAVELLED THROUGH <sup>11</sup>C-POSITRON AUTORADIOGRAPHY ENFORCED WITH <sup>13</sup>C-LABELLING

Parts of this chapter have been published in:

J. Mincke, M. Hubeau, J. Courty, B. Brans, C. Vanhove, S. Vandenberghe and K. Steppe, Normalization of <sup>11</sup>C-autoradiographic images for semi-quantitative analysis of woody tissue photosynthesis. *Acta Horticulturae* **2018**, 35-42



## 4.1 Abstract

Locally respired CO<sub>2</sub> in woody species can either diffuse to the atmosphere, dissolve in the xylem sap to be transported with the transpiration stream or be assimilated via woody tissue photosynthesis ( $P_{wt}$ ). We lack important knowledge about the relevance of  $P_{wt}$  in the carbon balance because it is not straightforward to quantify its dynamics within smaller spatial dimensions. Additionally, assimilation of xylem-transported CO<sub>2</sub> ( $A_X$ ) to sugars inside woody tissues has mainly been assumed but has never been confirmed. To assess  $P_{wt}$  we traced xylem-transported <sup>11</sup>C<sub>2</sub> in detached poplar branches. The applicability of positron autoradiography was proven to be successful in visualising internal CO<sub>2</sub> transport (Chapter 3) it was used here to quantify the dynamics of CO<sub>2</sub>-transport occurring within the submillimetre range, while manipulating light exposure to the branch. We evidenced assimilation of internal CO<sub>2</sub> into sugars by performing <sup>13</sup>C-experiments. Experiments using <sup>18</sup>F-fluorine were conducted to study water transport since <sup>18</sup>F-radionuclides are not assimilated and solely transported. The acquired insights confirmed the results of <sup>11</sup>C-experiments performed on light-excluded branches where CO<sub>2</sub> was found to be merely transported by the sap. Combination of stable and unstable isotope experiments led to two main conclusions. We unequivocally showed that xylem-transported CO<sub>2</sub> is fixed by photosynthetic cells in both branches and leaves providing building blocks and energy to woody tissues; and that  $P_{wt}$  is highly light responsive along the pathway of xylem-transport towards the leaves.

## 4.2 Introduction

Besides water, xylem cells transport several other compounds throughout the entire plant like e.g. hormones and nutrients (Lucas *et al.* 2013; Schuetz *et al.* 2013). An important molecule in this respect is carbon dioxide (CO<sub>2</sub>). Mainly through respiration, it gets inside the tree where it exists in equilibrium with other carbonate species. The proportion of these species in solution is dependent on the pH with the dominant form being CO<sub>2</sub> (aq) and bicarbonate for woody species (Teskey *et al.* 2008). In this way, respired CO<sub>2</sub> is piled up to a substantially higher concentration (often between 3 and 10 % and sometimes up to 26 %) than the atmospheric CO<sub>2</sub> concentration (~ 0.04 %) (Teskey *et al.* 2008; Ávila *et al.* 2014). Upon dissolution in xylem sap, CO<sub>2</sub> is transported throughout the plant where it can either diffuse into the atmosphere or be fixed by chloroplasts present in the bark, xylem rays, and pith tissues (Bloemen *et al.* 2016b). This latter process may as such be regarded as a recycling mechanism that contributes to the total carbon budget of the plant. Photosynthesis performed by these tissues will be referred to as woody tissue photosynthesis ( $P_{wt}$ ), as described by Saveyn *et al.* (2010).  $P_{wt}$  is, however, often overlooked with respect to the plant carbon budget. Furthermore, we lack knowledge about its role in plant survival, especially during drought/changing climatic conditions, i.e. when uptake of atmospheric CO<sub>2</sub> is limited (Vandegheuchte *et al.* 2015; De Baerdemaeker *et al.* 2017). This may be related to the ongoing debate about whether CO<sub>2</sub> is merely accumulating in xylem cells or stripped from them to be assimilated through woody tissue photosynthesis (Cernusak & Cheesman 2015; Vandegheuchte *et al.* 2015). Aside from  $P_{wt}$ , anaplerotic fixation of CO<sub>2</sub> is described (Berveiller & Damesin 2008; Ávila *et al.* 2014; Hilman *et al.* 2019), which falls out of the scope of this study and will therefore not be discussed.

As highlighted in Chapter 1, it has merely been assumed that retention/accumulation of xylem-transported CO<sub>2</sub> in woody tissues is related to  $A_x$  by  $P_{wt}$  through exposure of photosynthetically active radiation (PAR) as described by experiments using <sup>13</sup>C-labelling in branches and leaves (e.g. McGuire *et al.* 2009; Bloemen *et al.* 2015; Stutz & Hanson 2019) or CO<sub>2</sub> gas exchange measurements (e.g. Wittmann *et al.* 2001; Salomón *et al.* 2018). Moreover, McGuire *et al.* (2009) labelled detached branches of sycamore (*Platanus occidentalis* L.) by allowing them to transpire an enriched <sup>13</sup>CO<sub>2</sub> aqueous solution. An average of 35 ± 2.4 % (SE) of the supplied label was taken up from the

treatment water and accumulated in the woody tissues of the branches, with smaller amounts in leaves and petioles. Another study focused on detached poplar leaves (*Populus x canadensis* Moench 'Robusta') and observed higher tissue  $^{13}\text{C}$ -enrichment under higher vapour pressure deficit (VPD) (Bloemen *et al.* 2015). Among tissues, highest enrichment was observed in the petiole and the veins, regardless of the VPD treatment. In these studies,  $^{13}\text{C}$ -enrichment of the tissues was observed but actual incorporation of the  $^{13}\text{C}$ -label into  $^{13}\text{C}$ -containing sugars was not tested. With regard to  $\text{CO}_2$  gas exchange measurements, a dynamic  $^{13}\text{C}$ -labelling study using tunable diode laser absorption spectroscopy performed on leaves of *Populus deltoides* and *Brassica napus* indicated that rates of  $A_X$  increased with increasing xylem [ $^{13}\text{CO}_2^*$ ] and transpiration (Stutz & Hanson 2019a). Wittmann *et al.* (2001) found that apparent  $\text{CO}_2$  respiration (measured as  $\text{CO}_2$  release) in twigs clearly reduced in the light, which was suggested to be attributed to light-driven refixation within chlorenchyma tissues. A study performed by Salomón *et al.* (2018) on *Populus tremula* L. used a mass balance approach to estimate diel contributions of  $P_{wt}$  (represented as storage flux in the mass balance) and xylem-transported  $\text{CO}_2$  to stem respiration. Also in these gas exchange studies,  $A_X$  has been assumed since conversion of xylem-transported  $\text{CO}_2$  into sugars was not measured. Only the study of Stringer and Kimmerer (1993) showed actual assimilation of a xylem-transported  $^{14}\text{C}$ -label into sugars in petioles, veins and lamina of poplar leaves (*Populus deltoides* Bartr. ex Marsh) under illumination. However, this study was limited to  $A_X$  in leaves, and therefore extrapolation to woody tissues assimilation might be challenging. Taken all together, each of the aforementioned studies (based on  $^{13}\text{C}$ - and  $^{14}\text{C}$ -labelling or gas exchange) contribute to the understanding of the fate of respired  $\text{CO}_2$  regarding  $P_{wt}$ , but only provide indications that xylem-transported  $\text{CO}_2$  is fixed in woody tissues as it could equally be retained in the tissues as  $\text{CO}_2$ .

Less detail is available on dynamic processes at smaller spatial scales (e.g. (sub)millimetre) since either  $^{13}\text{C}$ - and  $^{14}\text{C}$ -sample procedures are used, which require a certain amount of sample mass, or measurements inform on the integrated response of a branch/stem segment enclosed in a gas exchange chamber. Results of these studies typically report on integrated responses but neglect underlying short-range dynamics at finer spatial scale. To this end, radioactive  $^{11}\text{CO}_2$ -based experiments have been performed on plants in combination with the positron emission tomography (PET) and positron autoradiography. However, studies focusing on xylem-transported  $^{11}\text{CO}_2$  are scarce and

have to date only been performed on leaves (Dirks *et al.* 2012; Bloemen *et al.* 2015; Hubeau *et al.* 2018, 2019a, b).

Positron autoradiography is put forward to study dynamics of  $P_{wt}$  and xylem transported  $\text{CO}_2$  at branch level (Hubeau *et al.* 2019a). Detached poplar branches (*P. tremula*) were allowed to take up an aqueous solution enriched with radioactive  $^{11}\text{C}$ -labelled  $\text{CO}_2$ . By applying aluminium foil and/or grease on parts of the branches we aimed at better understanding the short-term response of light exposure and transpiration on  $P_{wt}$  at fine spatial resolution. The same treatments were applied on leaf lamina to assess the possibility whether branch respired  $\text{CO}_2$  is actually fixed in leaves. In addition,  $^{13}\text{C}$ -based measurements were performed and analysed with liquid chromatography-mass spectrometry (LC-MS) to unequivocally identify whether carbon tissue enrichment under light exposure is attributed to accumulation or actual  $A_X$  by  $P_{wt}$ . Lastly,  $^{18}\text{F}$ -labeling experiments were performed with  $^{18}\text{F}$ fluorine being a proxy for water. By visualising both water and  $^{11}\text{C}\text{CO}_2$  transport we aimed at demonstrating that by illumination of branches with PAR,  $\text{CO}_2$  is stripped from the xylem sap to be assimilated by  $P_{wt}$ .

## 4.3 Materials and methods

### 4.3.1 Plant material

For this study, five 40-cm poplar cuttings (*Populus tremula* L.) were planted on March 23, 2016 in 30-L pots containing commercial potting mixture (Peltracom, Gent, Belgium). They were grown in a greenhouse for two months at the Faculty of Bioscience Engineering, Ghent University, Belgium (51.053693°N, 3.706487°E) and had a height ranging between 90 – 120 cm. All trees (N = 5) were subsequently transported to the small animal imaging facility of Ghent University (INFINITY lab) at least 24 h before measurement (Pickard *et al.* 1993). There, they were placed outside during the experiments (51.023237°N, 3.725782°E) and were watered every day. The nine branches used for stable ( $^{13}\text{C}$ , N = 4) and unstable ( $^{11}\text{C}$  and  $^{18}\text{F}$ , N = 5) isotopic experiments had an average ( $\pm$  SE) length and diameter at the cut end of  $23.2 \pm 2.3$  cm and  $2.5 \pm 0.1$  mm, respectively.

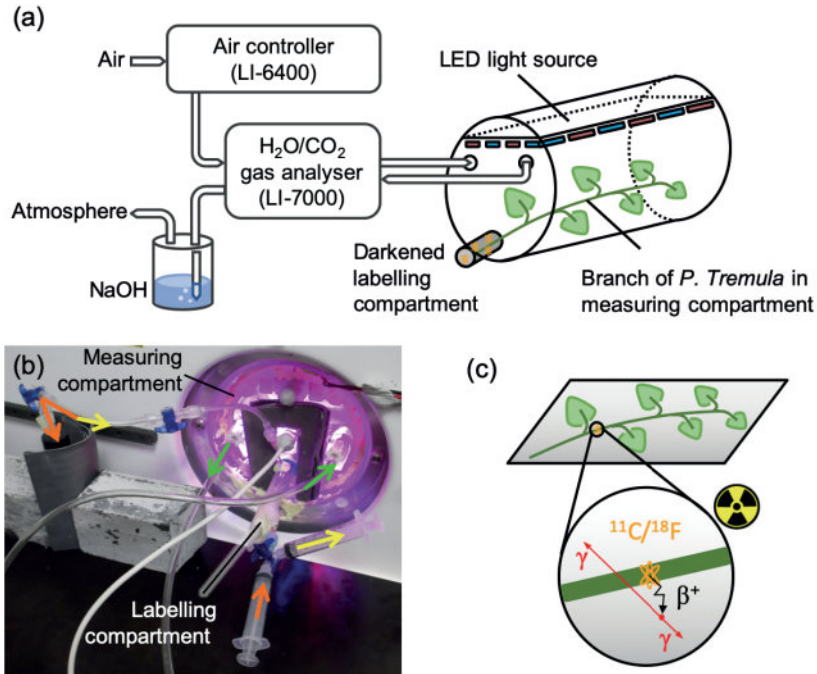


**Figure 4.1** Protocol of  $^{11}C$ - and  $^{18}F$ -labelling (a), label administration procedure (b), and positron autoradiography (c). (a) Schematic of the experimental set-up displaying a *P. tremula* branch inside an airtight chamber. A small dark labelling compartment containing the radioactive isotopes (indicated in orange) and the cut end of the branch is hermetically sealed from the measurement compartment containing the illuminated part of the branch. The incoming  $[CO_2]$  is maintained at 400 ppm by a LI-6400 system while the water content and  $[CO_2]$  entering and leaving (green arrows in (b)) the measurement compartment is analysed by a LI-7000 system, to calculate the transpiration and photosynthetic rate, respectively. For safety measures, the leaving air is stripped from all radioactivity by bubbling it through a basic NaOH solution. (b) The labelling compartment was connected to two syringes. The first syringe, provided the tracer to the cut end of the branch (orange arrow). Just before introducing the tracer, the plunger of the second syringe was pulled to remove the non-labelled aqueous solution (yellow arrow). While doing so, a needle introduced at the headspace of the labelling compartment ensured in- and outflow of air (represented by the two-headed arrow having a yellow and orange colour, respectively) so that no vacuum was created in the labelling compartment. For safety measures, the outflowing air was directed to a container filled with soda lime as to strip the  $^{11}CO_2$  from the air. (c) Schematic of positron autoradiography where a *P. tremula* branch is in close contact with a rectangular phosphor plate detecting the radioactivity ( $\beta^+$  positron and to a lesser extent  $\gamma$ -ray) inside the branch.

### 4.3.2 Experimental set-up and radioactive $^{11}\text{C}$ - and $^{18}\text{F}$ -labelling

Carbon transport and water movement in detached poplar branches were imaged following exposure to a labelled solution containing either dissolved  $^{11}\text{CO}_2$  ( $N = 4$ ) or  $^{18}\text{F}$ -fluorine ( $N = 1$ ), respectively. Both radioactive tracers were produced using a cyclotron (18 MeV protons, IBA, Belgium) of Ghent University Hospital. For  $^{11}\text{C}$ -production, protons were accelerated towards an  $\text{N}_2/\text{H}_2$  (5%) target. The  $(p, \alpha)$  nuclear reaction resulted in the formation of  $^{11}\text{CH}_4$  which was subsequently oxidized via cobalt oxide to yield  $^{11}\text{CO}_2$  as described by Landais & Finn (1989). Subsequently, the captured  $^{11}\text{CO}_2$  gas was bubbled through a 40 mM citric acid buffer at a set pH of  $\sim 5.8$ , resembling the pH of xylem sap in young *P. tremula* branches (pH  $\sim 6.4$ , which is in the reported range of 4.5 – 7.4 for woody species (Teskey *et al.* 2008)). The pH of the labelled solution was slightly more acidic than the xylem sap favouring the  $^{11}\text{C}$ -label being dissolved as  $\text{CO}_2$  (aq) (70 %) over bicarbonate (30 %). Once the tracer is taken up, equilibrium reactions will shift according to the pH of the xylem sap (Butler 1991). Concerning the  $^{18}\text{F}$ -experiment related to water movement, high energy protons were accelerated inside the cyclotron (18 MeV protons, IBA, Belgium) to bombard  $^{18}\text{O}$ -enriched water causing a  $(p, n)$  nuclear reaction resulting in an aqueous solution containing  $^{18}\text{F}$ -ions. The half-life of  $^{18}\text{F}$  is higher than  $^{11}\text{C}$  (109.8 vs. 20.8 minutes) making the former easier to handle with regard to timing.

Radioactive labelling (one branch at a time) was performed in a cylindrical airtight chamber consisting of two compartments: a polypropylene labelling compartment (6 mL in volume) in which the cut end of the branch was exposed either the  $^{11}\text{C}$ - or  $^{18}\text{F}$ -labeled solution, and a plexiglass measurement compartment (135 mm inner diameter and 200 mm length) containing leaves and light source (Fig. 4.1a). The position of a detached branch within the chamber was fixed by applying polysiloxane material (Terostat-IX, Henkel AG & Company, KGaA, Düsseldorf, Germany) around the branch at the intersection of both compartments to separate them. With respect to the  $^{11}\text{C}$ -experiments, extra grease (Vacuum grease, Dow Corning, Auburn, MI, USA) was added around the branch segment coming out of the polysiloxane material which ensured airtightness between both labelling and measurement compartments as to avoid assimilation of evaporated  $^{11}\text{CO}_2$  from the solution ( $^{11}\text{CO}_2$  (aq) to  $^{11}\text{CO}_2$  (g)) by leaf photosynthesis. To avoid leaf wilting the labelling compartment was filled with five mL of non-labelled buffer solution at least 45 min prior to the arrival of the label. A 5-mL volume of this solution was sufficient given



the averaged transpiration rate ( $\pm$  SE) of  $0.49 \pm 0.06$  mL h<sup>-1</sup>. Because of the isotope's decay, the labelling system was designed to give a minimal time-delay for the tracer to enter the branch after labelling. Therefore, the labelling compartment was connected to two 5-mL syringes (Fig. 4.1b). The first syringe, containing the <sup>11</sup>C- or <sup>18</sup>F-labeled solution, provided the tracer to the cut end of the branch. Just before introducing the tracer (orange arrow), the plunger of the second syringe was pulled to remove the non-labelled aqueous solution (yellow arrow). Five mL of <sup>11</sup>C- or <sup>18</sup>F-enriched solution was supplied to the branch with an activity at labelling ranging from 125.8 – 436.6 MBq and 740 MBq, respectively. A needle introduced at the headspace of the labelling compartment ensured in- and outflow of air (represented by the two-headed arrow having a yellow and orange colour, respectively) under these procedures so that no vacuum was created in the compartment. For safety measures, the outflowing air was directed to a container filled with soda lime as to strip the <sup>11</sup>CO<sub>2</sub> from the air. The branches were labelled for 1.5 h, after which they were taken out of the chamber to immediately perform autoradiography. For radiation safety purposes, the labelling compartment was shielded using lead sheets which darkened it at the same time (Fig. 4.1a).

The microclimate inside the measurement compartment was characterized by an average ( $\pm$  SE) relative humidity (RH), air temperature and vapor pressure deficit of  $60.8 \pm 6.6$  %,  $32.4 \pm 0.7$  °C and  $1.9 \pm 0.3$  kPa, respectively. Photosynthetic rate averaged ( $\pm$  SE) over the labelling periods was  $1.09 \pm 0.31$   $\mu$ mol CO<sub>2</sub> m<sup>-2</sup> s<sup>-1</sup> which is low for poplar leaves and could be explained by the low PAR intensity of about 250  $\mu$ mol photons m<sup>-2</sup> s<sup>-1</sup> that was provided at leaf and branch level by ten red and ten blue LED lights (GreenPower LED strings 0842 LF Red and WPO 83 LF Blue, Philips, The Netherlands). Common photosynthetic rates of *Populus tremula* range from 10-20  $\mu$ mol CO<sub>2</sub> m<sup>-2</sup> s<sup>-1</sup> but are obtained at 1000-1500  $\mu$ mol photons m<sup>-2</sup> s<sup>-1</sup> PAR. However, the results found in this study are equally valid since PAR at crown level of trees is around 300  $\mu$ mol m<sup>-2</sup> s<sup>-1</sup> for a 12 h period (0700–1900 h) (Saveyn *et al.* 2010). Additionally, the low flow rate (0.4 L min<sup>-1</sup>) of the air containing 400 ppm CO<sub>2</sub> that was supplied using a portable photosynthesis system (model LI-6400, Li-Cor Inc., Lincoln, Nebraska, USA) was not able to remove the transpired water properly. Hence high RH (60% vs. 40% in the room) likely hampered normal photosynthesis. The water content of the air entering and leaving the measurement compartment was measured with a gas analyser (model LI-7000, Li-Cor

Inc., Lincoln, Nebraska, USA). To prevent radioactivity from coming into the atmosphere, the outflowing air was directed to a 1 M sodium hydroxide solution.

### 4.3.3 Positron autoradiography

At the end of the experiment, the branch was taken out of the cylindrical chamber and positioned on an autoradiographic phosphor plate (Super Resolution storage phosphor plate, Perkin Elmer, Waltham, Massachusetts, USA) of which the crystals are principally excited by positrons leaving the tissue (Fig. 4.1c). To prevent contamination of the imaging plate, the branch was first wrapped in transparent cellophane before making contact with the phosphor plate. After 10 – 20 min exposure, the plate was read-out digitally (Cyclone Plus Phosphor imager, Perkin Elmer, Waltham, Massachusetts, USA) and visualised using OptiQuant version 5.0 (Perkin Elmer, Waltham, Massachusetts, USA) to obtain image files (5806x2995 pixels – 24.58x12.68 cm) (e.g. Fig. 4.2c,d of the corresponding branches in Fig. 4.2a,b).

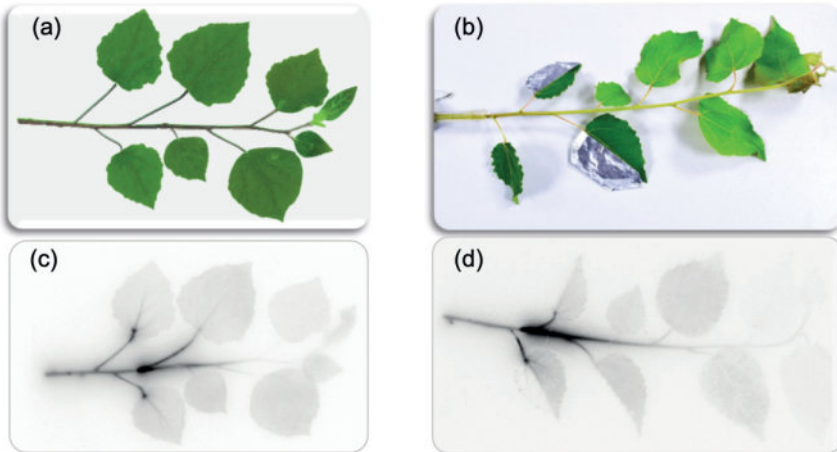


**Figure 4.2** Photographs of a poplar branch without (a) and with (b) partially aluminium- and grease-covered leaves. Autoradiographic image obtained after  $^{11}\text{C}$ -labelling of the corresponding poplar branch without (c) and with (d) partially aluminium- and grease-covered leaves. In (b, d) the following covering methods were applied on the leaves starting from the cut-end: grease, aluminium, grease + aluminium.

### 4.3.4 Image analysis

Information on the acquired autoradiographs was extracted using Fiji software. A line profile (10-pixel width) of the branch was drawn on the image obtained from each of the

experiments. The recorded activity (arbitrary units - a.u.) on the line profile was subsequently plotted in function of the branch length. To allow mutual comparison of the activity profile plots (e.g. Fig. 4.3a,b;), normalisation was performed according to the procedure described by Mincke *et al.* (2018) (Text box 4.1). To indicate the part of the branch that was in the dark labelling chamber auxiliary grey bars on the x-axis as well as a dash-dotted line were added to the profile plots. Green diamonds indicate the onset of petioles on the branch. Note that after each petiole junction, sap flow rate within the branch is slightly reduced because less leaf area is transpiring from that point onwards. Hence, the actual  $^{11}\text{C}$ -activity in the more distal branch pieces could be higher than the recorded activity since it took more time for the activity to reach these parts.

Different decay of  $^{11}\text{C}$  and  $^{18}\text{F}$  isotopes results in positrons with a different energy, making the normalisation procedure described by Mincke *et al.* (2018) invalid for direct comparison of  $^{18}\text{F}$ - and  $^{11}\text{C}$ -experiments. Therefore, the scale on the Y-axis was manually set for the  $^{18}\text{F}$ -experiment to equal the one of the  $^{11}\text{CO}_2$ -based profile plots to alleviate comparison between different experiments.

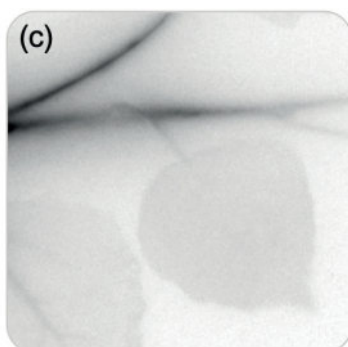
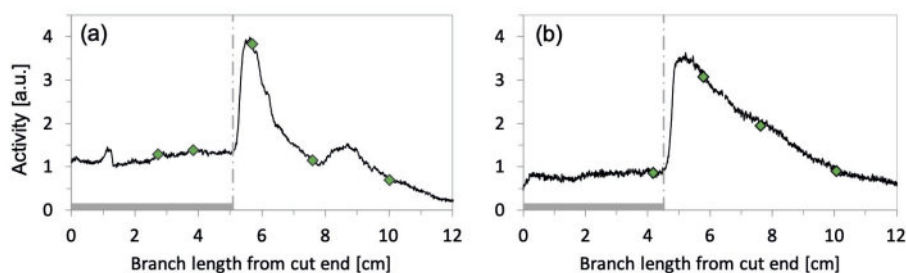


**Figure 4.3** Profile plot of the normalized activity (expressed in arbitrary units) across the entire length of a branch without (a) and with (b) partially covered leaves. Grey bars along the x-axis indicate part of the branch that was in the labelling chamber. Branches were illuminated from dash-dotted line. Diamonds represent starting origins of petioles. (c) Zoom of autoradiograph of the first branch (from Fig. 4.2c) where the petiole of leaf 4 is covering the branch section, preventing close contact with the detection plate.

**Text box 4.1 Normalisation of  $^{11}\text{CO}_2$  experiments**

The recorded activity in the section of the branch that was inside the dark labeling compartment (grey box in Figure 4.3a, b) shows a nearly horizontal line. It was theorized that this signal should be attributed to transport of  $^{11}\text{CO}_2$  molecules along with water in the xylem. However, the intensity of this initial signal was different between the branches after digital read-out of the phosphor plates (not shown), which can be related to the time-dependency of radioactivity. Indeed, the starting radioactivity, starting time and duration of exposure of the branch to the phosphor plate differed for each of the branches, which had a direct effect on the amount of radioactivity exposed to the phosphor plates during autoradiography. Therefore, images were normalised for following factors to allow semi-quantitative comparison:

*Experimental duration time*

The total time the branches transpired the radioactive solution was different for each branch. Because this affects the total amount of activity taken up by the branch, normalization was applied for the experimental duration.

*Radioactivity*

As radioactivity is dependent on time, other time-related ‘correction factors’ were considered. The starting activity and exposure time to the phosphor plates was different for each branch. The activity exposed to the autoradiographic plates was calculated by integration of the universal law of radioactive decay (Eq. (4.1)) from start to end of the exposure of the branch to the phosphor plate.

$$A(t) = A_0 e^{-\lambda t} \quad (4.1)$$

with  $A(t)$  the remaining radioactivity at time  $t$  when starting activity was  $A_0$  of radioisotope with decay constant  $\lambda$ . The latter can be derived from the half-life (Eq. (4.2)), where  $t_{1/2} = 20.4$  minutes for  $^{11}\text{C}$ :

$$t_{1/2} = \frac{\ln(2)}{\lambda} \quad (4.2)$$

### *Transpiration rate*

In addition to these time-related parameters, also transpiration should be accounted for as has been shown in earlier experiments (e.g. Bloemen *et al.* 2013c; Stutz *et al.* 2017). This was accomplished by calculating the average transpiration rate (difference in water vapor entering and leaving the treatment compartment per unit of time) transpired during labeling.

The stem profile plots were subsequently normalized by multiplying the raw profile activity plots (not shown) with the three above-mentioned factors, where a higher experiment time, recorded radioactivity or transpiration rate resulted in a lower normalization factor. After normalisation, the recorded activity of the branch segments inside the labeling compartment (grey boxes in Fig. 4.3) were at a similar activity levels, indicating the validity of the described normalisation procedure. This 'baseline activity' was subsequently set to  $\sim 1$  a.u. to allow better visual assessment of the profile plots. Small discrepancies between the 'baseline activity' of each branch might be attributed to differences in plant architecture and chlorophyll content in the branch tissues. When not all of the described factors are measured, simple equalisation of the 'baseline activity' could be performed instead. However, the resulting profile plots are subsequently not based on physical parameters and could contain masked biological effects.

#### **4.3.5 Manipulation experiments**

To investigate the dynamics of woody tissue photosynthesis, experiments with  $^{14}\text{CO}_2$  were conducted on four different branches: (i) a non-treated branch (Fig. 4.2a), (ii) a branch of which one half (both ab- and adaxial surfaces) of leaf one, two and three from the cut-end (assigning numbers to leaves or petioles in this way will be done throughout the entire manuscript) were treated with either grease, aluminium foil or a combination of grease and aluminium foil (on top of each other; Fig. 4.2b), respectively, (iii) a branch of which sections were covered with either grease, aluminium foil or a combination (Fig. 4.4a), and (iv) a branch that was completely covered with aluminium foil except for petioles and leaf lamina. Aluminium foil and grease (translucent Vaseline) were applied to minimize photosynthetic activity and to prevent gas exchange, respectively. Application of these treatments on leaves and branches were performed to test the hypothesis whether branch respired  $\text{CO}_2$  reaches the leaves to be assimilated, and to

assess the dynamics in light-sensitivity of  $P_{wt}$ , respectively. The treatments were applied when the branch was still attached to the tree, just before detachment under water. Subsequently, the branches were cut at least three times under water to prevent embolism formation in the xylem conduits. To investigate branch water transport, a labelling experiment with  $^{18}\text{F}$  (proxy for  $\text{H}_2\text{O}$ ) was conducted on a non-treated branch.

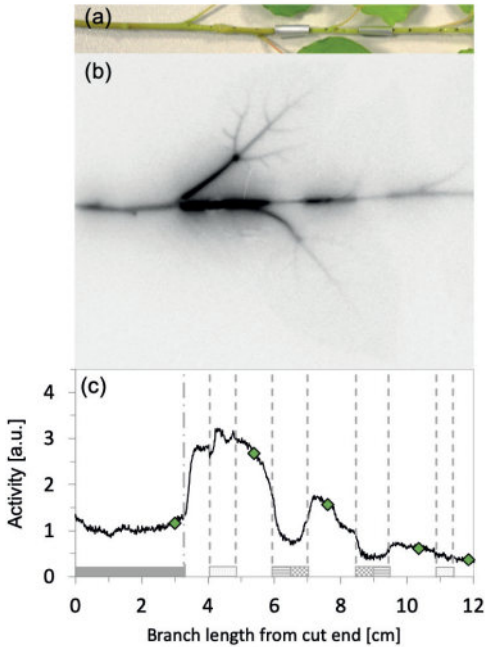


**Fig. 4.4** Autoradiographic image (b) and normalised stem profile plot (c) of a branch (a) were inter-petiole zones were covered with grease (white dotted); aluminium foil (horizontal lines); and the combination of grease and aluminium foil (checker-board). Diamonds represent starting origins of petioles. Vertical lines provide visual support for the delineation of the zones.

#### 4.3.6 Activity profile plot processing

To analyse the correlation between measured activity (a.u.) in the profile plot and branch position (cm), a linear regression model was fitted in RStudio (R Core Team (2018), RStudio: Integrated Development Environment for R. RStudio, Inc., Boston, MA, USA, version 1.1.453) using the *lm* function, in which the branch position was treated as the independent variable whereas measured activity was treated as dependent variables. This approach was performed on profile plots of both non-treated branch segments (Fig. 4.3a,b) from maximum activity to where activity equalled average activity measured in the dark. To indicate that measured activity in each of the branches had a different variance, weighted least squares were added in the fitting process. Normality of the

measured activity was tested and found by the Shapiro-Wilk test (on a 5% significance level), justifying the application of a linear model. The linear regression model resulted in an intercept, slope and P-value indicating whether or not the slope and/or intercept were significant at a 5 % significance level ( $P < 0.05$ ). The ratio of the slope to the intercept represents the percentual change in radioactivity (i.e. decrease in this study) per cm.

#### 4.3.7 Experimental set-up $^{13}\text{C}$ -labelling

To investigate whether the xylem dissolved  $\text{CO}_2$  was actually assimilated by  $P_{wt}$  different detached poplar branches ( $N = 4$ , originating from the same trees as the branches used in the  $^{11}\text{C}$ - and  $^{18}\text{F}$ -experiments) were exposed to an aqueous solution containing dissolved  $^{13}\text{CO}_2$  (Fig. 4.5a). Therefore, a solution was prepared containing 40 mM KCl to facilitate solution uptake and transfer in the xylem tissue of the detached branches (Zwieniecki *et al.* 2001). This KCl solution was appended with  $^{13}\text{C}$ -labelled  $[\text{NaHCO}_3]$  (98 atom %  $^{13}\text{C}$ , Sigma Aldrich, Overijse, Belgium) to a target concentration of 5.88 mM, which corresponds to the measured  $\text{CO}_2$  concentration ( $[\text{CO}_2]$ ) dissolved in the sap solution previously observed in *Populus* spp. (Salomón *et al.* 2018, 2019a). The solution had a pH of  $\sim 7$  which is in the reported range of 4.5 – 7.4 for woody species (Teskey *et al.* 2008). This pH is adequate to minimize the conversion of bicarbonate into  $\text{CO}_2$  and as such limit label loss to the atmosphere during the course of the experiment. Once the label solution is taken up into the slightly acidic xylem sap (Teskey *et al.* 2008), equilibrium reactions will shift toward the formation of aqueous  $\text{CO}_2$  (Butler 1991). Each of the branches was cut under water to prevent embolism formation and was placed in a slightly tilted 50 mL Falcon® tube (Corning, Tewksbury, Massachusetts, USA) containing 10 mL  $^{13}\text{C}$ -label solution. Subsequently, the branches were simultaneously positioned under four 1.5-m-long arrays of red and blue LED lights (GreenPower LED production module deep red/blue, Phillips, The Netherlands), which provided about  $250 \mu\text{mol m}^{-2} \text{s}^{-1}$  PAR at leaf/branch level (Fig. 4.5a). The tubes were packed with aluminium foil to exclude light (and thus  $P_{wt}$ ) from the part of the branch that was inside the tubing. This resembled the lead shielding in the  $^{11}\text{C}$ - and  $^{18}\text{F}$ -experiments. After 1.75 h labelling, the branches were taken out of the solution and cut in parts with a scalpel, separating the branch in the part inside (Da) and the part outside (Li) the darkened tube. The Li part was further subdivided into smaller samples. Both Li and Da samples were subsequently split in xylem and bark (Fig. 4.5a) and flash frozen in liquid nitrogen and stored in a freezer at  $-90^\circ\text{C}$  before further processing.

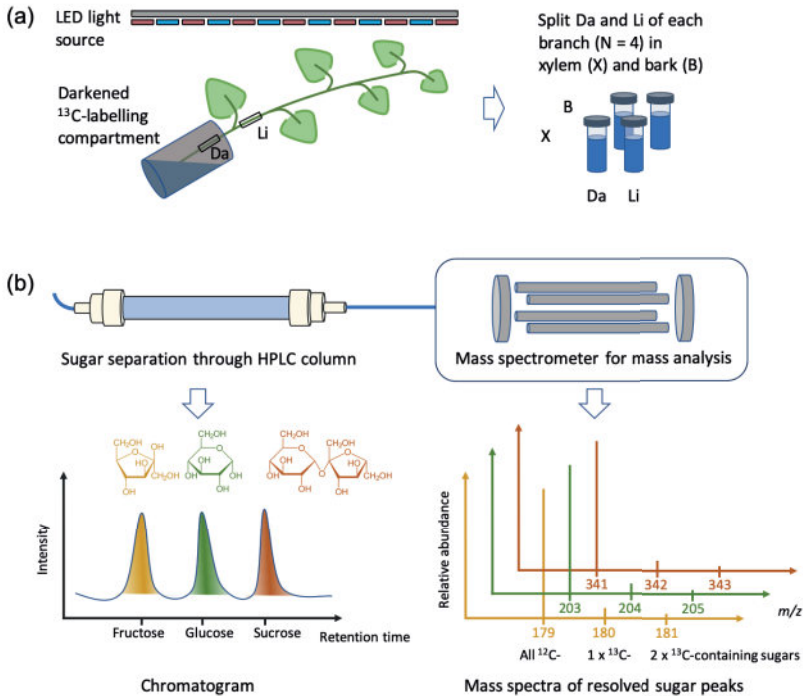


**Fig. 4.5** Protocol of  $^{13}\text{C}$  branch labelling, sample preparation and LC-MS analysis. (a) Schematic of the experimental set-up displaying a *P. tremula* branch inside a darkened labelling tube. After labelling two samples were taken from each branch ( $N = 4$ ), one sample from the darkened labelling compartment (Da) and one that was illuminated (Li). These Li and Da samples were subsequently split in xylem and bark to end up with 4 samples per branch. After flash freezing and storage, these samples were subjected to sugar extraction. (b) Schematic of a high-performance liquid chromatography (HPLC) column separating fructose, glucose and sucrose. Each of these resolved sugar peaks was subsequently ionised ( $\text{H}^-$ ,  $\text{Na}^+$  and  $\text{H}^-$  for fructose, glucose and sucrose, respectively) to be detected by mass spectrometry.

#### 4.3.8 Sugar extraction and LC-MS analysis

Xylem and bark samples were freeze dried, reduced to smaller pieces using a scalpel and grinded to powder in a mortar. To investigate the sugar content at least 20 mg of each sample was weighted and was dissolved in 100 % ethanol (Merck KGaQ, Darmstadt, Germany) to a concentration of  $4 \text{ mg mL}^{-1}$ . To extract the sugars, samples were consecutively placed in warm water bath of  $75^\circ\text{C}$  and  $45^\circ\text{C}$  for 10 min and 160 min,



respectively. Finally, the samples were centrifuged for 10 min at 8800 g (Quentin *et al.* 2015).

The sugars (fructose, glucose and sucrose) dissolved in the supernatant were analysed using liquid chromatography–mass spectrometry (LC-MS). Therefore, the sugars could be separated using an Acquity UPLC HSS T3 Column (Waters Corporation, Milford, Massachusetts, USA – 150 mm length, 2.1 mm internal diameter, 1.8  $\mu\text{m}$  particle size, 45°C column temperature – Fig. 4.5b). A volume of 10  $\mu\text{L}$  was automatically injected onto the column and pumped around using an UltiMate™ 3000 RS pumping system, column compartment and autosampler (Thermo Fisher Scientific, Waltham, Massachusetts, USA). Gradient elution was achieved by using a combination of formic acid (0.1 %) in ultra-pure water and in acetonitrile as solvents (Thermo Fisher Scientific, Waltham, Massachusetts, USA). A flow rate of 0.4  $\text{mL min}^{-1}$  was maintained during the separation. Retention time of fructose, glucose and sucrose were 0.95, 0.96 and 1.03 min, respectively. To be detected by mass spectrometry, the sugar molecules need to be ionized which resulted in mother ions  $[M-H]^-$ ,  $[M-\text{Na}]^+$  and  $[M-H]^-$  for fructose, glucose and sucrose, respectively. Detection of the sugars was done using Q extractive Hybrid Quadrupole-Orbitrap Mass Spectrometer (Thermo Fisher Scientific, Waltham, Massachusetts, USA – Fig. 4.5b). Ionized sugar molecules composed of only  $^{12}\text{C}$ -atoms were selected by  $m/z$  179.056, 203.053 and 341.109 for fructose, glucose and sucrose, respectively (Fig. 4.5b). To detect the sugars having one or two  $^{13}\text{C}$ -atoms, 1.003 was added to  $m/z$  once or twice, respectively.

#### 4.3.9 Sugar quantification

To quantify the amount of sugars (glucose, fructose and sucrose) in the xylem and bark samples calibration curves were constructed using eight points, each containing known concentrations of these sugars. These concentrations were 1, 3, 4, 5, 6, 8, 10 and 12  $\mu\text{g mL}^{-1}$  for fructose; 0.5, 1, 2, 3, 4, 5, 7 and 10  $\mu\text{g mL}^{-1}$  for glucose and 20, 40, 60, 80, 100, 120, 140 and 160  $\mu\text{g mL}^{-1}$  for sucrose. The choice of these calibration concentrations was based on concentrations measured in preliminary test experiments not included in this study. Since  $^{13}\text{C}$  is the naturally occurring isotope of carbon, each of these calibration samples include sugar molecules containing one and two  $^{13}\text{C}$ -atoms and are denoted as  $^{13}\text{C}$ - and  $[2x\ ^{13}\text{C}]$ -sugars (i.e. fructose, glucose or sucrose), respectively. Hence, using the mass

spectra of the resolved sugars (Fig. 4.5b) the calibration curves for these  $^{13}\text{C}$ - and  $[2\times^{13}\text{C}]$ -containing sugars could be constructed by searching for the corresponding  $m/z$  values (see previous paragraph). The specific  $m/z$  values used to construct the calibration curve were the same as those used for detection in the wood samples. The concentrations in  $\text{ng mL}^{-1}$  were converted to  $\text{mg g}^{-1}$  dry matter (DM) using the extraction concentration ( $4 \text{ mg mL}^{-1}$ ). In accordance with the normalization of the profile plots (Text box 4.1; Fig. 4.3a,b), the concentrations were normalized for the transpired volume during the experiment. Student t-test was performed to denote statistical differences between Da and Li samples on a 5 % significance level ( $P < 0.05$ ). When no significant difference in sugar concentration was found between Da and Li samples, a tendency towards a higher/lower concentration was indicated.

## 4.4 Results

### 4.4.1 $^{11}\text{C}$ positron autoradiographic imaging to assess woody tissue photosynthesis and water transport

High detection sensitivity of positron autoradiography was indicated by the profile plot of the uncovered branch (Fig. 4.3a) where a minimum around 8 cm is observed which can be attributed to the petiole of leaf 4 covering the branch from the phosphor plate preventing close contact between them (Fig. 4.3c).

A pronounced light sensitivity of  $P_{wt}$  in poplar branches (Fig. 4.2a, b) was observed when analysing the corresponding autoradiographic images (Fig. 4.2c, d) as indicated by the bright white spot (arbitrary choice) representing a higher number of detected positrons. These bright spots were located after petiole two (Fig. 4.2c) and one (Fig. 4.2d), counting starting from the cut-end, thus representing the branch parts that just left the darkened labelling compartment and were illuminated with PAR. During the experiment,  $^{11}\text{C}$ -tracer accumulated in the illuminated branch parts, suggesting assimilation of xylem-transported  $^{11}\text{CO}_2$  by  $P_{wt}$ . Some activity was also found in leaves, with highest activity in the veins. When leaf halves were covered with grease (leaf 1), aluminium foil (leaf 2), or a combination (leaf 3), almost no signal was detected in the treated zones. It should be noted that all leaves were inside the measurement compartment, whereas parts of the

petioles were sometimes (maximum two per branch as indicated by the green diamonds on the profile plots – Figs. 4.3, 4.4) inside the  $^{11}\text{C}$ -labelling compartment.

Normalised activity profile plots (expressed in arbitrary units) obtained from the autoradiographs of branches without (Fig. 4.2c) and with (Fig. 4.2d) treated leaves are shown in Fig. 4.3a and 4.3b, respectively. The activity measured in the branch inside the dark  $^{11}\text{C}$ -labelling compartment remained rather constant as indicated by the nearly horizontal line, which suggests  $^{11}\text{C}$ -transport only. As confirmed by the bright zones in the autoradiographs (Fig. 4.2c, d), the detected radioactivity reached a maximum where the branch just exited the  $^{11}\text{C}$ -labelling compartment. Averaged ( $\pm$  SE) over both non-treated branches, the maximum activity was  $3.8 \pm 0.3$  times higher than the averaged activity in the  $^{11}\text{C}$ -labelling compartment. The activity decreased quickly after the maximum was reached. A linear regression was applied on both profile plots of the uncovered branches (Fig. 4.3a,b), ranging from where maximum activity was measured to where activity equalled average activity in the dark, and resulted in a significant ( $P < 0.05$ ) decrease in activity of 16% per cm.

To investigate light-sensitivity of  $P_{wo}$ , the same treatments as described for leaves were applied to the branch. Application of grease (white dotted bar on x-axis – Fig. 4.4c) resulted in a 26% lower activity peak in the profile plot compared to non-treated branches (Fig. 4.3a, b). Highest recorded activity in this grease-covered segment was 2.8 times higher than the averaged activity measured in the darkened  $^{11}\text{C}$ -labelling compartment (Fig. 4.4c), whereas the highest recorded activity in the non-treated branches was  $\sim 3.8$  times higher than the averaged activity in the labelling compartment (Fig. 4.3a, b). In contrast, application of aluminium foil (grey horizontal bars) and combination of grease and aluminium foil (checkerboard-filled bars) marked two minima in the normalised profile plots (zones around 6.5 and 9 cm – Fig. 4.4c). In these zones, it appeared that  $\text{CO}_2$  is only transported and not accumulated, similar to the branch inside the  $^{11}\text{C}$ -labelling compartment.

To explore the  $\text{CO}_2$ -transport only hypothesis under light exclusion, an experiment was performed where the entire branch was covered with aluminium foil to block light exposure (Fig. 4.6a). The normalised profile plot showed indeed a nearly horizontal line indicating  $\text{CO}_2$  transport without accumulation or refixation. The observed peak around 5.5 cm is related to the starting point of a petiole (green diamond) which prevented tight

wrapping of aluminium foil around that particular part of the branch segment, allowing exposure to PAR and thus  $P_{wt}$  to occur. The lower signal-to-noise ratio of this profile plot compared to the other profile plots (Figs. 4.3a,b 4.4c) is attributed to the lower starting activity of the particular experiment. As a result, the normalisation factor (Mincke et al. 2018) was higher, amplifying both activity and noise.

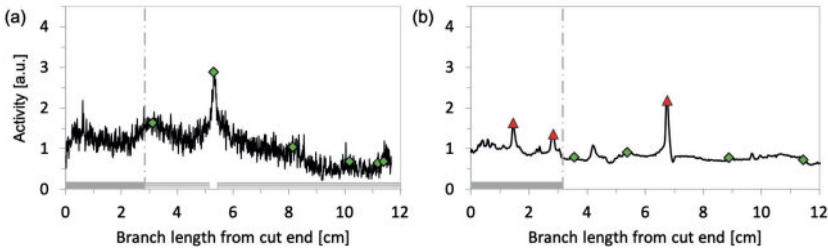


**Fig. 4.6** Normalised stem profile plots of a branch whose stem was completely wrapped with aluminium foil while being labelled with  $^{11}\text{C}$  (a) and a branch that was not covered and labelled with  $^{18}\text{F}$  (b). Both profile plots show a nearly horizontal line indicating that the radioactive tracer is only transported through the branch, without accumulation. Diamonds represent starting origins of petioles. Triangles indicate wound tissue on the branch due to the removal of leaves.

Further confirmation of the  $\text{CO}_2$ -transport hypothesis was sought by performing an  $^{18}\text{F}$ -labelling experiment (Fig. 4.6b). Since  $^{18}\text{F}$ -radionuclides are not assimilated and solely transported (thus representing sap flow) a profile plot similar to the one obtained from the aluminium wrapped branch was observed. Green diamonds again indicate the positioning of petioles on the branch whereas red triangles indicate wound tissue on the branch due to the removal of leaves (with petiole). At these positions, water is able to evaporate. Fluorine is however not volatile and cumulated, resulting in peaks in the profile plots.

#### 4.4.2 $^{13}\text{C}$ -sugar analysis

The branch experiments with  $^{13}\text{C}$ -labelling revealed that illuminated branch parts (Li) had a significant higher ( $P < 0.05$ ) concentration of  $[2x\ ^{13}\text{C}]$ -fructose and glucose in the bark compared to darkened parts (Da) (Fig. 4.7 and Table 4.1). Detection of  $^{13}\text{C}$ - and  $[2x\ ^{13}\text{C}]$ -sugars in also Da branch sections can be explained by  $^{13}\text{C}$ -carbon that is naturally occurring in the environment. The concentration of all  $^{13}\text{C}$ -containing sugars (fructose, glucose and sucrose) in both bark and xylem and the concentration of all  $[2x\ ^{13}\text{C}]$ -sugars

(fructose, glucose and sucrose) in xylem had a tendency ( $P > 0.05$ ) to be higher in the Li parts compared to darkened parts. However, tendency ( $P > 0.05$ ) towards a lower concentration of  $[2x^{13}C]$ -sucrose was found in Li branch segments within bark tissue compared to the corresponding Da segment (Table 4.1 and Fig. 4.7b). The increase in all  $[^{13}C]$ - and  $[2x^{13}C]$ -containing sugars in Li branch segments with respect to Da ranged from moderate (11.0 %) to very high (307.7 %). Concentration of all sugars was generally higher in bark tissue compared to xylem tissue, except for glucose albeit neglectable. Furthermore, sucrose was observed to have the highest concentration of all  $^{13}C$ - and  $[2x^{13}C]$ -containing sugars and mainly affected the total sugar concentration. The increase in total sugar concentration in Li branch segments with respect to Da branch segments hereby, ranged from 7.9 % to 22.7 %.

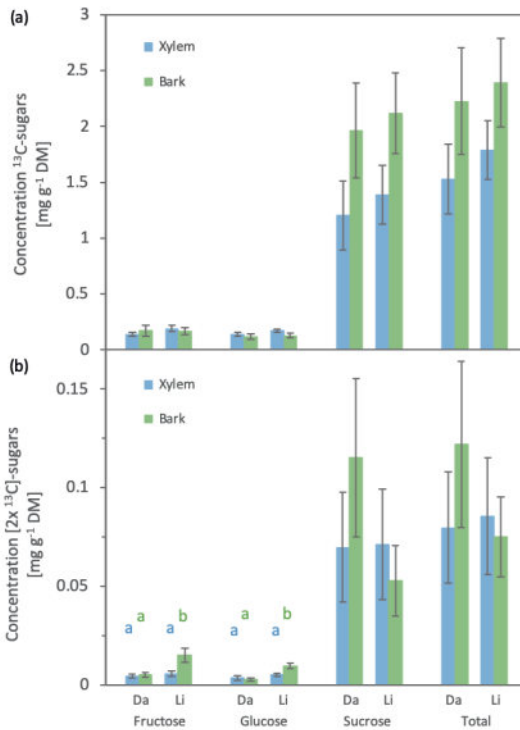


**Figure 4.7** Fructose, glucose, sucrose and total sugar concentration containing one (a) or two (b)  $^{13}C$ -atoms in both dark (Da) and illuminated (Li) parts of a poplar branch ( $N = 4$ ). Samples were further divided in bark and xylem. Error bars are standard errors. Statistical differences ( $P < 0.05$ ) between Li and Da branch parts are denoted with lower case letter.

**Table 4.1** Average enrichment ( $\pm$  SE) of xylem and bark samples of illuminated (Li) branch parts with respect to the dark (Da) branch parts for each of the analysed sugars fructose, glucose and sucrose containing one or two  $^{13}\text{C}$ -atoms. Statistically significant increase of Li branch parts with respect to Da branch parts are denoted with \* ( $P < 0.05$ ).

Sugar enrichment in branch part Li with respect to Da		Xylem	Bark
$^{13}\text{C}$	Fructose	$36.6 \pm 6.0 \%$	$17.7 \pm 2.9 \%$
	Glucose	$26.9 \pm 1.9 \%$	$15.4 \pm 7.7 \%$
	Sucrose	$23.7 \pm 6.7 \%$	$11.0 \pm 5.4 \%$
	Total	$22.7 \pm 11.3 \%$	$10.5 \pm 8.2 \%$
$2x \ ^{13}\text{C}$	Fructose	$34.8 \pm 23.6 \%$	$194.8 \pm 19.4 \%$ *
	Glucose	$89.1 \pm 26.8 \%$	$307.7 \pm 35.8 \%$ *
	Sucrose	$1.8 \pm 5.1 \%$	$-56.0 \pm 3.1 \%$
	Total	$7.9 \pm 16.0 \%$	$-33.9 \pm 4.7 \%$

## 4.5 Discussion

### 4.5.1 Assimilation of xylem-transported $\text{CO}_2$ in woody tissues

Knowledge on  $A_x$  by  $P_{wt}$  through exposure to PAR has merely been deduced from experiments that described enrichment of a  $^{13}\text{C}$ - or  $^{14}\text{C}$ -label within branches or leaves (e.g. McGuire *et al.* 2009; Bloemen *et al.* 2015; Stutz & Hanson 2019a), or a reduction in  $\text{CO}_2$  concentration when performing gas exchange measurements on PAR-illuminated twig or stem segments (e.g. Wittmann *et al.* 2001; Salomón *et al.* 2018). By means of LC-MS, we confirmed actual assimilation of internally-transported  $^{13}\text{CO}_2$  into sugars (i.e. fructose, glucose and sucrose) because Li samples contained higher sugar concentrations than Da ones (Table 4.1 and Fig. 4.7b), with the exception of  $[2x \ ^{13}\text{C}]$ -sucrose in the bark.

Specifically, a significant increase ( $P < 0.05$ ) in concentration of fructose and glucose containing two  $^{13}\text{C}$ -atoms was found when illuminating the branches. Given our short  $^{13}\text{C}$ -labelling period (1.75 h), fructose and glucose are known to be synthesized prior

to sucrose synthesis (Taiz & Zeiger 2010). Hence, accumulation of these sugars, rather than sucrose, is expected to contribute most to the activity peak detected in the  $^{11}\text{C}$ -profile plots of the illuminated branch parts (Figs. 4.3 and 4.4). It might be theorised that labelling for a longer period of time (e.g. 12h or longer) would result in also significant higher concentrations of  $[2x\ ^{13}\text{C}]$ -sucrose in Li samples compared to Da samples. A possible explanation why no significant increase was obtained for the fructose and glucose in the bark containing one  $^{13}\text{C}$ -atom upon illumination might be found in the high light sensitivity of  $P_{wt}$ . The rapid rise in detected  $^{11}\text{C}$ -activity in the profile plots upon illumination (Figs. 4.3a,b and 4.4c) indicates that the label was stripped from the sap in high amounts through  $P_{wt}$ . It is safe to assume that the same happened for the  $^{13}\text{C}$ -labelling, which increases the probability of  $[2x\ ^{13}\text{C}]$ -sugars synthesis over  $^{13}\text{C}$ -sugar synthesis. Additionally, increasing the currently limited sample size ( $N = 4$ ) would increase the power of the statistical test to detect a small effect which are now not significant.

With regard to the the higher concentration of  $[2x\ ^{13}\text{C}]$ -sucrose in the bark of Da samples compared to Li samples, two mechanisms are suggested that might take place simultaneously. First, there is a balance in the synthesis of sucrose and starch (which was however not measured). Both forms are synthesized from triose phosphate, but their synthesis is separated in space and time (Taiz & Zeiger 2010; Stitt & Zeeman 2012; Furze *et al.* 2018). Synthesis of sucrose occurs in the cytosol of the cell whereas starch, as well as fructose and glucose, are synthesized inside the chloroplasts. The balance between the biosynthetic pathway of sucrose and starch is determined by the relative concentration of metabolite effectors (e.g. orthophosphate and fructose-2,6-bisphosphate). Regarding the separation in time, surplus sugars produced in leaves during daytime are stored as starch granules in chloroplasts. During the night, these starch granules are then hydrolyzed to glucose to fuel growth and respiration or exported as sucrose to other plant organs via the phloem (Preiss 1984; Stitt & Zeeman 2012; Babst *et al.* 2013; Furze *et al.* 2018). It is likely that the same processes take place in woody tissues favouring synthesis of starch over sucrose in Li branch segments, whereas sucrose concentrations will increase for Da segments. Similar results were observed in a study where branches were exposed to a  $^{14}\text{C}$ -labelled solution. Moreover, higher  $^{14}\text{C}$ -starch enrichment (70% increase) compared to  $^{14}\text{C}$ -sugar enrichment (35% increase) was detected in petioles and major leaf veins upon illumination with PAR (Stringer & Kimmerer 1993). Reversely, a study investigating the sucrose and starch synthesis in function of light intensity observed

that up to seven times more carbon went into sucrose than into starch when light intensity was low (Sharkey *et al.* 1985). To confirm this, starch concentrations should have also been measured. However, this reasoning does not point out why higher concentrations of  $^{13}\text{C}$ -sucrose were found in Li samples compared to Da samples in the bark. Hence, a second mechanism might be taking place related to the difference in  $^{13}\text{C}$ - and  $[2x\ ^{13}\text{C}]$ -sucrose synthesis by sucrose synthase. Enzymatic conversion in plants is described to discriminate between  $^{13}\text{C}$  and  $^{12}\text{C}$  carbon isotopes as the overall abundance of  $^{13}\text{C}$  relative to  $^{12}\text{C}$  in plant tissues is commonly less than in atmospheric  $\text{CO}_2$  (O'Leary 1981; Farquhar 1989). Variation in the  $^{13}\text{C}/^{12}\text{C}$  ratio is the consequence of kinetic isotope effects, which are expressed during the formation and destruction of bonds involving a carbon atom. An example is the difference between the kinetic constants for the reaction of  $^{12}\text{CO}_2$  and  $^{13}\text{CO}_2$  with ribulose biphosphate carboxylase-oxygenase (RuBisCo) in which the process discriminates against the heavier isotope (Farquhar 1989). With regard to our results, a discrimination against  $^{13}\text{C}$ -glucose and/or  $^{13}\text{C}$ -fructose might have been taken place for sucrose synthase favouring  $^{13}\text{C}$ -sucrose synthesis over  $[2x\ ^{13}\text{C}]$ -sucrose synthesis. Note that the discrimination effect is probably less pronounced with regard to glucose and sucrose synthesis since both  $^{13}\text{C}$ - and  $[2x\ ^{13}\text{C}]$ -versions of these sugars are higher in Li samples compared to Da samples.

A total sugar concentration (sum of all  $^{12}\text{C}$ -,  $^{13}\text{C}$ - and  $[2x\ ^{13}\text{C}]$ -sugars) of  $39.4 \pm 6.8$   $\text{mg g}^{-1}$  DM ( $\pm$  SE) was observed and lies within the range of reported concentrations in deciduous trees (11–60  $\text{mg g}^{-1}$  DM; Reichenbacker *et al.* 1996; Sala *et al.* 2012). Compared to sucrose, lower concentration of fructose and glucose were detected in both xylem and bark tissues, which is in correspondence with literature (Landhäusser & Loeffers 2003; Traversari *et al.* 2018).

#### 4.5.2 $^{11}\text{C}$ -autoradiography to visualise assimilation of xylem-transported $\text{CO}_2$

So far, the assimilation of xylem-transported  $\text{CO}_2$  by  $P_{wt}$  in plants has been mainly studied using  $^{13}\text{C}$ - and  $^{14}\text{C}$ -based experiments (Stringer & Kimmerer 1993; Hibberd & Quick 2002; Bloemen *et al.* 2013c, b) or via  $\text{CO}_2$  gas exchange (Salomón *et al.* 2018; Stutz & Hanson 2019a; Wang *et al.* 2019). Both  $^{13}\text{C}$ - and  $^{14}\text{C}$ -labelling experiments as well as gas exchange measurements yield integrated responses from an entire organ (e.g. leaf, stem segment), making spatial resolution in both experiment-types rather coarse (typically in the order



of several cm in  $^{13}\text{C}$ - and  $^{14}\text{C}$ -experiments up to dm for gas exchange measurements). These methods are, hence, less suitable to study dynamics of xylem-transported carbon at high spatial resolution compared to imaging-based experiments. This has hampered our knowledge build-up about the behaviour of xylem-transported carbon with respect to  $P_{wt}$  across small distances (i.e. submillimetre resolution) within woody tissues. To address this, positron autoradiography was used in this study because it is a very sensitive technique obtaining images at high spatial resolution (24 pixels  $\text{mm}^{-1} \sim 50 \mu\text{m}$ ; in this study). Compared to other  $^{11}\text{C}$ -based studies like PET ( $\sim 1$  pixel  $\text{mm}^{-1}$ ; Hubeau et al. 2018) or direct positron images (3 pixels  $\text{mm}^{-1}$ ; Dirks et al. 2012), its resolution is superior. Positron autoradiography is especially suitable for revealing dynamics of short-time processes ( $\sim 1.5$  h) like  $P_{wt}$ . This is confirmed by the high detection sensitivity of the technique (e.g. minimum in the profile plot due to a petiole preventing close contact between phosphor plate and branch; Fig. 4.3c). Because of its high sensitivity and high spatial resolution, positron autoradiography has increasingly been employed for analysis of radioactive samples in e.g. molecular biology, pharmacology and receptor binding (Sihver et al. 1999; Maguire et al. 2012; Zanzonico 2012) and was proven to be successfully applied in plant sciences (Chapter 3, Babst *et al.* 2013, Bloemen *et al.* 2015).

Autoradiographic images (Fig. 4.2c,d and Fig. 4.4b) revealed that petioles and leaves contained  $^{11}\text{C}$ -tracer, with proximal positioned petioles and leaves having a higher activity than distal ones. Higher activities (indicated by a black colour) were detected in petioles and veins compared to parenchyma, which is in line with the findings of Chapter 3 as well as earlier studies (Stringer & Kimmerer 1993; McGuire et al. 2009; Bloemen et al. 2015; Hubeau et al. 2019b). Results indicate that branch respired  $\text{CO}_2$  dissolved in the xylem sap can be transported over several centimetres to be assimilated in leaves (Chapter 3 -Hubeau *et al.* 2019b). This was confirmed by treating leaf halves with grease (leaf 1), aluminium foil (leaf 2), or a combination thereof (leaf 3) (Fig. 4.2b). Almost no signal was detected in the aluminium covered leaf zones because no light could reach the tissues (Fig. 4.2d). Application of grease inhibited gas exchange with the atmosphere and thus convective movement of  $^{11}\text{CO}_2$  with the transpiration stream which, in turn, prevented the label to reach these leaf zones. However, secondary veins of the greased half of leaf 1 showed activity which could be attributed to assimilation of some locally respired  $\text{CO}_2$  in cells near the secondary veins, which generated a transient influx of water

to restore cell turgor, drawing water from petiole to leaf veins (Nikinmaa et al. 2013; Stroock et al. 2014; Hubeau et al. 2019b).

### 4.5.3 Effect of light on $P_{wt}$ dynamics in *P. tremula*

Autoradiography enabled successfully assessment of the light sensitivity of  $P_{wt}$  in *P. tremula* branches at high spatial resolution (Figs. 4.2, 4.4). The black colour (arbitrary choice) was associated with higher tracer uptake and thus higher woody tissue photosynthetic activity, and was observed in all proximal branch segments that were illuminated. The recorded signal reached a maximum, being  $\sim 3.8$  times higher than the activity recorded in the dark and decreased quickly thereafter (i.e. at a rate of 16% per cm). These results suggest that in the 1-year-old poplar branches a large part of the xylem-transported  $\text{CO}_2$  (originating from local respiration) is assimilated by  $P_{wt}$  (when exposed to PAR) within a short range from the point where it was dissolved in the xylem. McGuire et al. (2009) found comparable results when exposing detached branches to an aqueous  $^{13}\text{CO}_2$ -label with higher  $^{13}\text{C}$ -enrichment in branch sections in close proximity to the  $^{13}\text{C}$ -source. The observed reduction in enrichment with distance from the source was attributed to a reduction in concentration of dissolved  $^{13}\text{CO}_2$ -label in the sap as it ascended in the branch, due to assimilation and outgassing. Our findings confirm that  $A_x$  is responsible for reduced label-enrichment with branch length, regardless the fact that our study did not measure outgassing of  $^{14}\text{C}$ -label. Furthermore, our results complement the understanding acquired from experiments on leaves (Dirks et al. 2012; Bloemen et al. 2015; Hubeau et al. 2019b; Stutz & Hanson 2019a) and provide new insights on the  $A_x$  in woody tissues by  $P_{wt}$  on a small temporal and spatial scale.

Differences in recorded activity with application of grease, aluminium foil or the combination showed that irradiance is an important limiting factor for  $P_{wt}$ . Grease reduced the intensity of the highest activity signal by about one fourth compared to non-treated branches, which we attributed to light scattering on the grease, resulting in lower light intensity and reduced  $A_x$  by  $P_{wt}$ . Aluminium foil resulted in a distinct drop in activity (Fig. 4.4), because no PAR could reach the woody tissues. These results are consistent with  $^{11}\text{C}$ -experiments performed on leaves as described in Chapter 3 (Hubeau et al. 2019b). We theorized that recorded activity in dark conditions (i.e. in the labelling compartment or when covered with aluminium foil) was solely attributed to  $\text{CO}_2$ -

transport in the xylem. This was confirmed by wrapping an entire branch with aluminium foil, in which  $P_{wt}$  was prevented by full light exclusion (profile plot Fig. 4.6a). The only peak in activity was linked to the uncomplete wrapping of the branch due to the presence of a petiole (green diamond). The recorded 'baseline' hence represents  $\text{CO}_2$ -transport and is essentially attributed to sap flow. When a branch was allowed to transpire an  $^{18}\text{F}$ -enriched solution, the same nearly horizontal signal was observed, because  $^{18}\text{F}$ -ions are solely transported within the xylem conduits, which mimics water transport.

## 4.6 Conclusion

$^{11}\text{C}$ -positron autoradiography in combination with the applied labelling method in this study successfully enabled visualisation of  $P_{wt}$  in 1-year-old *P. tremula* branches and leaves. However, this method is less suitable for thicker tissue types like stems or mature branches, because  $^{11}\text{C}$ -positrons travel an average distance of  $\sim 1$  mm in condensed matter upon annihilation (conversion to gamma rays) so that they can no longer be detected by the autoradiographic phosphor plate. An alternative technique to study larger samples would be PET (e.g. Hubeau & Steppe 2015).

Furthermore, our results complement previous research performed on leaves and provided new insights on xylem-transported  $\text{CO}_2$  in woody tissues on a small temporal and spatial scale. Upon illumination with PAR, conversion of xylem-transported  $\text{CO}_2$  to sugars via  $P_{wt}$  was unequivocally demonstrated by means of LC-MS, rather than  $\text{CO}_2$  accumulation or retention within tissues. The  $^{11}\text{C}$ -results highlight the importance of studying the production of local sugars via  $P_{wt}$  at small spatial scales. More specific,  $P_{wt}$  seems to strip a large part of the  $\text{CO}_2$  molecules from the xylem sap within a short range from where they are released to assimilate them into carbohydrates. Consequently, respired  $\text{CO}_2$ , that is dissolved in the sap, is recycled providing a local buffer of energy. Given the fast assimilation of  $\text{CO}_2$  and the continuous supply of respiratory  $\text{CO}_2$ ,  $P_{wt}$  may have a far greater impact than assumed. However, further research on this topic in larger trees, different species with larger sample sizes would be necessary to assess the contribution of  $P_{wt}$  to the carbon budget of species under different environmental conditions like e.g. drought.



# 5

## STUDYING *IN VIVO* DYNAMICS OF XYLEM- TRANSPORTED $^{11}\text{CO}_2$ USING PET



## 5.1 Abstract

Respired CO<sub>2</sub> in woody tissues can build up in the xylem and dissolve in the sap solution to be transported through the plant. From the sap, a fraction of the CO<sub>2</sub> can either radially diffuse to the atmosphere or be assimilated in chloroplasts present in woody tissues. These processes occur simultaneously in stems and branches making it difficult to study their specific dynamics. Therefore, an <sup>11</sup>C-enriched aqueous solution was administered to young branches of *Populus tremula* L., which were subsequently imaged by PET. This approach allows *in vivo* visualisation of the internal movement of CO<sub>2</sub> inside branches at high spatial and temporal resolution, and enabled direct measurement of the transport speed of xylem-transported CO<sub>2</sub> ( $v_{CO_2}$ ). Through compartmental modelling of the dynamic data obtained from the PET images we (i) quantified  $v_{CO_2}$  and (ii) proposed a new method to assess the fate of xylem-transported <sup>11</sup>CO<sub>2</sub> within the branches. Specifically, it was found that a fraction of 0.49 of CO<sub>2</sub> present in xylem sap was transported upwards per minute. A fraction of 0.38 min<sup>-1</sup> of the xylem-transported CO<sub>2</sub> radially diffused from the sap to the surrounding parenchyma and apoplastic spaces (CO<sub>2,PA</sub>) to be assimilated ( $A_X$ ) by woody tissue photosynthesis. Another 0.12 min<sup>-1</sup> of the xylem-transported CO<sub>2</sub> diffused to the atmosphere via efflux ( $E_A$ ). The remaining CO<sub>2</sub> (i.e. 0.01 min<sup>-1</sup>) was stored ( $\Delta S$ ) as CO<sub>2,PA</sub> and can be regarded as build-up within the parenchyma and apoplastic spaces, that is to be assimilated or directed to the atmosphere. Here, we demonstrate the outstanding potential of <sup>11</sup>CO<sub>2</sub>-based plant-PET in combination with compartmental modelling to advance our understanding of internal CO<sub>2</sub> movement and the respiratory physiology within woody tissues.

## 5.2 Introduction

As indicated in previous Chapters, cell respiration releases  $\text{CO}_2$  which builds up and dissolves in the sap solution reaching a substantially higher concentration than that in the atmosphere. Xylem  $\text{CO}_2$  concentration ( $[\text{CO}_2]$ ) in the gaseous phase is hereby in equilibrium with  $\text{CO}_2$  species ( $\text{CO}_2(\text{aq})$ ,  $\text{HCO}_3^-$  and  $\text{CO}_3^{2-}$ ) dissolved in the sap solution (sap  $[\text{CO}_2^*]$ ) (Hari *et al.* 1991; Levy *et al.* 1999; McGuire & Teskey 2004). Hereby,  $\text{CO}_2$  is transported upward with the transpiration stream ( $F_T$ ) throughout the plant (Stringer & Kimmerer 1993) while another part can diffuse to surrounding xylem and phloem parenchyma and apoplastic spaces ( $\text{CO}_{2,PA}$  in Fig. 5.1). From there it has two main pathways: it can either radially diffuse into the atmosphere via stem  $\text{CO}_2$  efflux ( $E_A$ ) which is facilitated by the  $[\text{CO}_2]$  gradient across the xylem–atmosphere (Teskey *et al.* 2008) or be assimilated ( $A_X$ ) in chloroplasts present in the bark, xylem rays, and pith tissues (van Cleve *et al.* 1993; Berveiller *et al.* 2007; Pfanz 2008; Rentzou & Psaras 2008; Bloemen *et al.* 2016b). This latter process will be referred to as woody tissue photosynthesis ( $P_{wt}$ ). The remaining fraction of  $\text{CO}_2$  is stored ( $\Delta S$ ) and can be regarded as build-up of  $\text{CO}_{2,PA}$  that is to be assimilated or directed to the atmosphere. A schematic representation of these  $\text{CO}_2$  fluxes in woody plants is given in Fig. 5.1.

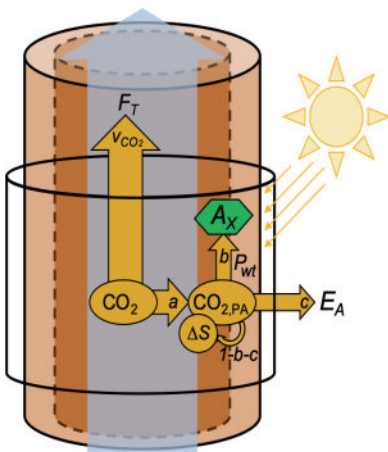


**Fig. 5.1** Schematic illustrating the fate of respired  $\text{CO}_2$  in woody tissues. Internal transport of xylem-transported  $\text{CO}_2$  ( $F_T$ ) can diffuse to the surrounding xylem and phloem parenchyma and apoplastic spaces ( $\text{CO}_{2,PA}$ ) from where it can either radially diffuse into the atmosphere via stem  $\text{CO}_2$  efflux ( $E_A$ ) or be assimilated ( $A_X$ ) by chloroplasts present in the bark, and xylem rays via woody tissue photosynthesis ( $P_{wt}$ ). The remaining part is stored ( $\Delta S$ ) as  $\text{CO}_{2,PA}$ . Xylem and outer tissues (cambium, phloem and bark) are represented in dark and light brown, respectively. The cylinder enclosing the stem segment represents one ROI of the model described in Fig. 5.5. Arrows indicate model parameters with  $v_{\text{CO}_2}$  the transport speed of  $\text{CO}_2$  ( $\text{mm min}^{-1}$ ) while  $a$ ,  $b$  and  $c$  represent  $\text{CO}_2$  exchange fractions ( $\text{min}^{-1}$ ).



Our understanding of xylem-transported CO<sub>2</sub> in relation to plant respiration is less advanced than our knowledge of water transport or photosynthesis (Amthor 2000; Atkin & Macherel 2009; Thornley 2011), although progress has been made. Specifically, the classic assumption of  $E_A$  being a measure of local stem respiration ( $R_S$ ) has been refuted as it has been demonstrated that part of the respired CO<sub>2</sub> dissolves in the sap solution to be transported upward through the xylem tissue (Hari *et al.* 1991; Levy *et al.* 1999; Teskey *et al.* 2008, 2017; Hölttä & Kolari 2009; Angert *et al.* 2012). However, questions about the transport of xylem-transported CO<sub>2</sub> through the xylem ( $F_T$ ) still remain, as it confounds interpretation of CO<sub>2</sub> efflux measurements from soil (Aubrey & Teskey 2009) and leaves (Stutz & Hanson 2019a), and it supports the mechanism of internal CO<sub>2</sub> recycling by  $P_{wt}$  (Bloemen *et al.* 2013a). It is expected that assimilation of xylem-transported CO<sub>2</sub> ( $A_X$ ) via  $P_{wt}$  is important for plant functioning, especially for young plant structures as well as under drought stress conditions (Cernusak & Marshall 2000; Bloemen *et al.* 2013a; Cernusak & Cheesman 2015; Steppe *et al.* 2015; Vandegehuchte *et al.* 2015). However, methodological constraints to study internal CO<sub>2</sub> transport ( $F_T$ ) in woody tissues at small spatial scale hinder accurate estimates of its dynamic fate (Teskey *et al.* 2008). Quantification of  $F_T$  is not straightforward. Two methods are described (McGuire & Teskey 2004; Angert *et al.* 2012; Salomón *et al.* 2018, 2019a). First, a mass balance approach has been proposed (on a volume basis;  $\mu\text{mol CO}_2 \text{ m}^{-3} \text{ s}^{-1}$ ) to account for  $F_T$  in  $R_S$  estimates:

$$R_S = F_T + E_A + \Delta S \quad (5.1)$$

$$= \frac{F_{H_2O}}{V} \times \Delta[\text{CO}_2^*] + \frac{F_{air}}{V} \times \Delta[\text{CO}_2] + \frac{L}{T} \times \Delta[\text{CO}_2^*]_T \quad (5.2)$$

where  $\Delta S$  is the storage CO<sub>2</sub> flux which excludes  $A_X$  through  $P_{wt}$  (McGuire & Teskey 2004). Hereby, gas exchange measurements are performed on a stem segment enclosed in a cuvette and requires measurements of sap flow  $F_{H_2O}$  ( $\text{L s}^{-1}$ ), sapwood volume  $V$  within the enclosed stem segment ( $\text{m}^3$ ), sap  $[\text{CO}_2^*]$  at top and bottom of the segment ( $\Delta[\text{CO}_2^*]$ ), air flow rate  $F_{air}$  through the cuvette,  $[\text{CO}_2]$  of the air entering and exiting the cuvette ( $\Delta[\text{CO}_2]$ ), length  $L$  of the stem segment and  $[\text{CO}_2^*]$  at start and end over a time period  $T$  ( $\Delta[\text{CO}_2^*]_T$ ). The second approach consists of simultaneous measurements of CO<sub>2</sub> and O<sub>2</sub> exchanges at the stem surface (Angert *et al.* 2012). The ratio of CO<sub>2</sub> efflux to the atmosphere and O<sub>2</sub> influx into the stem (defined as the apparent respiratory quotient - ARQ) is used as an

indication of  $F_T$ . Specifically, when assuming carbohydrates as the respiratory substrate and in absence of  $F_T$ ,  $\text{CO}_2$  production and  $\text{O}_2$  consumption will be equal, and ARQ close to one is expected. If respired  $\text{CO}_2$  is transported through the xylem, ARQ will deviate from unity. In both approaches, the internal  $\text{CO}_2$  fluxes (or a part of them) are either calculated from measurements (Eq. (5.2)) or indirectly estimated via a proxy (ARQ) using gas exchange measurements that integrate fluxes across a tree segment (e.g. Teskey & McGuire 2007; Salomón *et al.* 2018, 2019b; Hilman *et al.* 2019; Wang *et al.* 2019). Results capture net fluxes of internally transported  $\text{CO}_2$  while specific dynamics are described with a low spatial resolution.

We propose a novel approach to quantify the  $\text{CO}_2$  fluxes (i.e.,  $F_T/\text{CO}_{2,X}$ ,  $E_A/\text{CO}_{2,X}$  and  $\Delta S/\text{CO}_{2,X}$ ) as well as  $A_X/\text{CO}_{2,X}$  that originate from  $\text{CO}_2$  that is dissolved in xylem sap ( $\text{CO}_{2,X}$ ) based on radioactive  $^{11}\text{CO}_2$  labelling coupled with PET. To this end, an aqueous solution of  $^{11}\text{CO}_2$  was administered to the cut-end of branches of European aspen (*Populus tremula* L.). PET allowed *in vivo* visualisation of the dynamics of internally transported carbon with a high temporal resolution (every 2.5 min), resulting in 3D images with a high spatial resolution (c. 1 mm). Image analysis resulted in direct estimates of  $v_{\text{CO}_2}$ . By means of compartmental modelling,  $v_{\text{CO}_2}$  estimation was refined, while also the relative contribution of  $\text{CO}_{2,X}$  to the described carbon fluxes was determined. Revealing the dynamics of  $\text{CO}_2$  at high spatial and temporal resolution is essential to, for instance, better predict how plants cope with changing climate regimes. Furthermore, we believe that labelling of trees with radioactive isotopes is one of the most promising techniques to study plants *in vivo*.

## 5.3 Materials and methods

### 5.3.1 Plant material

For this study, 40-cm cuttings of *Populus tremula* L. ( $N = 3$ ) were planted on March 23, 2016 in 30-L pots containing commercial potting mixture (Peltracom, Gent, Belgium). They were grown in a greenhouse for two months at the Faculty of Bioscience Engineering, Ghent University, Belgium (51.053693°N, 3.706487°E) and eventually had a height ranging between 90 and 120 cm. The trees were subsequently transported to the small animal imaging facility of Ghent University (INFINITY lab) 24 h before measurement (Pickard *et al.* 1993) where they were placed outside during the experiments. The cuttings

were watered every day. The one-year-old study branches (N = 3, one branch per tree) had an average ( $\pm$ SE) length and diameter at their cut end of  $21.17 \pm 3.63$  cm and  $1.61 \pm 0.10$  mm, respectively.

### **5.3.2 Production and formulation of <sup>11</sup>CO<sub>2</sub>**

The radioactive <sup>11</sup>CO<sub>2</sub> was produced using a cyclotron (18 MeV protons, IBA, Belgium) of Ghent University Hospital where a proton (i.e. H<sup>+</sup>) was accelerated to a high velocity to bombard a N<sub>2</sub>/H<sub>2</sub> (5%) target. The (p,  $\alpha$ ) nuclear reaction resulted in the formation of <sup>11</sup>CH<sub>4</sub> which was subsequently oxidized via cobalt oxide to yield <sup>11</sup>CO<sub>2</sub> as described by Landais & Finn (1989). Subsequently, <sup>11</sup>CO<sub>2</sub> gas was bubbled through a 40 mM citric acid buffer at a set pH of *c.* 5.8, resembling the pH of xylem sap in young *P. tremula* branches (pH *c.* 6.4, which is in the reported range of 4.5 – 7.4 for woody species) (Teskey *et al.* 2008). The resulting <sup>11</sup>C-labelled solution was supplied to the cut end of the excised branches (one at a time). Once the solution is taken up by the branch, equilibrium reactions will shift according to the pH of the xylem sap (Butler 1991).

### **5.3.3 Experimental set-up and <sup>11</sup>C-labelling**

Dynamics in internally transported CO<sub>2</sub> in the poplar branches was imaged following exposure to the <sup>11</sup>C-labelled solution. Radioactive labelling of the branches (one branch per day) was performed in an airtight chamber (same as described in Chapter 4) consisting of two compartments, a polypropylene labelling compartment (6 mL in volume) in which the cut end of the branch was exposed to the <sup>11</sup>C-label and a cylindrical plexiglass measurement compartment (135 mm inner diameter and 200 mm length) containing leaves and light source (ten red and blue LED lights, GreenPower LED strings 0842 LF Red and WPO 83 LF Blue, Philips, The Netherlands) providing about 250  $\mu\text{mol photons m}^{-2} \text{s}^{-1}$  PAR to the leaves and branch (Fig. 5.2). After cutting the branch under water, its position within the chamber was fixed by applying polysiloxane material (Terostat-IX, Henkel AG & Company, KGaA, Düsseldorf, Germany) around the branch at the intersection of both compartments to separate them. Extra grease (Vacuum grease, Dow Corning, Auburn, MI, USA) was added around the branch segment coming out of the polysiloxane material which ensured airtightness between both labelling and measurement compartments to avoid assimilation of evaporated <sup>11</sup>CO<sub>2</sub> from the solution (<sup>11</sup>CO<sub>2</sub> (aq)  $\rightarrow$  <sup>11</sup>CO<sub>2</sub> (g)) by leaf photosynthesis. To avoid leaf wilting the labelling

compartment was filled with five mL of non-labelled buffer solution prior to the arrival of the label. A 5-mL volume was sufficient given the averaged transpiration rate ( $\pm$  SE) of  $0.40 \pm 0.01$  mL h<sup>-1</sup>. Regarding <sup>11</sup>C-labelling, same syringe set-up to provide <sup>11</sup>C-tracer was applied as described in Chapter 4. Five mL of <sup>11</sup>CO<sub>2</sub>-enriched solution was supplied to the branch with an activity at labelling of 125.8, 340.4 and 358.9 MBq, respectively, for each of the experiments. The branches were labelled for one hour.

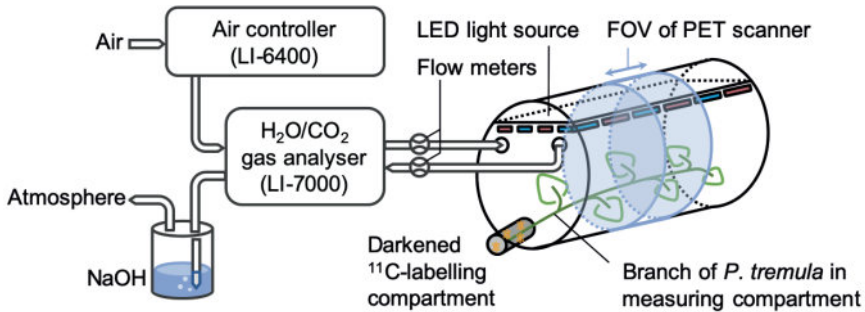


**Fig. 5.2** Schematic of the experimental set-up displaying a *P. tremula* branch inside an airtight chamber. A small and dark cylindrical labelling compartment with an aqueous solution containing the radioactive isotopes (indicated in orange) and the cut end of the branch is hermetically sealed from the measurement compartment containing the illuminated part of the branch. The measurement compartment was positioned in the circular bore of the PET scanner and only a part of it was surrounded by the detector ring (i.e. the FOV of the PET scanner). The incoming [CO<sub>2</sub>] is maintained at 400 ppm by a LI-6400 system while the water content and [CO<sub>2</sub>] entering and leaving the measurement compartment is analysed by a LI-7000 system, to calculate the transpiration and photosynthetic rate, respectively. For safety measures, the leaving air is stripped from all radioactivity by bubbling it through a basic NaOH solution.

The microclimate inside the measuring compartment is characterised by an average ( $\pm$  SE) relative humidity (RH), air temperature and vapor pressure deficit of  $62.8 \pm 2.3$  %,  $32.2 \pm 1.3$  °C and  $1.80 \pm 0.13$  kPa, respectively. During the experiment air containing 400 ppm CO<sub>2</sub> was continuously supplied using a portable photosynthesis system (model LI-6400, Li-Cor Inc., Lincoln, NE, USA). The H<sub>2</sub>O and CO<sub>2</sub> content of the air coming in and out of the measuring compartment was analysed with a gas analyser (model LI-7000, Li-Cor Inc., Lincoln, NE, USA). To prevent radioactivity from coming into the atmosphere, the outflowing air was directed to a 1 M sodium hydroxide solution. Transpiration rate and photosynthetic rate averaged ( $\pm$  SE) over the labelling periods, were  $0.69 \pm 0.14$  mmol H<sub>2</sub>O m<sup>-2</sup> s<sup>-1</sup> and  $1.18 \pm 0.38$   $\mu$ mol CO<sub>2</sub> m<sup>-2</sup> s<sup>-1</sup>, respectively. The obtained photosynthetic

rate is low for poplar leaves which could be explained by the low photosynthetically active radiation (PAR) intensity that was provided at leaf and branch level (250  $\mu\text{mol photons m}^{-2} \text{ s}^{-1}$ ). Common photosynthetic rates of *Populus tremula* are within the range of 10-15  $\mu\text{mol CO}_2 \text{ m}^{-2} \text{ s}^{-1}$  but are obtained at 1000-1500  $\mu\text{mol photons m}^{-2} \text{ s}^{-1}$  PAR. However, the results obtained in this study are equally valid since PAR at crown level of trees is around 300  $\mu\text{mol m}^{-2} \text{ s}^{-1}$  for a 12 h period (0700–1900 h) (Saveyn *et al.* 2010). Additionally, the low flow rate (0.4 L  $\text{min}^{-1}$ ) was not able to remove transpired water properly resulting in a high RH (60% vs. 40% in the room) likely hampered normal photosynthesis.

#### 5.3.4 PET scanner, image reconstruction and analysis

In this study, a LabPET8 scanner (TriFoil Imaging, Chatsworth, CA, USA – same as described in Chapter 3) was used which was located at the INFINITY imaging lab of Ghent University, Ghent, Belgium. When positioning the measurement compartment in the PET scanner, only a section was surrounded by the detector ring (15 cm inner diameter and a depth of 7.5 cm), which results in a relatively small field of view (FOV) for plant imaging. Twice a year, the detectors are normalized, and the scanner is calibrated. For radiation safety purposes, the labelling compartment was shielded using lead sheets. The PET scanner registered activity for one hour after exposing the cut end of the study branch to the aqueous solution containing dissolved <sup>11</sup>CO<sub>2</sub>. After scanning, the acquired signals detected by the PET scanner were reconstructed by the LabPET reconstruction software (Version 1.12.1, TriFoil Imaging, Chatsworth, CA, USA) using the maximum likelihood expectation maximization (MLEM) reconstruction algorithm to obtain an image showing <sup>11</sup>C-distribution within the FOV. Both a static 3D (i.e. x,y,z) and dynamic 4D (i.e. x,y,z,t) reconstruction were performed per experiment using a 3D- or 2D-MLEM algorithm, respectively. The static 3D-MLEM reconstructed image has a higher signal to noise (SNR) ratio compared to the 2D-MLEM reconstructed image and was used during image analysis for drawing regions of interest (ROIs - see further). On the contrary, 2D-MLEM reconstruction resulted in a quantitative image (voxels in MBq) which could not be obtained using the 3D-MLEM algorithm of the LabPET software. 2D-MLEM reconstruction of the data allowed mutual comparison of experiments and was therefore applied to retrieve dynamic 4D <sup>11</sup>C-images. For both MLEM reconstruction algorithms 50 iterations were used whereas the dynamic data was reconstructed into timeframes of 2.5 min. Correction for radioactive decay is performed during reconstruction so that a decay-corrected 3D

and 4D image were obtained consisting of one (static) and 24 (dynamic) timeframe(s) with 63 slices of  $200 \times 200$  voxels. Each voxel had a bit depth of 16 bits and a size of  $0.50 \times 0.50 \times 1.18$  mm. These images were imported in the open-source software tool AMIDE (Loening & Gambhir 2003) for image visualisation and analyses. On the static image (Fig. 5.3 – upper left corner), a 3D median filter with a kernel size of 3 was applied to reduce noise and highlight plant structures. On these images the branch was identified, and cylinder-shaped region of interests (ROIs) were drawn. Up to six consecutive ROIs (input ROI, ROI 1-5, Fig. 5.3 – upper left corner) were drawn along the direction of xylem flow with each ROI having a length and diameter of 4 and 5 mm, respectively. Subsequently the dynamically reconstructed image was imported into the same file and the cumulative amount of  $^{11}\text{C}$ -tracer in each ROI was calculated per 2.5 min timeframe (in MBq). Since the reconstructed images are corrected for decay, so are the resulting time-tracer curves (TTCs). The TTCs (Fig. 5.4) were exported to be used as input for the compartmental model. An example of a dynamically reconstructed image is provided in Fig. 5.3 with 10 min temporal resolution.

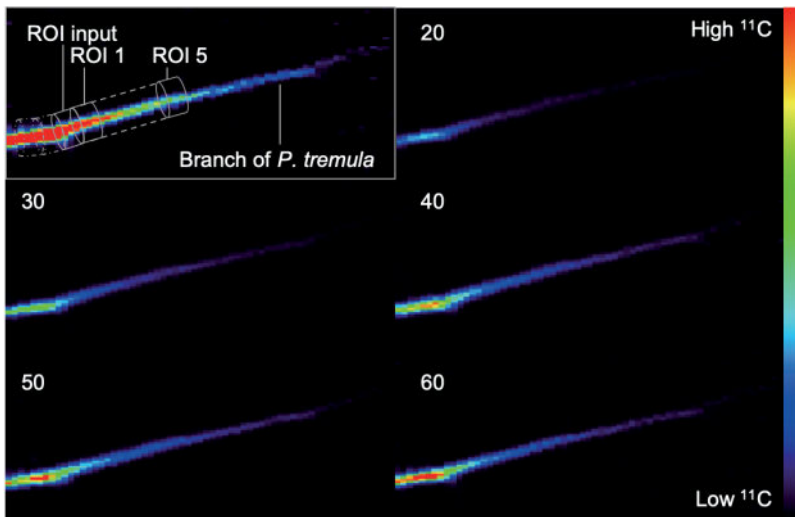


**Fig. 5.3** Example of a static (upper left corner) and dynamic PET images with a temporal resolution of 10 min (timestamp in min shown in the upper left corner of each dynamic PET image) of a *P. tremula* branch. An aqueous  $^{11}\text{CO}_2$ -solution was administered to the cut end of the branch (not shown) and its internal transport was visualised by dynamic PET images. The static PET image has highest SNR and is used for image analysis, i.e. drawing ROIs. These ROIs were applied on the dynamic PET images to obtain tracer concentrations per ROI over time, i.e. TTCs. Dash dotted ROIs were not used for image analysis since a petiole originated at that part of the branch. Colour bar indicates tracer content.

The two dash dotted ROIs in the utmost proximal part of the branch (upper left corner of Fig. 5.3) were not used because a petiole was present on the branch segment enclosed in these ROIs. Due to the spatial resolution of the PET scanner (*c.* 1 mm) the petiole and branch could not be resolved on the reconstructed image and the <sup>11</sup>C-tracer detected in both branch and petiole was therefore added in these dotted ROIs. This caused an incorrectly higher tracer concentration (i.e. TTCs – data not shown) with respect to the distally located ROIs. These TTCs were therefore omitted for modelling because they would inevitably prompt wrong results upon parameter calibration. Hence, branch segments were selected without ramifications.

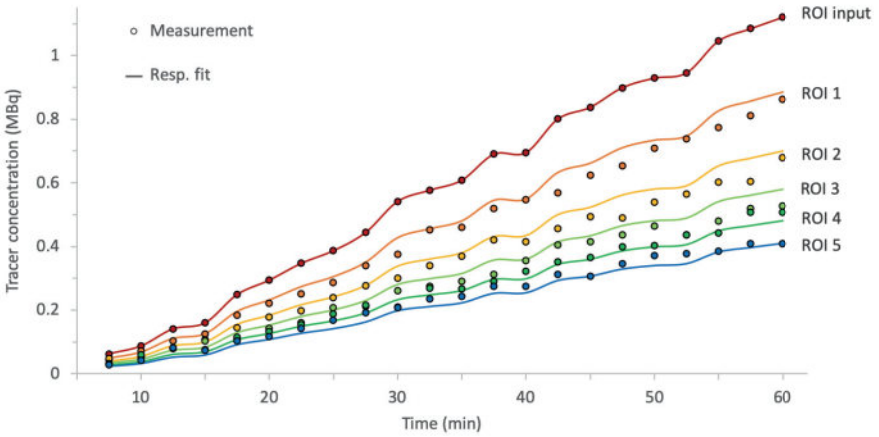


**Fig. 5.4** By extracting the tracer concentrations of six consecutive ROIs (ROI input, ROI 1–5) enclosing a branch segment of *P. tremula* on the dynamic PET images in Fig. 5.3, time-tracer curves (TTCs) are obtained (circles). The temporal resolution is here 2.5 min and time is expressed in minutes after pulse-labelling aqueous <sup>11</sup>CO<sub>2</sub> to the cut end of the branch. Simulation of the model defined in Fig. 5.5 using the calibrated parameters (i.e. describing the best model fit to the measured TTCs) resulted in the simulated TTCs (lines). Input ROI measurements were used as input for the compartmental model. Tracer concentrations are expressed in MBq.

A first image estimate  $v_{CO_2}^*$  of the CO<sub>2</sub> transport speed through xylem was derived from the distance of an ROI from the cut end of the branch and the time at which the tracer was first detected in that ROI. However, given a temporal resolution of 2.5 min of the dynamic PET images, CO<sub>2</sub> transport speed could not be accurately determined. Hence, this parameter was seen as an initial value and included in the model calibration to be further

refined. Student t-test was performed to denote statistical differences between the image-estimated and model-estimated CO<sub>2</sub> transport speed on a 5 % significance level ( $P < 0.05$ ).

### 5.3.5 Compartmental modelling to compute characteristics of xylem-transported CO<sub>2</sub>

The goal of fitting a compartmental model to dynamic tracer data through calibration was to derive specific parameters of xylem-transported carbon that have a physiological meaning and cannot be easily obtained from direct measurements. Due to the spatial resolution of the used PET scanner ( $\sim 1$  mm) physiological processes like the carbon fluxes between xylem and phloem tissues are integrated into the measured TTCs (circles in Fig. 5.4) and therefore compartmental modelling is used to disentangle them. A compartmental model based on Bühler *et al.* (2011) and Hubeau *et al.* (2018) was implemented in the plant modelling software PhytoSim (Phyto-IT, Gent, Belgium) and fed with the TTCs (Fig. 5.4) derived from ROIs from the image analysis. Therefore, each ROI was divided into three compartments (Fig. 5.5), which correspond to the compartments defined in Fig. 5.1.

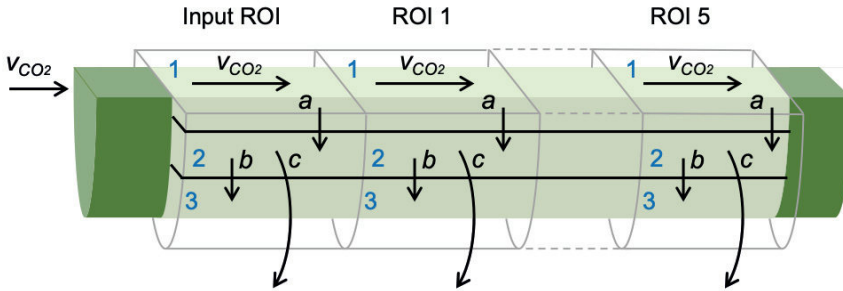


**Fig. 5.5** Schematic of the compartmental model used to simulate evolution of tracer amounts in the six consecutive ROIs (ROI input, ROI 1-5) along the branch segment. Tracer that enters an ROI is defined by bulk xylem CO<sub>2</sub> flow  $v_{CO_2}$  (mm min<sup>-1</sup>) and exchange parameters  $a$ ,  $b$  and  $c$  (min<sup>-1</sup>). Parameter  $v_{CO_2}$  describes the xylem CO<sub>2</sub> transport speed in compartment 1. Tracer will move from the xylem to compartment 2 (i.e. surrounding parenchyma and apoplastic spaces) through  $a$ , and can enter a storage compartment 3, via  $b$  where it is assimilated by  $P_{wt}$ , or can exit to the atmosphere (outside the ROI) through  $c$ . Parameters are assumed equal in each ROI, and data for the input ROI data is directly derived from measured activity.

The tracer concentration ( $T_C$  in MBq) of each compartment is described by mass balance Eqs. (5.3-5.5), where superscript denotes compartment number and subscript ROI



number. Compartment 1 embodies xylem conduits and is characterized by the speed of the xylem-transported CO<sub>2</sub>  $v_{CO_2}$  (mm min<sup>-1</sup>) and the exchange constant  $a$  (min<sup>-1</sup>), which represents the ratio of CO<sub>2</sub> that moves from xylem conduits into compartment 2 per minute, representing the surrounding xylem and phloem parenchyma and apoplastic spaces (CO<sub>2,PA</sub> in Fig. 5.1). From compartment 2, the <sup>11</sup>C-tracer is either directed towards chloroplast-containing cells where it is assimilated by  $P_{wt}$  (Fig. 5.1) and potentially relocated in storage cells (compartment 3 in Fig. 5.5) via  $b$ , or radially diffused to the atmosphere via  $c$ . Chloroplast-containing tissues have been found in xylem ray cells (Rentzou & Psaras 2008) and pith tissue (van Cleve *et al.* 1993) but mainly in phloem and bark tissues (Pfanz & Aschan 2001; Saveyn *et al.* 2010). Exchange parameters  $b$  and  $c$  (both in min<sup>-1</sup>) thus represent the net tracer fraction exchanged from compartment 2, which is assimilated via  $P_{wt}$  or alternatively diffuses to the atmosphere via efflux, respectively, and can be used to estimate  $A_X$  and  $E_A$  of Eq. (5.1). Note that some CO<sub>2</sub> can remain in compartment 2 to be temporarily stored as CO<sub>2</sub> ( $\Delta S$  of Eq. (5.1)). The parameter search range for  $v_{CO_2}$  was narrowed around the image-derived initial value  $v_{CO_2}^*$  (which differed for each of the experiments). The search range for the other parameters was not adjusted.

$$\frac{dT_{C_i}^1}{dt} = \frac{v_{CO_2}}{l} \cdot T_{C_{i-1}}^1 - \frac{v_{CO_2}}{l} \cdot T_{C_i}^1 - a \cdot T_{C_i}^1 \quad (5.3)$$

$$\frac{dT_{C_i}^2}{dt} = a \cdot T_{C_i}^1 - b \cdot T_{C_i}^2 - c \cdot T_{C_i}^2 \quad (5.4)$$

$$\frac{dT_{C_i}^3}{dt} = b \cdot T_{C_i}^2 \quad (5.5)$$

Constant  $l$  is the length of the ROI (i.e. 4 mm). Parameters  $a$ ,  $b$  and  $c$  represent fractions of CO<sub>2</sub> flowing across compartments and thus range from 0 to 1. Note that these parameters are the net result of <sup>11</sup>C-tracer flowing forth (e.g.  $a_{12}$ ) and back (e.g.  $a_{21}$ ) to each compartment because separate parameters (in- and outflow) were not identifiable. This approach is comparable with the fixed ratio (e.g.  $a_{21} = h \times a_{12}$ ) implemented by Bühler *et al.* (2011). For the first timeframe, we assumed that all measured tracer was present in compartment 1. This assumption was tested, and it was found that the parameter outcome was insensitive to whether initial activity was allocated to compartment 1 only or distributed over all three compartments. Branch material was checked to ensure that

the dimensions did not change with ROI since all model parameters were assumed to be constant for each ROI as well as over the entire scan time (i.e. 1 h). Note that this model allows CO<sub>2</sub> gas-liquid interconversion (Hari *et al.* 1991; Levy *et al.* 1999) but does not differentiate between phases. Calibrated parameters should be taken with caution given that other carbon fluxes not accounted for by the model might bias parameter calibration. However, this model suited our measurements best while other model formulations with a different number of compartments and/or parameters can be developed in a similar way (Bühler *et al.* 2014).

In the model, the input ROI (with all other ROIs being located downstream from it) does not receive tracer from upstream ROIs. In reality, however, tracer will enter this ROI via xylem sap upstream, so the tracer concentration in its first compartment was directly calculated from the total amount of tracer measured in the input ROI ( $T_{C_{total}}$ ) for each time step according to Eq. (5.6). The change in tracer concentrations for the other two compartments was calculated according to Eqs. (5.4-5.5) with  $i = input$ .

$$T_{C_{input}}^1 = T_{C_{total}} - T_{C_{input}}^2 - T_{C_{input}}^3 \quad (5.6)$$

Model sensitivity and identifiability were assessed according to De Pauw *et al.* (2008), and the four model parameters ( $v_{CO_2}$ ,  $a$ ,  $b$ ,  $c$ ) were identifiable, with each parameter having a high sensitivity in the model output. Simulations were performed by using an adaptive step size fourth order Runge-Kutta solver (accuracy  $10^{-5}$ , maximum step size 1 min) (Runge 1895; Kutta 1901; De Pauw *et al.* 2008). Parameter calibration was done by applying a shuffled complex evolution (Duan *et al.* 1993), with 9 complexes (i.e. two times number of model parameters + 1, which was found to result in a better overall calibration performance as described by Duan *et al.* (1994)) and an accuracy of  $10^{-5}$ , for 5000 evaluations. Calibration was completed when the difference between simulated and measured TTCs was minimized.

### 5.3.6 Data processing and terminology

To assess the correlation between  $v_{CO_2}$  and the transpiration rate or the computed exchange parameters ( $a$ ,  $b$  and  $c$ ), a linear regression model was fitted in RStudio (R Core Team (2018), RStudio: Integrated Development Environment for R. RStudio, Inc., Boston, MA, USA, version 1.1.453) using the *lm* function, in which  $v_{CO_2}$  was treated as independent

variable whereas transpiration rate,  $a$ ,  $b$  and  $c$  were treated as dependent variables. To indicate that each of the variables had different variance, weighted least squares were added in the fitting process. Normality of the variables was tested and found by Shapiro-Wilk test (on a 5% significance level), justifying the application of a linear model. The linear regression model resulted in an intercept ( $\beta_0$ ), slope ( $\beta_1$ ) and coefficient of determination ( $R^2$ ) and P-values indicating whether or not the slope and/or intercept were significant at a 5 % significance level ( $P < 0.05$ ).

When  $\beta_1$  was significant, a significant increase or decrease was mentioned (Table 5.1). When  $\beta_1$  was not significant but  $\beta_0$  was, and  $R^2$  was equal or higher than 0.5 a tendency towards a positive or negative correlation was indicated. When both  $\beta_1$  and  $\beta_0$  were not significant, and  $R^2$  was equal to or higher than 0.5, a tendency towards a positive or negative correlation was indicated. When both  $\beta_1$  and  $\beta_0$  were not significant, and  $R^2$  was lower than 0.5 a no effect was reported.

**Table 5.1** Determination table of terminology based on slope ( $\beta_1$ ), intercept ( $\beta_0$ ) and coefficient of determination ( $R^2$ ) of a linear regression.

$\beta_1$	$\beta_0$	$R^2$		Terminology
Significant ( $p < 0.05$ )	-	-	$\Rightarrow$	Significant
Not significant	Significant ( $p < 0.05$ )	$\geq 0.5$	$\Rightarrow$	Tendency to
Not significant	Not significant	$\geq 0.5$	$\Rightarrow$	Tendency to
Not significant	Not significant	$\leq 0.5$	$\Rightarrow$	No effect

### 5.3.7 Assessing the fate of xylem-transported CO<sub>2</sub> using PET and compartmental modelling

Exchange parameters  $a$ ,  $b$  and  $c$  describe the fate of the xylem-transported CO<sub>2</sub> with respect to net radial diffusion, assimilation by  $P_{wt}$  and efflux to the atmosphere, respectively. These parameters can be used to estimate the relative contribution of xylem-dissolved CO<sub>2</sub> ( $CO_{2,x}$ ) to each of the carbon fluxes ( $F_T^{\%}/CO_{2,x}$ ,  $\Delta S^{\%}/CO_{2,x}$  and  $E_A^{\%}/CO_{2,x}$ ) in accordance with the model described by McGuire & Teskey (2004) Eq. (5.1). Additionally, our method allows to identify the relative amount of CO<sub>2,x</sub> that is assimilated by  $P_{wt}$  (i.e.  $A_X^{\%}/CO_{2,x}$ ). Specifically, parameter  $a$  indicates CO<sub>2</sub> exchange from the xylem conduits to

the surrounding parenchyma and apoplastic spaces (i.e.  $CO_{2,PA}$ ). Hence, fraction  $(1 - a)$  of the  $^{11}CO_2$ -tracer was transported upwards on a minute basis representing  $F_T^{\%}/CO_{2,X}$ .  $CO_2$  that is present in the parenchyma and apoplastic spaces ( $CO_{2,PA}$ ) can be assimilated through  $P_{wt}$  (via  $b$  to compartment 3 of the model in Fig. 5.5) or be released to the atmosphere via efflux (via  $c$ ). Hence, to estimate the corresponding xylem-transported  $CO_2$  fractions multiplication of exchange parameters  $b$  and  $c$  with  $a$  was performed, as these products can be related to the relative  $CO_2$  fluxes  $A_X^{\%}/CO_{2,X}$  (i.e. assimilation flux) and  $E_A^{\%}$  (i.e. efflux to the atmosphere), respectively. The remaining  $CO_{2,PA}$   $(1 - b - c)$  can be multiplied with  $a$  to retrieve the storage flux  $\Delta S^{\%}$ . The relative contribution of the each of the carbon fluxes is given in Eq. (5.7).

$$1 = (1 - a) + (a \times b) + (a \times c) + (a \times (1 - b - c)) \quad (5.7)$$

$$F_T^{\%}/CO_{2,X} \quad A_X^{\%}/CO_{2,X} \quad E_A^{\%}/CO_{2,X} \quad \Delta S^{\%}/CO_{2,X}$$

## 5.4 Results

### 5.4.1 PET images

Tracer transport from the proximal (left) part of the branch to the distal part is shown in Fig. 5.3. Highest tracer concentration was observed in the proximal part. The normalized sum of tracer concentrations ( $\pm$  SE) over the scanning period of one hour per ROI (averaged over all three experiments) is given in Fig. 5.6. Tracer concentration per ROI was normalized with the input ROI concentration.

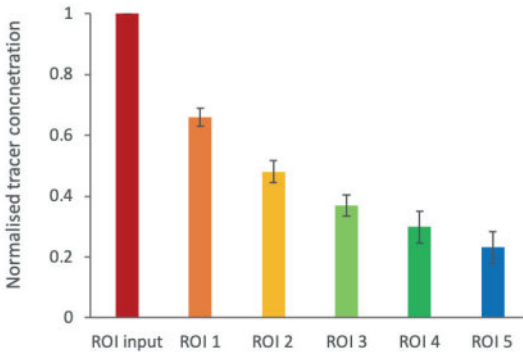


**Fig. 5.6** Normalized sum of tracer concentration per ROI over the scanning period of one hour, averaged over all three  $^{11}C$ -experiments performed on branches of *P. tremula* (error bars indicate SE). Tracer concentrations were normalized per experiment with respect to the concentration measured in the input ROI.

#### 5.4.2 Modelling xylem-transported carbon dynamics

Time series of tracer concentration within each ROI (Fig. 5.4) showed that <sup>11</sup>C-tracer concentration increased with time. Each distally located ROI showed a lower concentration with respect to the adjacent proximal ROI, indicating local retention of tracer through  $P_{wt}$  and/or tracer efflux to the atmosphere. Measured TTCs were used for compartmental modelling and closely corresponded with the simulated TTCs (Fig. 5.4). In the study branches (N = 3), average ( $\pm$  SE) model-estimated speed of xylem-transported CO<sub>2</sub>  $v_{CO_2}$  (for the compartmental model in Fig. 5.5) was found to be  $5.00 \pm 1.29$  mm min<sup>-1</sup> and was not significantly different ( $P > 0.05$ ) from the average ( $\pm$  SE) image-estimated  $v_{CO_2}^*$  (based on the distance of an ROI from the cut end of the branch and the time at which the tracer was first detected in that ROI), which equalled  $5.55 \pm 2.15$  mm min<sup>-1</sup> (Fig. 5.7a). The exchange rate parameters  $a$  (i.e. tracer fraction from xylem conduits to the surrounding xylem and phloem parenchyma and apoplastic spaces),  $b$  (i.e. the fraction of CO<sub>2,PA</sub> that gets assimilated by  $P_{wt}$ ) and  $c$  (i.e. the tracer fraction that diffuses to the atmosphere via efflux) averaged ( $\pm$  SE) over the experimental branches (N = 3)  $0.51 \pm 0.06$ ,  $0.71 \pm 0.07$  and  $0.25 \pm 0.06$  min<sup>-1</sup> (Fig. 5.7b). Note that actual exchange fractions might be higher than the obtained model-estimates, because our parameters represent net exchange between tissues/compartments.

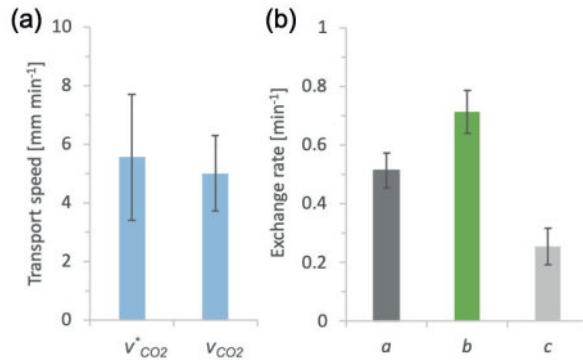


**Fig. 5.7** Average estimated parameter values for the compartmental model as defined by Fig. 5.5, with (a) average PET image-estimation of the transport speed  $v_{CO_2}^*$  by means of the distance of an ROI from the cut end of the branch and the time at which the tracer was first detected in that ROI, and average model-estimation  $v_{CO_2}$ . No significant difference ( $P > 0.05$ ) was found between both transport speeds (b) Average model parameter estimates  $a$ ,  $b$  and  $c$ . Average values were calculated over the experiments performed on branches of *P. tremula* while error bars indicate SE.

The average ( $\pm$  SE) relative contribution of xylem-transported  $\text{CO}_2$  to the fluxes  $F_T^{\%}/\text{CO}_{2,X}$ ,  $A_X^{\%}/\text{CO}_{2,X}$ ,  $E_A^{\%}/\text{CO}_{2,X}$  and  $\Delta S^{\%}/\text{CO}_{2,X}$  equalled  $0.49 \pm 0.06$ ,  $0.38 \pm 0.08$ ,  $0.12 \pm 0.01$  and  $0.01 \pm 0.01 \text{ min}^{-1}$ , respectively, and their sum equals one. Note that the fraction of  $\text{CO}_2$  that remains inside the parenchyma and apoplastic spaces ( $\Delta S^{\%}/\text{CO}_{2,X}$ ) is neglectable. Tendency towards a positive correlation was found between the transpiration rate and the transport speed of xylem-transported  $\text{CO}_2$ , i.e.  $v_{\text{CO}_2}$  (Fig. 5.8a). Tendency towards a positive correlation was obtained for the exchange parameters  $a$ ,  $b$  and  $v_{\text{CO}_2}$  (Fig. 5.8b). A tendency to an inverse correlation was found between parameter  $c$  and  $v_{\text{CO}_2}$  (Fig. 5.8b).

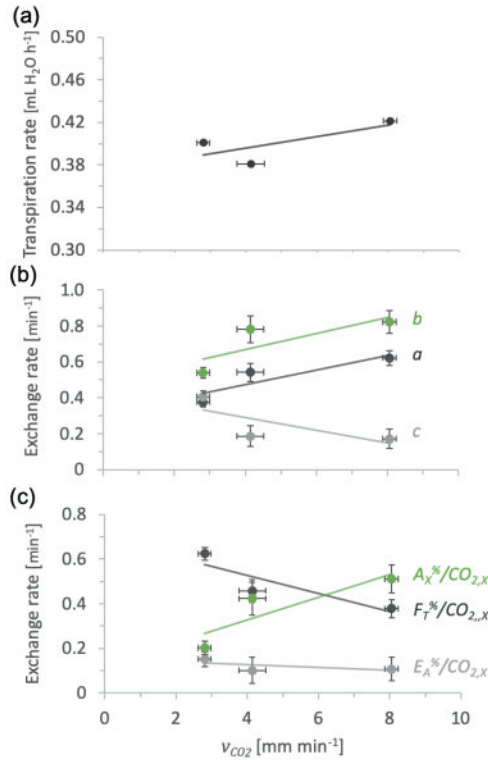


**Fig. 5.8** Estimated parameter values for the compartmental model defined in Fig. 5.5 (a,b) and the calculated relative carbon fluxes (c), in function of the simulated transport rate of  $\text{CO}_2$  within xylem ( $v_{\text{CO}_2}$ ). Specifically, (a) the relation between the transpiration rate and  $v_{\text{CO}_2}$  ( $R^2$  of 0.71), (b) the relation between the exchange parameters ( $a$ ,  $b$  and  $c$ ) and  $v_{\text{CO}_2}$  ( $R^2$  of 0.88, 0.79 and 0.71, respectively). Parameters  $a$ ,  $b$  and  $c$  represent the tracer fractions between compartments defined by Eq. (5.3-5.5). (c) The relation of the relative carbon fluxes  $F_T^{\%}/\text{CO}_{2,X}$ ,  $A_X^{\%}/\text{CO}_{2,X}$  and  $E_A^{\%}/\text{CO}_{2,X}$  (as calculated by Eq. (5.7)) and  $v_{\text{CO}_2}$  ( $R^2$  of 0.79, 0.75 and 0.39). Error bars indicate 95% confidence interval and are derived from the uncertainty analysis.

With regard to the relative carbon fluxes, tendency towards a positive correlation was found between  $A_X^{\%}/CO_{2,x}$  and  $v_{CO_2}$  whereas tendency to an inverse correlation was found for  $F_T^{\%}/CO_{2,x}$  as a function of  $v_{CO_2}$  (Fig. 5.8c). Since  $\Delta S^{\%}/CO_{2,x}$  was neglectable in all three branches, no linear model was tested and it was not included in Fig. 5.8c.

## 5.5 Discussion

### 5.5.1 Plant-PET to unravel dynamics in woody tissue photosynthesis

Preceding to compartmental modelling, pure image analysis demonstrated that highest <sup>11</sup>C-concentrations were found in the proximal branch parts (Figs. 5.4 and 5.6). Part of the <sup>11</sup>C-tracer hence accumulated during the scanning period, indicating assimilation of CO<sub>2</sub> by  $P_{wt}$ . Comparable results were obtained in detached sycamore branches that were allowed to take up <sup>13</sup>CO<sub>2</sub>-labelled solution (McGuire *et al.* 2009). Moreover, highest <sup>13</sup>C-enrichment was found in the lower branch sections due to their proximity to the <sup>13</sup>C-source. Regarding the transport speed of CO<sub>2</sub>, a first image-estimated  $v_{CO_2}^*$  was obtained by determining which specific branch segment was inside the FOV of the PET scanner. This is, to our understanding, the first method to directly determine the speed of xylem-transported CO<sub>2</sub> *in vivo*. Given the temporal resolution of 2.5 min of the dynamic PET images, this initial value was subsequently used to narrow the search range of model-estimated  $v_{CO_2}$  upon parameter calibration.

The compartmental model was able to simulate the behaviour of internally transported CO<sub>2</sub> in young branches, resulting in a close correspondence between measured and simulated time–tracer curves of <sup>11</sup>C-tracer (Fig. 5.4). No significant difference ( $P > 0.05$ ) was found between  $v_{CO_2}^*$  and  $v_{CO_2}$ , indicating the validity of the proposed measurement techniques, i.e. direct image- and model-estimation of CO<sub>2</sub> transport speed. Since CO<sub>2</sub> is transported through the xylem,  $v_{CO_2}$  is expected to be linked to the sap flow rate (McGuire & Teskey 2004; Bloemen *et al.* 2013c; Salomón *et al.* 2018). This rationale is also used in the mass balance approach (Eq. (5.2); McGuire & Teskey 2004) as sap flow is used to calculate the carbon flux through the xylem. This explains the tendency towards a positive correlation between the transpiration rate and  $v_{CO_2}$  (Fig. 5.8a).

Aside from the CO<sub>2</sub> transport speed  $v_{CO_2}$ , other dynamic characteristics of xylem-transported CO<sub>2</sub> within *P. tremula* branches were assessed using a combination of PET

scans and compartmental modelling. Model calibration successfully resulted in the exchange parameters  $a$ ,  $b$  and  $c$  describing the  $\text{CO}_2$  transport fractions with respect to net radial diffusion, assimilation  $A_X$  through  $P_{wt}$  and efflux to the atmosphere, respectively. Analogous to the mass balance approach described by McGuire & Teskey (2004), we propose dynamic  $^{11}\text{C}$ -PET combined with compartmental modelling yielding the exchange parameters as a new method to further disentangle the different carbon fluxes inside woody tissues. Our method results in the relative contribution of  $\text{CO}_{2,X}$  to each of the carbon fluxes of the mass balance ( $F_T^{\%}/\text{CO}_{2,X}$ ,  $\Delta S^{\%}/\text{CO}_{2,X}$  and  $E_A^{\%}/\text{CO}_{2,X}$ ) as well as  $A_X^{\%}/\text{CO}_{2,X}$  of which the sum equals one. When measuring  $[\text{CO}_2^*]$  ( $\mu\text{mol CO}_2 \text{ L}^{-1}$ ) inside branches and branch water content ( $\text{L m}^{-3}$ ), it is possible to quantify each of the relative carbon fractions in Eq. (5.7) to fluxes expressed in  $\mu\text{mol CO}_2 \text{ m}^{-3} \text{ min}^{-1}$ . However, note that the obtained relative carbon fluxes are not comparable with the carbon fluxes of the mass balance described by McGuire & Teskey (2004) since our study only focusses on the fate of xylem-transported  $\text{CO}_2$  ( $\text{CO}_{2,X}$ ). Hence, the sum of the relative fluxes does not represent respiration  $R_S$ . To make the comparison with the mass balance fluxes, it comes down to knowing which part of  $R_S$  will dissolve in the sap at small spatial scale. Comparison with studies which involved labelling the xylem sap is of course justified.

In young branches of *P. tremula*, it was found that slightly less than half ( $0.49 \text{ min}^{-1}$ ) of the  $^{11}\text{CO}_2$ -tracer was transported upwards on a minute basis representing the contribution of  $F_T^{\%}/\text{CO}_{2,X}$ . This is plausible as a study where 7-yr-old field-grown poplar trees were infused with  $^{13}\text{CO}_2$ -labeled solution into the base for two days described  $^{13}\text{C}$ -enrichment throughout the entire tree (stem, branch woody tissues and foliage) suggesting substantial tracer movement (Bloemen *et al.* 2013b). The same trend was observed for a similar study on 4-m tall northern white-cedar trees (Powers & Marshall 2011). Additionally, a study where detached 20-50 cm long branches (<1 cm in diameter) of a 7-year-old *P. deltoides* tree were labelled with aqueous  $^{13}\text{CO}_2$ -enriched solutions (having different label concentration) found that at least 29% of the assimilated  $^{13}\text{C}$ -label was fixed in the branches (with the remaining part in the leaves) (Bloemen *et al.* 2013a). These results suggest that most of the label was transported to the leaves to be assimilated. They can however not be used to predict  $F_T^{\%}/\text{CO}_{2,X}$  which is an advantage of  $^{11}\text{C}$ -based PET over  $^{13}\text{C}$ -based labelling.



The relative xylem-transported CO<sub>2</sub>-fraction contributing to the assimilation flux  $A_X^{\%}/CO_{2,X}$  (0.38) lies within the assimilation percentage (35 – 42 %) of young branches of poplar and sycamore that could take up a <sup>13</sup>CO<sub>2</sub>-labelled solution (McGuire *et al.* 2009; Bloemen *et al.* 2013c). However, it is rather low compared to the reported reassimilation percentage of woody species (40 – 123%) (Teskey *et al.* 2008; Ávila *et al.* 2014). Reassimilation higher than 100% are associated with net CO<sub>2</sub> uptake via lenticels in the stem periderm (Berveiller *et al.* 2007) but was not taken into account in this study. Furthermore, parameter *b* indicates that most of the available CO<sub>2,PA</sub> was assimilated instead of directed to the atmosphere (0.71 vs. 0.25 - Fig. 5.7b). This is in accordance to the high  $A_X$  efficiency of  $P_{wt}$  observed in young *P. tremula* branches and petioles which are characterised by thin and smooth bark having a high content of chloroplasts (Aschan *et al.* 2001; Ávila *et al.* 2014; De Roo *et al.* 2019). However, upon development of the periderm, a reduction in light transmittance can be expected, causing a reduction in  $A_X$  efficiency of  $P_{wt}$  (Ávila *et al.* 2014).

The relative fraction of xylem-transported CO<sub>2</sub> that was direct to the atmosphere via efflux  $E_A^{\%}$  had a limited contribution (0.12) and is related to the assimilation of internal CO<sub>2</sub> by  $P_{wt}$ . Specifically,  $A_X$  in the light has been estimated to reduce CO<sub>2</sub> efflux from branches by about 52% (McGuire *et al.* 2009). Hence, it is expected that CO<sub>2</sub> efflux would increase when the branches would not have been irradiated with PAR.

### 5.5.2 Dependency of internal CO<sub>2</sub> fluxes on transport speed

Since sap flow and thus the transport speed of CO<sub>2</sub> is found to substantially affect both the efficiency of  $P_{wt}$  and the efflux to the atmosphere (Teskey & McGuire 2002; McGuire *et al.* 2007; Teskey *et al.* 2008; Bloemen *et al.* 2013c; Ávila *et al.* 2014; Stutz & Hanson 2019a) the exchange parameter values of each experiment are described as function of  $v_{CO_2}$ . Exchange parameter *a* had a tendency to increase with increasing  $v_{CO_2}$  (Fig. 5.8b) which might be explained by the fact that more CO<sub>2</sub> is delivered to the tissue at a higher transport speed. The observed trend is similar to the inverse coupling between sap velocity and sap [CO<sub>2</sub>] detected in the stem of a *Liriodendron tulipifera* tree (Teskey & McGuire 2002). Xylem [CO<sub>2</sub>\*] (similar to  $1 - a$  in our study) in *L. tulipifera* trees was high during the night, when sap velocity was zero, and decreased during the morning as sap velocity increased. During brief periods of cloud cover during the day, sap velocity decreased and xylem [CO<sub>2</sub>\*] increased concurrently. Similarly, under controlled temperature conditions, xylem

[CO<sub>2</sub>\*] of *Platanus occidentalis* branches decreased rapidly as sap velocity increased and remained low at higher sap velocities (McGuire *et al.* 2007).

Since assimilation of xylem-transported CO<sub>2</sub> is dependent on the transpiration rate (Bloemen *et al.* 2013c; Mincke *et al.* 2018), which provides substrate for photosynthetic reactions, a tendency to a positive correlation was found between  $b$  and  $v_{CO_2}$  (Fig. 5.8b). The observed trend is in accordance to a study where the transpiration rate of detached poplar branches was altered at leaf level, while the branches were allowed to take up <sup>13</sup>CO<sub>2</sub> solution (Bloemen *et al.* 2013c). Subsequent <sup>13</sup>C-analysis of branch and leaf tissues revealed that woody tissues assimilated more label under higher transpiration, than when transpiration was low.

Since parameter  $c$  has a non-zero value, our results indicate that part of xylem-transported <sup>11</sup>CO<sub>2</sub> radially diffused to the atmosphere which illustrates the error incurred when  $R_S$  is estimated from  $E_A$  measurements (McGuire & Teskey 2004; Teskey *et al.* 2008; Trumbore *et al.* 2013). By means of isotopic labelling coupled with isotope ratio laser spectroscopy, Salomón *et al.* (2019) disentangled the contribution of locally respired CO<sub>2</sub> ( $L_{CO_2}$ ) and xylem-transported CO<sub>2</sub> ( $T_{CO_2}$ ) to  $E_A$  for *P. tremula*. When the contribution of both  $T_{CO_2}$  and  $L_{CO_2}$  to  $E_A$  is desired, the current experimental set-up requires measurements of  $E_A$  and internal sap [CO<sub>2</sub>\*]. Note that volatile organic compounds (VOCs) like isoprene and terpenes are created using the same substrate as sugars, i.e. trisose phosphate and could thus be produced from assimilated <sup>11</sup>CO<sub>2</sub> (Lichtenthaler & Zeidler 2002; Hillier & Lathe 2019). However, only 0.4 % of recently fixed carbon is used for isoprene production (Ferrieri *et al.* 2005). Additionally, as these are volatile compounds, they will be directed to the atmosphere and would contribute to model parameter  $c$  which was small compared to the other parameters. It is therefore safe to assume that the synthesis of VOCs will not have a tremendous effect on the proposed mass balance.

## 5.6 Conclusion

Tracing xylem-transported <sup>11</sup>CO<sub>2</sub> in young *P. tremula* branches using the medical imaging technique positron emission tomography enabled visualising its dynamics *in vivo* with high spatial and temporal resolution. We demonstrated the applicability of dynamic PET imaging in combination with compartmental modelling to quantify the transport speed of internal CO<sub>2</sub> ( $v_{CO_2}$ ) as well as to retrieve dynamics in xylem-transported CO<sub>2</sub> with regard to upward transport with the sap ( $F_T$ ), assimilation via  $P_{wt}$  ( $\Delta S$ ) and efflux to the

atmosphere ( $E_A$ ).  $P_{wt}$  may efficiently reduce respiratory CO<sub>2</sub> losses, at least in young twigs and branches, and thus in the outer parts of tree crowns. Hence, refixation of CO<sub>2</sub> appears to be of great importance for carbon budgets in e.g. environmentally controlled leafless states of deciduous trees (although surely different in young and mature trees). However, increasing the number of replications by including both smaller and bigger sized branches is needed to further confirm our results and could potentially result in a statistically significant regression of the model parameters in function of  $v_{CO_2}$ .

Nonetheless, our findings indicate the potential of plant-PET since physiological parameters are obtained regarding the fate of internally transported CO<sub>2</sub> that are otherwise challenging to be measured with the same spatial resolution. Therefore, we believe that *in vivo* imaging in combination with modelling, both at cell and organ scale, are necessary to advance our mechanistic understanding of plant physiology, including  $P_{wt}$ .



# 6

## CONCLUSIONS AND PERSPECTIVES



What happens with CO<sub>2</sub> once it is respired by mitochondrial activity? In view of the threat of increasing droughts, which is related to carbon starvation, this question might become of great importance for forests and other ecosystems in many regions on earth. However, our understanding of respired CO<sub>2</sub> and its dynamics is still far less advanced compared to our knowledge of e.g. water transport. This might be related to methodological constraints of the techniques that have been used so far to study xylem-transported CO<sub>2</sub> in relation to stem respiration, i.e. mainly <sup>13</sup>C- or <sup>14</sup>C-measurements or gas-exchange methods which both suffer from a limited spatial resolution. Therefore, this PhD thesis was centred around the investigation of the dynamic fate of internally transported CO<sub>2</sub> by application of medical imaging modalities. Specifically, the possibility of applying positron emission tomography (PET) and positron autoradiography were explored towards tracing <sup>11</sup>C-labelled CO<sub>2</sub> *in vivo* at high temporal and spatial resolution in leaves and branches of poplar trees (i.e. *Populus × canadensis* Moench “Robusta” and *Populus tremula* L.).

The introduction of this thesis was concluded by a list of four main questions, each of which will be discussed in the following section.

## **6.1 Can medical imaging techniques be used to study the dynamic fate of internal CO<sub>2</sub>**

Whereas application of medical visualisation methods is rather narrow in plant science, these techniques, with the focus on PET, are one of the most common and useful imaging modalities in both clinical and preclinical settings. Moreover, positron autoradiography is applied in several fields ranging from molecular biology, pharmacology, receptor binding and quantitative biopsy analysis (Sihver *et al.* 1999; Maguire *et al.* 2012; Zanzonico 2012) due to its high spatial resolution (~ 50 µm). Additionally, this technique is fairly straightforward as images are obtained by exposing the labelled tissue to a phosphor plate which is read out afterwards. Therefore, the potential application of this technique to visualise assimilation of xylem-transported CO<sub>2</sub> ( $A_x$ ) in leaves, petioles and branches was tested in this PhD thesis (**Chapters 3, 4**). By performing short <sup>11</sup>C-labelling experiments (~ 1.5 h) it was demonstrated that CO<sub>2</sub> was assimilated in these tissues when they were exposed to photosynthetically active radiation (PAR). Autoradiographic images

revealed that illumination of the branches resulted in a vast response in the sections closest to the label-source, indicating that CO<sub>2</sub> is stripped from the sap to be assimilated. Opposed to the direct application of autoradiography to visualise tissues in **Chapters 3, 4**, it has been used in a creative way to assess carbon partitioning to the major non-structural carbohydrates (NSC, i.e. fructose, glucose, sucrose and starch) recently fixed in leaves (Babst *et al.* 2013). Hereby leaves were labelled using gaseous <sup>11</sup>C<sub>2</sub>O<sub>2</sub> of which tissue extracts were analysed by high-performance thin-layer chromatography (HPTLC) to separate the soluble sugars. The TLC plates were subsequently exposed to an autoradiographic plate to determine the metabolic partitioning of assimilated <sup>11</sup>C to soluble sugars. It would have been beneficial if this method was performed in **Chapter 4** on tissues that were illuminated with PAR (Li) and or in the darkened labelling compartment (Da). Practically, extraction of these samples and HPTLC analysis could have been done perfectly after direct visualisation of the whole branch and the results would have validated the ones of the <sup>13</sup>C-based experiments. Furthermore, the additional benefit offered by elucidating carbon partitioning to NSC via <sup>11</sup>C-based analysis (HPTLC + autography) over <sup>13</sup>C-based LC-MS is that only the added <sup>11</sup>C-tracer is detected whereas <sup>13</sup>C is also naturally occurring.

Whereas positron autoradiography has proven its ability to study  $A_x$  in the studied leaves and young branches, it is less suitable for imaging thicker tissue types like stems or mature branches. Specifically, the phosphor plates detect <sup>11</sup>C-positrons which need to reach them by travelling through the tissue. However, the average distance of <sup>11</sup>C-positrons is only ~ 1 mm in condensed matter upon annihilation (conversion to gamma rays) so that they can no longer be detected by the autoradiographic phosphor plate. When larger tissues (with regard to volume) are being studied, it is advised to make use of PET as an alternative technique.

PET is used worldwide on a daily basis for detection and treatment monitoring of human diseases because of its high diagnostic efficacy and accuracy (Saha 2016). Additionally, it is used in preclinical studies on rodents and nonhuman primates for research on drug development linked to e.g. oncology, cardiology or neurology (Ametamey *et al.* 2008; Fleming *et al.* 2015; Kogan *et al.* 2018). In this PhD thesis, the potential application of PET was tested by dynamic visualisation of internal CO<sub>2</sub> in leaves and branches (**Chapter 2, 4**). In order to allow leaves and branches to transpire an enriched <sup>11</sup>C-solution, first a labelling system was developed (**Chapter 2**) to prevent



radioactive CO<sub>2</sub> from entering the atmosphere. Dynamic PET imaging combined with compartmental modelling successfully provided a new method to assess the percentual contribution of internal CO<sub>2</sub> (on a time basis) to the carbon fluxes describing its fate (i.e. upward transport with sap, radial diffusion to the atmosphere and assimilation via  $P_{wt}$ ). Each of these fluxes can be quantified (i.e.  $\mu\text{mol CO}_2 \text{ m}^{-3} \text{ min}^{-1}$ ) by measuring both the internal [CO<sub>2</sub>\*] ( $\mu\text{mol CO}_2 \text{ L}^{-1}$  - as described by McGuire & Teskey (2004)) and the branch water content ( $\text{L m}^{-3}$ ) hereby demonstrating the applicability to study the dynamics of internal CO<sub>2</sub> using PET.

Despite its applicability, the set-up described in **Chapter 4** could be further improved by measuring the radioactivity that ended up in the NaOH solution (i.e., neutralised <sup>11</sup>CO<sub>2</sub> in the air leaving the measurement compartment), the activity of the remaining <sup>11</sup>C-solution that was not taken up by the branch as well as the activity inside the branch. Hereby, a direct estimation of the efflux (activity in NaOH solution) and storage + transport (activity in branch) of CO<sub>2</sub> could be retrieved. This information can then be used to validate the results of the compartmental model.

## **6.2 What is the relevance of xylem-transported CO<sub>2</sub>?**

By performing experiments in which branches were exposed to a <sup>13</sup>C-labelled solution and subsequently analysed using liquid chromatography–mass spectrometry (**Chapter 4**), this PhD thesis evidenced unambiguously that internally transported CO<sub>2</sub> is stripped from the sap to be assimilated into sugars by  $P_{wt}$  under light exposure. By manipulating the incident PAR to branches (**Chapter 4**), positron autoradiography indicated that carbon was mainly transported through the xylem when these were not illuminated. This hypothesis was confirmed by performing <sup>18</sup>F-labelling experiments with <sup>18</sup>Fluorine being a proxy for water. By visualising both water and <sup>11</sup>CO<sub>2</sub> transport we demonstrated that only with illumination of branches, CO<sub>2</sub> is stripped from the xylem sap for  $P_{wt}$ . These insights coupled with the firm light-response of  $P_{wt}$ , suggest that respired CO<sub>2</sub> that dissolves in the sap in stem or branches containing no or limited amount of chlorophyll (Chl) could be transported upwards until the point it is stripped from the sap to be assimilated in Chl-containing stem and branch segments or possibly leaves, at least if it is not directed to the atmosphere via efflux along the pathway. In that respect, young branches will benefit from Chl-containing periderm and xylem parenchyma cells as they

might receive CO<sub>2</sub> from older branch tissues (containing less Chl) which can be assimilated.

PET measurements performed on 1-year-old branches (**Chapter 5**) revealed that a large part of the internal CO<sub>2</sub> (i.e. 38 %) is assimilated by  $P_{wt}$  to likely be stored, while only 12 % was outgassed to the atmosphere via efflux. The remaining part of 49 % was found to be transported upward with the sap. Since  $P_{wt}$  was taking place along entire Chl-containing branches, it might be suggested that a vast part of the transported CO<sub>2</sub> also ends-up being assimilated, suggesting that overall only a limited part of the internal CO<sub>2</sub> ends up in the atmosphere in young branches. This is in line with the indication that  $P_{wt}$  can reduce the loss of respired CO<sub>2</sub> from woody tissues to the atmosphere by 50 to > 100 %, suggesting that on a 24 h basis, 20–40 % recovery of respired carbon may be feasible, at least in canopy branches (Teskey *et al.* 2008). Continuing on this concept, it could be suggested that xylem-transported CO<sub>2</sub> molecules could undergo multiple cycles of assimilation and respiration before ending up in the atmosphere. According to the great sensitivity of  $P_{wt}$ , each ‘recycling’ process could possibly occur within a short distance from where CO<sub>2</sub> molecules are dissolved in the sap flow of young branches.

Besides  $A_X$  in woody tissues, it was found that the majority of xylem-transported CO<sub>2</sub> is assimilated in leaves of poplar (*Populus deltoides*) while efflux was small compared to respiration (Stutz & Hanson 2019a). However,  $A_X$  within poplar leaves comprises a small portion of total leaf photosynthesis which is estimated to be between 2 - 10% of total assimilates (Bloemen *et al.* 2013c; Stutz & Hanson 2019a). Nonetheless, combined with the results described in this PhD thesis it is not unlikely that  $A_X$  plays a major role in the growth and development of young Chl-containing branches and leaves. Under high irradiance and low internal inorganic carbon ( $[\text{CO}_2^*] = [\text{CO}_2] + [\text{HCO}_3^-] + [\text{CO}_3^{2-}]$ )  $A_X$  was found to be higher (Stutz & Hanson 2019a) indicating that  $A_X$  in leaves and branches will become even more important when CO<sub>2</sub> is limited, i.e. under drought.

In order to make a rough estimation of  $A_X$  via  $P_{wt}$  on branch level only [CO<sub>2</sub>] need to be known inside the branch. Although this measurement was not performed, it can be estimated from stem [CO<sub>2</sub>] of *Populus* species and is on average 10% (Teskey *et al.* 2008; Salomón *et al.* 2018). Using Henry’s law, it is possible to convert this CO<sub>2</sub> concentration in the gaseous phase to total dissolved [CO<sub>2</sub>\*] in the liquid phase (McGuire & Teskey 2002) which results in 6 mmol L<sup>-1</sup>. Eventual multiplication of this value with the averaged leaf

transpiration in this PhD thesis ( $1.5 \text{ mmol H}_2\text{O m}^{-2} \text{ s}^{-1}$ ) results in a total amount of  $0.16 \text{ } \mu\text{mol CO}_2 \text{ m}^{-2} \text{ s}^{-1}$  that is transported in young branches. The results obtained in this PhD thesis suggest that 38% of it is locally assimilated, which is small as this assumes that the other 50% that is transported ( $F_T$ ) is not assimilated. This corresponds to  $0.06 \text{ } \mu\text{mol CO}_2 \text{ m}^{-2} \text{ s}^{-1}$  which is about 0.5 % of outer crown leaf photosynthesis ( $\sim 1000 \text{ } \mu\text{mol PAR m}^{-2} \text{ s}^{-1}$ ) but 1 % for inner crown leaf photosynthesis ( $\sim 300 \text{ } \mu\text{mol PAR m}^{-2} \text{ s}^{-1}$ ). This value is likely to increase further when  $\text{CO}_2$  is limited (Stutz & Hanson 2019a). This is however a rough estimation and more data is needed on the relationship between stem and branch tip [ $\text{CO}_2^*$ ] as well as their diurnal and seasonal patterns before a solid prediction can be made of what the contribution is from one branch up to single tree.

Since the exchange of water and carbohydrates mainly occurs between roots and leaves (i.e., the main suppliers and consumers of water and carbohydrates, respectively), it is not surprising that xylem and phloem functioning are coupled in these organs (Hölttä *et al.* 2006; Taiz & Zeiger 2010; Sevanto *et al.* 2011; Pfautsch *et al.* 2015). However, as  $\text{CO}_2$  is shown to be transported with the xylem sap within (Chl-containing) branches (**Chapter 4**) and illumination of these branches results in assimilation of this  $\text{CO}_2$  through  $P_{wt}$  (**Chapter 4 and 5**),  $P_{wt}$  might be regarded as a coupling between xylem and phloem in branches, and in a similar way potentially also in Chl-containing stems. Carbohydrates produced from xylem-transported  $\text{CO}_2$  by  $P_{wt}$  represent an alternative and immediate source of non-structural carbohydrates and can be used for maintenance and growth processes or osmotic adjustment (Cernusak & Cheesman 2015). Furthermore, local synthesis of sugars along the chlorophyll-containing stems supports the leakage-retrieval adaptation to the generally accepted Münch theory (Münch 1930; Hölttä *et al.* 2009; Jensen *et al.* 2009; Knoblauch & Peters 2010). Down the phloem pathway, considerable amounts of carbohydrates are lost to lateral sinks. However, a part of these lost carbohydrates is subsequently reloaded into the phloem tissue, which is referred to as the leakage-retrieval mechanism. By means of  $P_{wt}$ , new carbohydrates can be produced, and provided across the entire Chl-containing stem when exposed to PAR. Hence, this can be seen as an infinite supply of carbohydrates enabling continuous local buffering of irregularities in the turgor potential and gradient in phloem tissue.

### 6.3 Why should we expand positron-based imaging in plant studies?

Aside its usefulness to study xylem-transported CO<sub>2</sub>, PET has already shown its applicability to investigate the transport of nutrients, phytohormones and photoassimilates (e.g. Minchin & Thorpe 2003; Kiser *et al.* 2008; Jahnke *et al.* 2009; Hanik *et al.* 2010; Hubeau *et al.* 2018). The short half-life of the applied radiotracers (e.g. 2 – 109 min for the most used radioisotopes in plant science) in combination with the non-invasive nature of PET enable the same plant to be scanned multiple times without destructive sampling. These features allow to determine plant responses to environmental changes in the same plant (Kiser *et al.* 2008). Furthermore, PET is especially suited to decipher phloem functioning. Since this tissue type is pressure-driven (De Schepper *et al.* 2013), it is easily disturbed through transport or displacement, complicating its investigation (Pickard & Minchin 1990; Turgeon & Wolf 2009). Radiotracers enable visualisation of the sugar flow without damaging or perturbing phloem transport (Jahnke *et al.* 2009; Kawachi *et al.* 2011; Yamazaki *et al.* 2015; Hubeau *et al.* 2018; Hidaka *et al.* 2019). Improving our understanding of the mechanisms that drive phloem transport will undoubtedly lead to new approaches for manipulating photoassimilate allocation patterns in crops and fruits.

Aside from the abovementioned examples, positron-based imaging has huge potential to be further expanded in plant science. Its restricted application in plant science may be related to the complexity of putting together methodological developments from multiple disciplines, such as radio-pharmacology, physics, mathematics and engineering, which may form an obstacle for some research groups. Hence, **Chapter 2** was composed to encourage researchers to study plants using PET. The approaches and methodology described in that particular chapter are applied in the other chapters to unravel the dynamic character of internal CO<sub>2</sub> and they are the result of trial and error while addressing technical difficulties. One of these technical difficulties encountered in this PhD thesis can be linked to working with gaseous <sup>11</sup>CO<sub>2</sub>. This holds especially for the PET study described in **Chapter 5**, where a limited number of repetitions (N = 3) were studied but actually more experiments were carried out. These could not be included in the study since the labelling and measuring compartment of the experimental set-up were not hermetically sealed. Dissolved <sup>11</sup>CO<sub>2</sub> from the labelling solution could therefore evaporate and make its way through the connection of both compartments. This connection coincided with the branch part that was being exposed to PAR i.e. most interesting part to

be imaged and used for modelling. Creating a hermetic sealing between both compartments using polysiloxane material (which was used in **Chapter 5**) was challenging but further research (not described in this PhD thesis) indicated that this was easier to achieve by another sealing method which involves the use of two cylindrical rubber pieces as described in **Chapter 2**.

#### **6.4 What are the challenges and future prospects for plant-PET**

Unlike human or laboratory animal imaging, where the object size is fairly fixed, the size of plants may range from several millimetres to meters, indicating that the scanner should have a large field of view (FOV) for imaging large plants while pursuing a high spatial resolution. However, most of the PET studies carried out on plants use either PET systems that were specifically developed for plant imaging (e.g. Kume *et al.* 1997; Uchida *et al.* 2004; Jahnke *et al.* 2009; Beer *et al.* 2010; Wu & Tai 2011; Weisenberger *et al.* 2012; Wang *et al.* 2014) or laboratory animal PET scanners (e.g. Alexoff *et al.* 2011; Hubeau *et al.* 2018), which are both characterised by a limited FOV (i.e. the PET scanner used to perform the experiments described in **Chapter 3** and **5** has a transverse and axial FOV of 15 and 7.5cm). Although these scanning systems benefit from a high spatial resolution (~1.5 mm and sometimes submillimetre) generally only one or two plant organs (stem, leaves, fruits, or roots) can be visualised (e.g. Jahnke *et al.* 2009; Hubeau *et al.* 2018; Hidaka *et al.* 2019). The PET scanner used in this PhD thesis was able to visualise dynamics of internal CO<sub>2</sub> in young branches but is not adapted to study the dynamics at stem or mature branch level given its small FOV. Yet, a more comprehensive view of whole-plant carbon allocation patterns can be gained from mature organs in large plants, where a quasi-active carbon sink for carbohydrate storage competes with different plant carbon sinks as growth or respiration (Sala *et al.* 2012; Hartmann & Trumbore 2016). These difficulties could be overcome by making use of clinical PET systems, which are developed for human imaging, as these systems have two main advantages. Firstly, these imaging devices allow visualisation of larger objects since they are characterised by a transverse and axial FOV up to 85 and 26 cm, respectively (Vandenberghe & Marsden 2015; Vandenberghe *et al.* 2016). Additionally, clinical PET scanners are equipped with a moving bed on which the plant can be placed, which enables visualisation of even larger plants than the volume of the FOV, by acquiring multiple bed positions that can be stitched

together into a larger volume. Secondly, clinical PET systems are nearly exclusively used in combination with structural imaging like computed tomography (CT) or magnetic resonance imaging (MRI). Consequently, the functional information provided by PET can be combined with structural data provided by CT or MRI, but only few plant studies have been reported making use of this multimodal imaging approach (e.g. Jahnke *et al.* 2009; Garbout *et al.* 2012). The structural information is incredibly useful when it comes down to imaging small structures like leaves and branches with smaller dimensions. Specifically, in Fig. 3 of **Chapter 4**, it seemed obvious to start drawing ROIs from the most proximal point of the branch because of the high measured tracer concentrations (dash dotted ROIs). However, in these ROIs a petiole originates from the branch and due to the limited resolution of the PET system (~ 1-2 mm) the tracer inside the petiole and branch could not be resolved resulting in higher TTCs for these ROIs (not shown). This would inevitably prompt incorrect parameter values upon calibration.

However, a drawback of clinical PET systems is the lower spatial resolution (~ 3 mm - Vandenberghe & Marsden 2015) compared to the laboratory animal PET scanners (España *et al.* 2014; Fine *et al.* 2014). Additionally, the FOV of clinical PET systems have a horizontal axis while in some cases where large plants are studied, it might be appropriate to have a vertical orientation of the PET scanner. Nevertheless, the possibility towards using a clinical PET system on large plants (70–90 cm in length) has been described (e.g. Karve *et al.* (2015)). In this study, photoassimilate transport dynamics were investigated in sorghum plants whereby the plant was imaged while laying horizontally. As this position would certainly affect plant function over the long-term, there was little or no effect of the horizontal positioning in the commercial PET scanner on transport speeds,  $^{14}\text{CO}_2$  leaf assimilation or photosynthetic  $\text{CO}_2$  exchange rates (measured with an IRGA) compared with vertical plants within the 3 h time frame of the experiment demonstrating the potential application of clinical PET systems to study plants, although for short-time processes. Despite the intensive occupancy of these clinical PET systems, we believe that studies making use of these functional imaging devices will make an important contribution to reveal complex *in vivo* interactions in plants, like the link between xylem and phloem tissue.

B

BIBLIOGRAPHY





- 
- Agtuca, B., Rieger, E., Hilger, K., Song, L., Robert, C.A.M., Erb, M., *et al.* (2014). Carbon-11 Reveals Opposing Roles of Auxin and Salicylic Acid in Regulating Leaf Physiology, Leaf Metabolism, and Resource Allocation Patterns that Impact Root Growth in *Zea mays*. *J. Plant Growth Regul.*, 33, 328–339.
- Alexoff, D.L., Dewey, S.L., Vaska, P., Krishnamoorthy, S., Ferrieri, R., Schueller, M., *et al.* (2011). PET imaging of thin objects: Measuring the effects of positron range and partial-volume averaging in the leaf of *Nicotiana tabacum*. *Nucl. Med. Biol.*, 38, 191–200.
- Ametamey, S.M., Honer, M. & Schubiger, P.A. (2008). Molecular imaging with PET. *Chem. Rev.*, 108, 1501–1516.
- Amthor, J.S. (2000). The McCree-de Wit-Penning de Vries-Thornley respiration paradigms: 30 Years later. *Ann. Bot.*, 86, 1–20.
- Angert, A., Muhr, J., Negron Juarez, R., Alegria Muñoz, W., Kraemer, G., Ramirez Santillan, J., *et al.* (2012). Internal respiration of Amazon tree stems greatly exceeds external CO<sub>2</sub> efflux. *Biogeosciences*, 9, 4979–4991.
- Aschan, G. & Pfanz, H. (2003). Non-foliar photosynthesis – a strategy of additional carbon acquisition. *Flora*, 198, 81–97.
- Aschan, G., Wittmann, C. & Pfanz, H. (2001). Age-dependent bark photosynthesis of aspen twigs. *Trees - Struct. Funct.*, 15, 431–437.
- Atkin, O.K. & Macherel, D. (2009). The crucial role of plant mitochondria in orchestrating drought tolerance. *Ann. Bot.*, 103, 581–597.
- Aubrey, D.P. & Teskey, R.O. (2009). Root-derived CO<sub>2</sub> efflux via xylem stream rivals soil CO<sub>2</sub> efflux. *New Phytol.*, 184, 35–40.
- Ávila, E., Herrera, A. & Tezara, W. (2014). Contribution of stem CO<sub>2</sub> fixation to whole-plant carbon balance in nonsucculent species. *Photosynthetica*, 52, 3–15.
- Babst, B.A., Karve, A.A. & Judt, T. (2013). Radio-metabolite analysis of carbon-11 biochemical partitioning to non-structural carbohydrates for integrated metabolism and transport studies. *Plant Cell Physiol.*, 54, 1016–1025.
- De Baerdemaeker, N.J.F., Salomón, R.L., De Roo, L. & Steppe, K. (2017). Sugars from woody tissue photosynthesis reduce xylem vulnerability to cavitation. *New Phytol.*, 216,
-

720–727.

- Bahn, M., Lattanzi, F.A., Hasibeder, R., Wild, B., Koranda, M., Danese, V., *et al.* (2013). Responses of belowground carbon allocation dynamics to extended shading in mountain grassland. *New Phytol.*, 198, 116–126.
- Bailey, D.L., Karp, J.S. & Surti, S. (2005). Physics and Instrumentation in PET. In: *Positron emission tomography* (eds. Bailey, D., Townsend, D., Valk, P. & Maisey, M.). Springer Berlin, pp. 13–39.
- Beer, S., Streun, M., Hombach, T., Buehler, J., Jahnke, S., Khodaverdi, M., *et al.* (2010). Design and initial performance of PlanTIS: a high-resolution positron emission tomograph for plants. *Phys. Med. Biol.*, 55, 635–646.
- Berveiller, D. & Damesin, C. (2008). Carbon assimilation by tree stems: Potential involvement of phosphoenolpyruvate carboxylase. *Trees - Struct. Funct.*, 22, 149–157.
- Berveiller, D., Kierzkowski, D. & Damesin, C. (2007). Interspecific variability of stem photosynthesis among tree species. *Tree Physiol.*, 27, 53–61.
- Black, M.Z., Minchin, P.E.H., Gould, N., Patterson, K.J. & Clearwater, M.J. (2012). Measurement of Bremsstrahlung radiation for *in vivo* monitoring of <sup>14</sup>C tracer distribution between fruit and roots of kiwifruit (*Actinidia arguta*) cuttings. *Planta*, 236, 1327–1337.
- Bloemen, J., Bauweraerts, I., De Vos, F., Vanhove, C., Vandenberghe, S., Boeckx, P., *et al.* (2015). Fate of xylem-transported <sup>11</sup>C- and <sup>13</sup>C-labeled CO<sub>2</sub> in leaves of poplar. *Physiol. Plant.*, 153, 555–564.
- Bloemen, J., McGuire, M.A., Aubrey, D.P., Teskey, R.O. & Steppe, K. (2013a). Internal recycling of respired CO<sub>2</sub> may be important for plant functioning under changing climate regimes. *Plant Signal. Behav.*, 8.
- Bloemen, J., McGuire, M.A., Aubrey, D.P., Teskey, R.O. & Steppe, K. (2013b). Transport of root-respired CO<sub>2</sub> via the transpiration stream affects aboveground carbon assimilation and CO<sub>2</sub> efflux in trees. *New Phytol.*, 197, 555–565.
- Bloemen, J., McGuire, M.A., Aubrey, D.P., Teskey, R.O. & Steppe, K. (2013c). Assimilation of xylem-transported CO<sub>2</sub> is dependent on transpiration rate but is small relative to

- atmospheric fixation. *J. Exp. Bot.*, 64, 2129–2138.
- Bloemen, J., Teskey, R.O., McGuire, M.A., Aubrey, D.P. & Steppe, K. (2016a). Root xylem CO<sub>2</sub> flux: an important but unaccounted-for component of root respiration. *Trees - Struct. Funct.*, 30, 343–352.
- Bloemen, J., Vergeynst, L.L., Overlaet-Michiels, L. & Steppe, K. (2016b). How important is woody tissue photosynthesis in poplar during drought stress? *Trees - Struct. Funct.*, 30, 63–72.
- Boellaard, R., van Lingen, A. & Lammertsma, A.A. (2001). Experimental and clinical evaluation of iterative reconstruction (OSEM) in dynamic PET: quantitative characteristics and effects on kinetic modeling. *J. Nucl. Med.*, 42, 808–817.
- Browne, J. & De Pierru, A.R. (1996). A row-action alternative to the EM algorithm for maximizing likelihoods in emission tomography. *IEEE Trans. Med. Imaging*, 15, 687–699.
- Bühler, J., Huber, G., Schmid, F. & Blümler, P. (2011a). Analytical model for long-distance tracer-transport in plants. *J. Theor. Biol.*, 270, 70–79.
- Bühler, J., Von Lieres, E. & Huber, G. (2014). A class of compartmental models for long-distance tracer transport in plants. *J. Theor. Biol.*, 341, 131–142.
- Bühler, J., von Lieres, E. & Huber, G.J. (2018). Model-Based Design of Long-Distance Tracer Transport Experiments in Plants. *Front. Plant Sci.*, 9.
- Butler, J.N. (1991). *Carbon Dioxide Equilibria and their Applications*. 1st editio. CRC Press, New York, NY.
- Caird, M.A., Richards, J.H. & Donovan, L.A. (2007). Nighttime stomatal conductance and transpiration in C<sub>3</sub> and C<sub>4</sub> plants. *Plant Physiol.*, 143, 4–10.
- Caudullo, G. & de Rigo, D. (2016). *Populus tremula* in Europe: distribution, habitat, usage and threats. In: *European Atlas of Forest Tree Species* (eds. San-Miguel-Ayanz, J., de Rigo, D., Caudullo, G., T., H.D. & Mauri, A.). Publication Office of the European Union, Luxembourg, pp. 138–139.
- Cernusak, L.A. & Cheesman, A.W. (2015). The benefits of recycling: How photosynthetic bark can increase drought tolerance. *New Phytol.*, 208, 995–997.
- Cernusak, L.A. & Marshall, J.D. (2000). Photosynthetic relaxation in branches of Western

- White Pine. *Funct. Ecol.*, 14, 300–311.
- Chen, X., Gao, J., Zhao, P., McCarthy, H.R., Zhu, L., Ni, G., *et al.* (2018). Tree species with photosynthetic stems have greater nighttime sap flux. *Front. Plant Sci.*, 9, 1–9.
- Cho, Z.H., Chan, J.K., Ericksson, L., Singh, M., Graham, S. & MacDonald, N.S. (1975). Positron ranges obtained from biomedically important positronemitting radionuclides. *J. Nucl. Med.*, 16, 1174–1176.
- van Cleve, B., Forreiter, C., Sauter, J.J. & Apel, K. (1993). Pith cells of poplar contain photosynthetically active chloroplasts. *Planta*, 189, 70–73.
- Comstock, J. & Ehleringer, J. (1990). Effect of Variations in Leaf Size on Morphology and Photosynthetic Rate of Twigs. *Funct. Ecol.*, 4, 209–221.
- Dawson, T.E., Burgess, S.S.O., Tu, K.P., Oliveira, R.S., Santiago, L.S., Fisher, J.B., *et al.* (2007). Nighttime transpiration in woody plants from contrasting ecosystems. *Tree Physiol.*, 27, 561–575.
- Dirks, R.C., Singh, M., Potter, G.S., Sobotka, L.G. & Schaefer, J. (2012). Carbon partitioning in soybean (*Glycine max*) leaves by combined  $^{11}\text{C}$  and  $^{13}\text{C}$  labeling. *New Phytol.*, 196, 1109–21.
- Duan, Q., Sorooshian, S. & Gupta, V.K. (1994). Optimal use of the SCE-UA global optimization method for calibrating watershed models. *J. Hydrol.*, 158, 265–284.
- Duan, Q.Y., Gupta, V.K. & Sorooshian, S. (1993). Shuffled complex evolution approach for effective and efficient global minimization. *J. Optim. Theory Appl.*, 76, 501–521.
- Epila, J., Hubeau, M. & Steppe, K. (2018). Drought effects on photosynthesis and implications of photoassimilate distribution in  $^{11}\text{C}$ -labeled leaves in the African tropical tree species *Maesopsis eminii* Engl. *Forests*, 9.
- Epron, D., Bahn, M., Derrien, D., Lattanzi, F.A., Pumpanen, J., Gessler, A., *et al.* (2012). Pulse-labelling trees to study carbon allocation dynamics: a review of methods, current knowledge and future prospects. *Tree Physiol.*, 32, 776–98.
- España, S., Marcinkowski, R., Keereman, V., Vandenberghe, S. & Van Holen, R. (2014). DigiPET: Sub-millimeter spatial resolution small-animal PET imaging using thin monolithic scintillators. *Phys. Med. Biol.*, 59, 3405–3420.
- Evert, R.F., Eichorn, S.E. & Raven, P.H. (2013). *Raven Biology of Plants*. Eight edit. W.H.

- Freeman and Company, New York.
- Fares, Y., Goeschl, J.D., Magnuson, C.E., Scheld, H.W. & Strain, B.R. (1988). Tracer kinetics of plants carbon allocation with continuously produced  $^{14}\text{C}$ . *J. Radioanal. Nucl. Chem. Artic.*, 124, 105–122.
- Farquhar, G.D. (1989). Carbon Isotope Discrimination and Photosynthesis. *Annu. Rev. Plant Physiol. Plant Mol. Biol.*, 40, 503–537.
- Farrar, J.F., Minchin, P.E.H. & Thorpe, M.R. (1995). Carbon import into barley roots: Effects of sugars and relation to cell expansion. *J. Exp. Bot.*, 46, 1859–1865.
- Fatangare, A. & Svatoš, A. (2016). Applications of 2-deoxy-2-fluoro-D-glucose (FDG) in Plant Imaging: Past, Present, and Future. *Front. Plant Sci.*, 7, 1–11.
- Ferrieri, R.A., Gray, D.W., Babst, B.A., Schueller, M.J., Schlyer, D.J., Thorpe, M.R., *et al.* (2005). Use of carbon-11 in *Populus* shows that exogenous jasmonic acid increases biosynthesis of isoprene from recently fixed carbon. *Plant, Cell Environ.*, 28, 591–602.
- Fine, E.J., Herbst, L., Jelicks, L.A., Koba, W. & Theele, D. (2014). Small-animal research imaging devices. *Semin. Nucl. Med.*, 44, 57–65.
- Fleming, I.N., Manavaki, R., Blower, P.J., West, C., Williams, K.J., Harris, A.L., *et al.* (2015). Imaging tumour hypoxia with positron emission tomography. *Br. J. Cancer*, 112, 238–250.
- Furbank, R.T., Chitty, J.A., Jenkins, C.L.D., Taylor, W.C., Trevanion, S.J., Von Caemmere, S., *et al.* (1997). Genetic manipulation of key photosynthetic enzymes in the  $\text{C}_4$  plant *Flaveria bidentis*. *Aust. J. Plant Physiol.*, 24, 477–485.
- Furze, M.E., Trumbore, S. & Hartmann, H. (2018). Detours on the phloem sugar highway: stem carbon storage and remobilization. *Curr. Opin. Plant Biol.*, 43, 89–95.
- Garbout, A., Munkholm, L.J., Hansen, S.B., Petersen, B.M., Munk, O.L. & Pajor, R. (2012). The use of PET/CT scanning technique for 3D visualization and quantification of real-time soil/plant interactions. *Plant Soil*, 352, 113–127.
- Golman, K., Petersson, J.S., Magnusson, P., Johansson, E., Åkeson, P., Chai, C.M., *et al.* (2008). Cardiac metabolism measured noninvasively by hyperpolarized  $^{13}\text{C}$  MRI. *Magn. Reson. Med.*, 59, 1005–1013.
- Griboaud, I., Novello, V. & Restagno, M. (2001). Improved control of water loss from

- micropropagated grapevines (*Vitis vinifera* cv. Nebbiolo). *Vitis*, 40, 137–140.
- Griffiths, H., Weller, G., Toy, L.F.M. & Dennis, R.J. (2013). You're so vein: Bundle sheath physiology, phylogeny and evolution in C<sub>3</sub> and C<sub>4</sub> plants. *Plant, Cell Environ.*, 36, 249–261.
- Hanik, N., Gómez, S., Best, M., Schueller, M., Orians, C.M. & Ferrieri, R.A. (2010). Partitioning of New Carbon as <sup>11</sup>C in *Nicotiana tabacum* Reveals Insight into Methyl Jasmonate Induced Changes in Metabolism. *J. Chem. Ecol.*, 36, 1058–1067.
- Hari, P., Nygren, P. & Korpilahti, E. (1991). Internal circulation of carbon within a tree. *Can. J. For. Res.*, 21, 514.
- Hartmann, H. & Trumbore, S. (2016). Understanding the roles of nonstructural carbohydrates in forest trees - from what we can measure to what we want to know. *New Phytol.*, 211, 386–403.
- Hevesy, G. (1923). The Absorption and Translocation of Lead by Plants. A Contribution to the Application of the Method of Radioactive Indicators in the Investigation of the Change of Substance in Plants. *Biochem. J.*, 17, 439–445.
- Hibberd, J.M. & Quick, W.P. (2002). Characteristics of C<sub>4</sub> photosynthesis in stems and petioles of C<sub>3</sub> flowering plants. *Nature*, 415, 451–454.
- Hidaka, K., Miyoshi, Y., Ishii, S., Suzui, N., Yin, Y.-G., Kurita, K., *et al.* (2019). Dynamic Analysis of Photosynthate Translocation Into Strawberry Fruits Using Non-invasive <sup>11</sup>C-Labeling Supported With Conventional Destructive Measurements Using <sup>13</sup>C-Labeling. *Front. Plant Sci.*, 9, 1–12.
- Hillier, S.G. & Lathe, R. (2019). Terpenes, hormones and life: isoprene rule revisited. *J. Endocrinol.*, 242, R9–R22.
- Hilman, B., Muhr, J., Trumbore, S.E., Kunert, N., Carbone, M.S., Yuval, P., *et al.* (2019). Comparison of CO<sub>2</sub> and O<sub>2</sub> fluxes demonstrate retention of respired CO<sub>2</sub> in tree stems from a range of tree species. *Biogeosciences*, 16, 177–191.
- Hodoušek, M., Dias, A.M.P.G., Martins, C., Marques, A.F.S. & Böhm, M. (2017). Comparison of non-destructive methods based on natural frequency for determining the modulus of elasticity of *Cupressus lusitanica* and *Populus x canadensis*. *BioResources*, 12, 270–282.

- 
- Hölttä, T. & Kolari, P. (2009). Interpretation of stem CO<sub>2</sub> efflux measurements. *Tree Physiol.*, 29, 1447–1456.
- Hölttä, T., Mencuccini, M. & Nikinmaa, E. (2009). Linking phloem function to structure: Analysis with a coupled xylem-phloem transport model. *J. Theor. Biol.*, 259, 325–337.
- Hölttä, T., Vesala, T., Sevanto, S., Perämäki, M. & Nikinmaa, E. (2006). Modeling xylem and phloem water flows in trees according to cohesion theory and Münch hypothesis. *Trees - Struct. Funct.*, 20, 67–78.
- Hubeau, M., Mincke, J., Vanhove, C., Courty, J., Vandenberghe, S. & Steppe, K. (2018). Plant-PET to investigate phloem vulnerability to drought in *Populus tremula* under changing climate regimes. *Tree Physiol.*, 39, 211–221.
- Hubeau, M., Mincke, J., Vanhove, C., Gorel, A.P., Fayolle, A., Epila, J., et al. (2019a). <sup>14</sup>C-Autoradiographs to Image Phloem Loading. *Front. For. Glob. Chang.*, 2, 1–11.
- Hubeau, M. & Steppe, K. (2015). Plant-PET Scans: *In Vivo* Mapping of Xylem and Phloem Functioning. *Trends Plant Sci.*, 20, 676–685.
- Hubeau, M., Thorpe, M.R., Mincke, J., Bloemen, J., Bauweraerts, I., Minchin, P.E.H., et al. (2019b). High-resolution *in vivo* imaging of xylem-transported CO<sub>2</sub> in leaves based on real-time <sup>11</sup>C-tracing. *Front. For. Glob. Chang.*, 2.
- Ishioaka, N.S., Matsuoka, H., Watanabe, S., Osa, A., Koizumi, M., Kume, T., et al. (1999). Production of positron emitters and application of their labeled compounds to plant studies. *J. Radioanal. Nucl. Chem.*, 239, 417–421.
- Jahnke, S., Menzel, M.I., Van Dusschoten, D., Roeb, G.W., Bühler, J., Minwuyelet, S., et al. (2009). Combined MRI-PET dissects dynamic changes in plant structures and functions. *Plant J.*, 59, 634–644.
- Jahnke, S., Schlesinger, U., Feige, G.B. & Knust, E.J. (1998). Transport of photoassimilates in young trees of *Fraxinus* and *sorbus*: Measurement of translocation *in vivo*. *Bot. Acta*, 111, 307–315.
- James, M.L. & Gambhir, S.S. (2012). A molecular imaging primer: Modalities, imaging agents, and applications. *Physiol. Rev.*, 92, 897–965.
- Janacek, S.H., Trenkamp, S., Palmer, B., Brown, N.J., Parsley, K., Stanley, S., et al. (2009). Photosynthesis in cells around veins of the C<sub>3</sub> plant *Arabidopsis thaliana* is important
-

- for both the shikimate pathway and leaf senescence as well as contributing to plant fitness. *Plant J.*, 59, 329–343.
- Jenkins, C.L.D., Furbank, R.T. & Hatch, M.D. (1989). Inorganic Carbon Diffusion between C4 Mesophyll and Bundle Sheath Cells. *Plant Physiol.*, 91, 1356–1363.
- Jensen, K.H., Rio, E., Hansen, R., Clanet, C. & Bohr, T. (2009). Osmotically driven pipe flows and their relation to sugar transport in plants. *J. Fluid Mech.*
- Jodal, L., Le Loirec, C. & Champion, C. (2012). Positron range in PET imaging: An alternative approach for assessing and correcting the blurring. *Phys. Med. Biol.*, 57, 3931–3943.
- Karve, A.A., Alexoff, D., Kim, D., Schueller, M.J., Ferrieri, R.A. & Babst, B.A. (2015). *In vivo* quantitative imaging of photoassimilate transport dynamics and allocation in large plants using a commercial positron emission tomography (PET) scanner. *BMC Plant Biol.*, 15, 273.
- Kawachi, N., Fujimaki, S., Sakamoto, K., Ishioka, N.S., Matsushashi, S. & Sekimoto, H. (2008). Analysis of NO<sub>3</sub> interception of the parasitic angiosperm *Orobanche* spp. using a positron-emitting tracer imaging system and <sup>13</sup>NO<sub>3</sub>: A new method for the visualization and quantitative analysis of the NO<sub>3</sub> interception ratio. *Soil Sci. Plant Nutr.*, 54, 408–416.
- Kawachi, N., Kikuchi, K., Suzui, N., Ishii, S., Fujimaki, S., Ishioka, N.S., *et al.* (2011). Imaging of carbon translocation to fruit using carbon-11-labeled carbon dioxide and positron emission tomography. *IEEE Trans. Nucl. Sci.*, 58, 395–399.
- Kawachi, N., Sakamoto, K., Ishii, S., Fujimaki, S., Suzui, N., Ishioka, N.S., *et al.* (2006). Kinetic analysis of carbon-11-labeled carbon dioxide for studying photosynthesis in a leaf using positron emitting tracer imaging system. *IEEE Trans. Nucl. Sci.*, 53, 2991–2997.
- Kharouk, V.I., Middleton, E.M., Spencer, S.L., Rock, B.N. & Williams, D.L. (1995). Aspen bark photosynthesis and its significance to remote sensing and carbon budget estimates in the boreal ecosystem. *Water, Air Soil Pollut.*, 82, 483–497.
- Kikuchi, K., Ishii, S., Fujimaki, S., Suzui, N., Matsushashi, S., Honda, I., *et al.* (2008). Real-time Analysis of Photoassimilate Translocation in Intact Eggplant Fruit using <sup>11</sup>CO<sub>2</sub> and a Positron-emitting Tracer Imaging System. *J. Japanese Soc. Hortic. Sci.*, 77, 199–205.



- Kim, E.E., Lee, M.-C., Inoue, T. & Wong, W. (Eds.). (2013). *Clinical PET and PET/CT: Principles and Applications*. Springer, New York, NY.
- Kiser, M.R., Reid, C.D., Crowell, A.S., Phillips, R.P. & Howell, C.R. (2008). Exploring the transport of plant metabolites using positron emitting radiotracers. *HFSP J.*, 2, 189–204.
- Kishimoto, S., Brender, J.R., Crooks, D.R., Matsumoto, S., Seki, T., Oshima, N., *et al.* (2019). Imaging of glucose metabolism by  $^{13}\text{C}$ -MRI distinguishes pancreatic cancer subtypes in mice. *Elife*, 8, 1–20.
- Kiyomiya, S., Nakanishi, H., Uchida, H., Nishiyama, S., Tsukada, H., Ishioka, N.S., *et al.* (2001a). Light activates  $\text{H}_2[^{15}\text{O}]$  flow in rice: Detailed monitoring using a positron-emitting tracer imaging system (PETIS). *Physiol. Plant.*, 113, 359–367.
- Kiyomiya, S., Nakanishi, H., Uchida, H., Tsuji, A., Nishiyama, S., Futatsubashi, M., *et al.* (2001b). Real time visualization of  $^{13}\text{N}$ -translocation in rice under different environmental conditions using positron emitting tracer imaging system. *Plant Physiol.*, 125, 1743–1754.
- Knoblauch, M. & Peters, W.S. (2010). Münch, morphology, microfluidics - our structural problem with the phloem. *Plant, Cell Environ.*
- Kogan, F., Broski, S.M., Yoon, D. & Gold, G.E. (2018). Applications of PET-MRI in musculoskeletal disease. *J. Magn. Reson. Imaging*, 48, 27–47.
- Kume, T., Matsuhashi, S., Shimazu, M., Ito, H., Fujimura, T., Adachi, K., *et al.* (1997). Uptake and transport of positron-emitting tracer ( $^{18}\text{F}$ ) in plants. *Appl. Radiat. Isot.*, 48, 1035–1043.
- Kutta, W. (1901). Beitrag zur näherungsweise Integration totaler Differentialgleichungen. *Math. Phys.*, 46, 435–453.
- Lakhwani, O.P., Dalal, V., Jindal, M. & Nagala, A. (2019). Radiation protection and standardization. *J. Clin. Orthop. Trauma*, 10, 738–743.
- Landais, P. & Finn, R. (1989). On-line preparation of  $[^{11}\text{C}]$ carbon dioxide from  $[^{11}\text{C}]$ methane. *Int. J. Radiat. Appl. Instrumentation. Part A. Appl. Radiat. Isot.*, 40, 265–266.
- Landhäuser, S.M. & Lieffers, V.J. (2003). Seasonal changes in carbohydrate reserves in

- mature northern *Populus tremuloides* clones. *Trees - Struct. Funct.*, 17, 471–476.
- Levin, C.S. (2005). Primer on molecular imaging technology. *Eur. J. Nucl. Med. Mol. Imaging*, 32, 325–345.
- Levy, P.E., Meir, P., Allen, S.J. & Jarvis, P.G. (1999). The effect of aqueous transport of CO<sub>2</sub> in xylem sap on gas exchange in woody plants. *Tree Physiol.*, 19, 53–58.
- Liang, W., Nie, Y., Wang, J., Wu, J., Liu, H., Wang, Q., *et al.* (2011). Three-dimensional positron emission tomography/computed tomography analysis of <sup>13</sup>NO<sub>3</sub>- uptake and <sup>13</sup>N distribution in growing kohlrabi. *Anal. Chem.*, 83, 578–584.
- Lichtenthaler, H.K. & Zeidler, J.G. (2002). Isoprene and terpene biosynthesis. In: *Trace Gas Exchange in Forest Ecosystems. Tree Physiology, vol 3* (ed. Gasche R., Papen H., R.H.). Springer Dordrecht, pp. 79–99.
- Litton, C.M., Raich, J.W. & Ryan, M.G. (2007). Carbon allocation in forest ecosystems. *Glob. Chang. Biol.*, 13, 2089–2109.
- Loening, A.M. & Gambhir, S.S. (2003). AMIDE: A Free Software Tool for Multimodality Medical Image Analysis. *Mol. Imaging*, 2, 131–137.
- Lucas, W.J., Groover, A., Lichtenberger, R., Furuta, K., Yadav, S.R., Helariutta, Y., *et al.* (2013). The Plant Vascular System: Evolution, Development and Functions. *J. Integr. Plant Biol.*, 55, 294–388.
- Maguire, J.J., Kuc, R.E. & Davenport, A.P. (2012). Quantitative Phosphor Imaging Autoradiography of Radioligands for Positron Emission Tomography. In: *Receptor Binding Techniques, Methods in Molecular Biology* (ed. Davenport, A.P.). Humana Press, Cambridge, pp. 205–220.
- Maier, C.A., Johnsen, K.H., Clinton, B.D. & Ludovici, K.H. (2010). Relationships between stem CO<sub>2</sub> efflux, substrate supply, and growth in young loblolly pine trees. *New Phytol.*, 185, 502–513.
- McClendon, J.H. (1992). Photographic Survey of the Occurrence of Bundle-Sheath Extensions in Deciduous Dicots. *Plant Physiol.*, 99, 1677–1679.
- McGuire, M.A., Cerasoli, S. & Teskey, R.O. (2007). CO<sub>2</sub> fluxes and respiration of branch segments of sycamore (*Platanus occidentalis* L.) examined at different sap velocities, branch diameters, and temperatures. *J. Exp. Bot.*, 58, 2159–2168.

- McGuire, M.A., Marshall, J.D. & Teskey, R.O. (2009). Assimilation of xylem-transported  $^{13}\text{C}$ -labelled  $\text{CO}_2$  in leaves and branches of sycamore (*Platanus occidentalis* L.). *J. Exp. Bot.*, 60, 3809–3817.
- McGuire, M.A. & Teskey, R.O. (2002). Microelectrode technique for *in situ* measurement of carbon dioxide concentrations in xylem sap of trees. *Tree Physiol.*, 22, 807–811.
- McGuire, M.A. & Teskey, R.O. (2004). Estimating stem respiration in trees by a mass balance approach that accounts for internal and external fluxes of  $\text{CO}_2$ . *Tree Physiol.*, 24, 571–578.
- Merritt, M.E., Harrison, C., Storey, C., Jeffrey, F.M., Sherry, A.D. & Malloy, C.R. (2007). Hyperpolarized  $^{13}\text{C}$  allows a direct measure of flux through a single enzyme-catalyzed step by NMR. *Proc. Natl. Acad. Sci. U. S. A.*, 104, 19773–19777.
- Minchin, P.E.H. (2007). Mechanistic Modelling of Carbon Partitioning. In: *Functional-Structural Plant Modelling in Crop Production* (eds. Vos, J., Marcelis, L.F.M., de Visser, P.H.B., Struik, P.C. & Evers, J.B.). Springer, pp. 113–122.
- Minchin, P.E.H. (2012). Input-output analysis of phloem partitioning within higher plants. In: *System Identification, Environmental Modelling, and Control System Design* (eds. Wang, L. & Garnier, H.). Springer, London, pp. 519–532.
- Minchin, P.E.H. & Thorpe, M.R. (1984). Apoplastic phloem unloading in the stem of bean. *J. Exp. Bot.*, 35, 538–550.
- Minchin, P.E.H. & Thorpe, M.R. (2003). Using the short-lived isotope  $^{14}\text{C}$  in mechanistic studies of photosynthate transport. *Funct. Plant Biol.*, 30, 831–841.
- Mincke, J., Hubeau, M., Cortyn, J., Brans, B., Vanhove, C., Vandenberghe, S., *et al.* (2018). Normalization of  $^{14}\text{C}$ -autoradiographic images for semi-quantitative analysis of woody tissue photosynthesis. *Acta Hortic.*, 35–42.
- Mori, S., Kiyomiya, S., Nakanishi, H., Ishioka, N.S., Watanabe, S., Osa, A., *et al.* (2000). Visualization of  $^{15}\text{O}$ -water flow in tomato and rice in the light and dark using a positron-emitting tracer imaging system (PETIS). *Soil Sci. Plant Nutr.*, 46, 975–979.
- Münch, E. (1930). *Die Stoffbewegungen in der Pflanze*. Verlag von Gustave Fischer, Jena, Germany.
- Nikinmaa, E., Hölttä, T., Hari, P., Kolari, P., Mäkelä, A., Sevanto, S., *et al.* (2013). Assimilate

- transport in phloem sets conditions for leaf gas exchange. *Plant, Cell Environ.*, 36, 655–669.
- Nilsen, E. (1995). Stem photosynthesis: extent, patterns and rol in plant carbon economy. In: *Plant stems: Physiology and Functional Morphology* (ed. Gartner, B.). Academic Press, San Diego, pp. 223–240.
- Nilsen, E.T., Karpa, D., Mooney, A.H. & Field, C. (1993). Patterns of Stem Photosynthesis in Two Invasive Legumes (*Spartium junceum* , *Cytisus scoparius*) of the California Coastal Region. *Am. J. Bot.*, 80, 1126–1136.
- Nobel, P.S. (2009). *Phytochemical and Environmental Plant Physiology*. Fourth edi. Academic Press, Oxford.
- O’Leary, M.H. (1981). Carbon isotope fractionation in plants. *Phytochemistry*, 20, 553–567.
- Partelová, D., Horník, M., Lesný, J., Rajec, P., Kováč, P. & Hostin, S. (2016). Imaging and analysis of thin structures using positron emission tomography: Thin phantoms and *in vivo* tobacco leaves study. *Appl. Radiat. Isot.*, 115, 87–96.
- De Pauw, D.J.W., Steppe, K. & De Baets, B. (2008). Identifiability analysis and improvement of a tree water flow and storage model. *Math. Biosci.*, 211, 314–332.
- Pfanz, H. (2008). Bark photosynthesis. *Trees - Struct. Funct.*, 22, 137–138.
- Pfanz, H. & Aschan, G. (2001). The Existence of Bark and Stem Photosynthesis in Woody Plants and Its Significance for the Overall Carbon Gain. An Eco-Physiological and Ecological Approach. In: *Progress in Botany* (eds. Esser, K., Lüttge, U., Kadereit, J.W. & Beyschlag, W.). Springer Berlin Heidelberg, Berlin, pp. 477–510.
- Pfanz, H., Aschan, G., Langenfeld-Heysler, R., Wittmann, C. & Loose, M. (2002). Ecology and ecophysiology of tree stems: Corticular and wood photosynthesis. *Naturwissenschaften*, 89, 147–162.
- Pfautsch, S., Renard, J., Tjoelker, M.G. & Salih, A. (2015). Phloem as capacitor: Radial transfer of water into xylem of tree stems occurs via symplastic transport in ray parenchyma. *Plant Physiol.*, 167, 963–971.
- Pickard, W.F. & Minchin, P.E. (1990). The transient inhibition of phloem translocation in *Phaseolus vulgaris* by abrupt temperature drops, vibration, and electric shock. *J. Exp. Bot.*, 41, 1361–1369.

- 
- Pickard, W.F., Minchin, P.E.H. & Thorpe, M.R. (1993). Leaf export and partitioning changes induced by short-term inhibition of phloem transport. *J. Exp. Bot.*, 44, 1491–1496.
- Powers, E.M. & Marshall, J.D. (2011). Pulse labeling of dissolved  $^{13}\text{C}$ -carbonate into tree xylem: Developing a new method to determine the fate of recently fixed photosynthate. *Rapid Commun. Mass Spectrom.*, 25, 33–40.
- Preiss, J. (1984). Starch, sucrose biosynthesis and partition of carbon in plants are regulated by orthophosphate and triose-phosphates. *Trends Biochem. Sci.*, 9, 24–27.
- Pritchard, J., Tomos, A.D., Farrar, J.F., Minchin, P.E.H., Gould, N., Paul, M.J., *et al.* (2004). Turgor, solute import and growth in maize roots treated with galactose. *Funct. Plant Biol.*, 31, 1095–1103.
- Quentin, A.G., Pinkard, E.A., Ryan, M.G., Tissue, D.T., Baggett, L.S., Adams, H.D., *et al.* (2015). Non-structural carbohydrates in woody plants compared among laboratories. *Tree Physiol.*, 35, 1146–1165.
- R Core Team. (2018). *R: A language and environment for statistical computing*. Available at: <https://www.r-project.org/>. Last accessed .
- Reichenbacher, R.R., Schultz, R.C. & Hartl, A.R. (1996). Artificial Defoliation Effect on Populus Growth, Biomass Production, and Total Nonstructural Carbohydrate Concentration. *Environ. Entomol.*, 25, 632–642.
- Rentzou, A. & Psaras, G.K. (2008). Green plastids, maximal PSII photochemical efficiency and starch content of inner stem tissues of three Mediterranean woody species during the year. *Flora Morphol. Distrib. Funct. Ecol. Plants*, 203, 350–357.
- Roeb, G. & Britz, S.J. (1991). Short-term fluctuations in the transport of assimilates to the ear of wheat measured with steady-state  $^{14}\text{C}$ -CO<sub>2</sub>-labelling of the flag leaf. *J. Exp. Bot.*, 42, 469–475.
- De Roo, L., Bloemen, J., Dupon, Y., Salomón, R.L. & Steppe, K. (2019). Axial diffusion of respired CO<sub>2</sub> confounds stem respiration estimates during the dormant season. *Ann. For. Sci.*, 76.
- Rosset, A., Spadola, L. & Ratib, O. (2004). OsiriX: An open-source software for navigating in multidimensional DICOM images. *J. Digit. Imaging*, 17, 205–216.
- Runge, C. (1895). Über die numerische Auflösung von Differentialgleichungen. *Math. Ann.*,

46, 167–178.

Saha, G.B. (2016). *Basics of PET imaging: Physics, chemistry, and regulations, third edition. Basics PET Imaging Physics, Chem. Regul. Third Ed.*

Sala, A., Woodruff, D.R. & Meinzer, F.C. (2012). Carbon dynamics in trees: Feast or famine? *Tree Physiol.*, 32, 764–775.

Salomón, R.L., De Roo, L., Bodé, S., Boeckx, P. & Steppe, K. (2019a). Isotope ratio laser spectroscopy to disentangle xylem-transported from locally respired CO<sub>2</sub> in stem CO<sub>2</sub> efflux. *Tree Physiol.*, 39, 819–830.

Salomón, R.L., De Schepper, V., Valbuena-Carabaña, M., Gil, L. & Steppe, K. (2018). Daytime depression in temperature-normalised stem CO<sub>2</sub> efflux in young poplar trees is dominated by low turgor pressure rather than by internal transport of respired CO<sub>2</sub>. *New Phytol.*, 217, 586–598.

Salomón, R.L., Steppe, K., Crous, K.Y., Noh, N.J. & Ellsworth, D.S. (2019b). Elevated CO<sub>2</sub> does not affect stem CO<sub>2</sub> efflux nor stem respiration in a dry Eucalyptus woodland, but it shifts the vertical gradient in xylem [CO<sub>2</sub>]. *Plant Cell Environ.*, 42, 2151–2164.

Saveyn, A., Steppe, K., Ubierna, N. & Dawson, T.E. (2010). Woody tissue photosynthesis and its contribution to trunk growth and bud development in young plants. *Plant, Cell Environ.*, 33, 1949–1958.

De Schepper, V., De Swaef, T., Bauweraerts, I. & Steppe, K. (2013). Phloem transport: A review of mechanisms and controls. *J. Exp. Bot.*, 64, 4839–4850.

Schmitz, N., Egerton, J.J.G., Lovelock, C.E. & Ball, M.C. (2012). Light-dependent maintenance of hydraulic function in mangrove branches: Do xylary chloroplasts play a role in embolism repair? *New Phytol.*, 195, 40–46.

Schuetz, M., Smith, R. & Ellis, B. (2013). Xylem tissue specification, patterning, and differentiation mechanisms. *J. Exp. Bot.*, 64, 11–31.

Sevanto, S. (2014). Phloem transport and drought. *J. Exp. Bot.*, 65, 1751–1759.

Sevanto, S., Hölttä, T. & Holbrook, N.M. (2011). Effects of the hydraulic coupling between xylem and phloem on diurnal phloem diameter variation. *Plant, Cell Environ.*, 34, 690–703.

Shackel, K.A., Novello, V. & Sutter, E.G. (1990). Stomatal Function and Cuticular

- 
- Conductance in Whole Tissue-cultured Apple Shoots. *J. Am. Soc. Hortic. Sci.*, 115, 468–472.
- Sharkey, T.D., Berry, J.A. & Raschke, K. (1985). Starch and Sucrose Synthesis in *Phaseolus vulgaris* as Affected by Light, CO<sub>2</sub>, and Abscisic Acid. *Plant Physiol.*, 77, 617–620.
- Shepp, L.A. & Vardi, Y. (1982). Maximum Likelihood Reconstruction for Emission Tomography. *IEEE Trans. Med. Imaging*, 1, 113–122.
- Siddiqi, M.Y., Glass, A.D.M., Ruth, T.J. & Fernando, M. (1989). Studies of the Regulation of Nitrate Influx by Barley Seedlings Using <sup>13</sup>NO<sub>3</sub> - . *Plant Physiol.*, 90, 806–813.
- Sihver, S., Sihver, W., Bergström, M., Höglund, A.U., Sjöberg, P., Långström, B., *et al.* (1999). Quantitative autoradiography with short-lived positron emission tomography tracers: A study on muscarinic acetylcholine receptors with N-[<sup>11</sup>C]methyl-4-piperidylbenzilate. *J. Pharmacol. Exp. Ther.*, 290, 917–922.
- Steppe, K., Saveyn, A., McGuire, M.A., Lemeur, R. & Teskey, R.O. (2007). Resistance to radial CO<sub>2</sub> diffusion contributes to between-tree variation in CO<sub>2</sub> efflux of *Populus deltoides* stems. *Funct. Plant Biol.*, 34, 785–792.
- Steppe, K., Sterck, F. & Deslauriers, A. (2015). Diel growth dynamics in tree stems: Linking anatomy and ecophysiology. *Trends Plant Sci.*, 20, 335–343.
- Stitt, M. & Zeeman, S.C. (2012). Starch turnover: Pathways, regulation and role in growth. *Curr. Opin. Plant Biol.*, 15, 282–292.
- Stringer, J.W. & Kimmerer, T.W. (1993). Refixation of xylem sap CO<sub>2</sub> in *Populus deltoides*. *Physiol. Plant.*, 89, 243–251.
- Stroock, A.D., Pagay, V. V., Zwieniecki, M.A. & Michele Holbrook, N. (2014). The Physicochemical Hydrodynamics of Vascular Plants. *Annu. Rev. Fluid Mech.*, 46, 615–642.
- Stutz, S.S., Anderson, J., Zulick, R. & Hanson, D.T. (2017). Inside out: Efflux of carbon dioxide from leaves represents more than leaf metabolism. *J. Exp. Bot.*, 68, 2849–2857.
- Stutz, S.S. & Hanson, D.T. (2019a). Contribution and consequences of xylem-transported CO<sub>2</sub> assimilation for C<sub>3</sub> plants. *New Phytol.*, 223, 1230–1240.
- Stutz, S.S. & Hanson, D.T. (2019b). What is the fate of xylem-transported CO<sub>2</sub> in Kranz-
-

- type C<sub>4</sub> plants? *New Phytol.*, 223, 1241–1252.
- Taiz, L. & Zeiger, E. (2010). *Plant Physiology*. 5th edn. Sinauer Associates, Inc. Publishers, Sunderland, Massachusetts, USA.
- Tanner, W. & Beevers, H. (2001). Transpiration, a prerequisite for long-distance transport of minerals in plants? *Proc. Natl. Acad. Sci. U. S. A.*, 98, 9443–9447.
- Tarvainen, L., Wallin, G., Lim, H., Linder, S., Oren, R., Löfvenius, M.O., *et al.* (2017). Photosynthetic refixation varies along the stem and reduces CO<sub>2</sub> efflux in mature boreal *Pinus sylvestris* trees. *Tree Physiol.*, 38, 558–569.
- Teskey, R., McGuire, M., Bloemen, J., Aubrey, D. & Steppe, K. (2017). Plant respiration: metabolic fluxes and carbon balance. In: *Respiration and CO<sub>2</sub> fluxes in trees* (eds. Tcherkez, G. & Ghashghaie, J.). Springer International Publishing, Cham, pp. 181–207.
- Teskey, R., Teskey, R.O., Saveyn, A., Steppe, K. & McGuire, M.A. (2008). Origin, fate and significance of CO<sub>2</sub> in tree stems. *New Phytol.*, 177, 17–32.
- Teskey, R.O. & McGuire, M.A. (2007). Measurement of stem respiration of sycamore (*Platanus occidentalis* L.) trees involves internal and external fluxes of CO<sub>2</sub> and possible transport of CO<sub>2</sub> from roots. *Plant, Cell Environ.*, 30, 570–579.
- Teskey, R.O. & McGuire, M.A. (2002). Carbon dioxide transport in xylem causes errors in estimation of rates of respiration in stems and branches of trees. *Plant, Cell Environ.*, 25, 1571–1577.
- Thornley, J.H.M. (2011). Plant growth and respiration re-visited: Maintenance respiration defined it is an emergent property of, not a separate process within, the system and why the respiration: Photosynthesis ratio is conservative. *Ann. Bot.*, 108, 1365–1380.
- Thorpe, M.R., Ferrieri, A.P., Herth, M.M. & Ferrieri, R. a. (2007). <sup>11</sup>C-imaging: Methyl jasmonate moves in both phloem and xylem, promotes transport of jasmonate, and of photoassimilate even after proton transport is decoupled. *Planta*, 226, 541–551.
- Thorpe, M.R., Minchin, P.E.H., Williams, J.H.H., Farrar, J.F. & Tomos, A.D. (1993). Carbon import into developing ovules of *Pisum sativum*: The role of the water relations of the seed coat. *J. Exp. Bot.*, 44, 937–945.
- Traversari, S., Emiliani, G., Traversi, M.L., Anichini, M. & Giovannelli, A. (2018). Pattern of carbohydrate changes in maturing xylem and phloem during growth to dormancy



- transition phase in picea abies (L.) Karst. *Dendrobiology*, 80, 12–23.
- Troughton, J.H., Chang, F.H. & Currie, B.G. (1974). Estimates of mean speed of translocation in leaves of *Oryza sativa* L. *Plant Sci. Lett.*, 3, 49–54.
- Trumbore, S.E., Angert, A., Kunert, N., Muhr, J. & Chambers, J.Q. (2013). What's the flux? Unraveling how CO<sub>2</sub> fluxes from trees reflect underlying physiological processes. *New Phytol.*, 197, 353–355.
- Tsukamoto, T., Nakanishi, H., Uchida, H., Watanabe, S., Matsushashi, S., Mori, S., *et al.* (2009). <sup>52</sup>Fe translocation in barley as monitored by a positron-emitting tracer imaging system (PETIS): Evidence for the direct translocation of Fe from roots to young leaves via phloem. *Plant Cell Physiol.*, 50, 48–57.
- Turgeon, R. & Wolf, S. (2009). Phloem Transport: Cellular Pathways and Molecular Trafficking. *Annu. Rev. Plant Biol.*
- Turkheimer, F.E., Veronese, M. & Dunn, J. (2014). *Experimental Design and Practical Data Analysis in Positron Emission Tomography*. 1st Editio. CreateSpace Independent Publishing Platform, London.
- Uchida, H., Okamoto, T., Ohmura, T., Shimizu, K., Satoh, N., Koike, T., *et al.* (2004). A compact planar positron imaging system. *Nucl. Instruments Methods Phys. Res. Sect. A Accel. Spectrometers, Detect. Assoc. Equip.*, 516, 564–574.
- Vandegheuchte, M.W., Bloemen, J., Vergeynst, L.L. & Steppe, K. (2015). Woody tissue photosynthesis in trees: Salve on the wounds of drought? *New Phytol.*, 208, 998–1002.
- Vandenberghe, S. & Marsden, P.K. (2015). PET-MRI: A review of challenges and solutions in the development of integrated multimodality imaging. *Phys. Med. Biol.*, 60, R115–R154.
- Vandenberghe, S., Mikhaylova, E., D'Hoe, E., Mollet, P. & Karp, J.S. (2016). Recent developments in time-of-flight PET. *EJNMMI Phys.*, 3.
- Wang, Q., Mathews, A.J., Li, K., Wen, J., Komarov, S., O'Sullivan, J.A., *et al.* (2014). A dedicated high-resolution PET imager for plant sciences. *Phys. Med. Biol.*, 59, 5613–29.
- Wang, X., Mao, Z., McGuire, M.A. & Teskey, R.O. (2019). Stem radial CO<sub>2</sub> conductance

- affects stem respiratory CO<sub>2</sub> fluxes in ash and birch trees. *J. For. Res.*, 30, 21–29.
- Weisenberger, A.G., Kross, B., Lee, S., McKisson, J., McKisson, J.E., Xi, W., *et al.* (2012). PhytoBeta imager: a positron imager for plant biology. *Phys. Med. Biol.*, 57, 4195–4210.
- Wickline, S.A. & Lanza, G.M. (2002). Molecular imaging, targeted therapeutics, and nanoscience. *J. Cell. Biochem.*, 39, 90–97.
- Windt, C.W., Vergeldt, F.J., De Jager, P.A. & Van As, H. (2006). MRI of long-distance water transport: A comparison of the phloem and xylem flow characteristics and dynamics in poplar, castor bean, tomato and tobacco. *Plant, Cell Environ.*, 29, 1715–1729.
- Witkowski, E.T.F. & Lamont, B.B. (1991). Leaf Specific Mass Confounds Leaf Density and Thickness. *Oecologia*, 88, 486–493.
- Wittmann, C., Aschan, G. & Pfanz, H. (2001). Leaf and twig photosynthesis of young beech (*Fagus sylvatica*) and aspen (*Populus tremula*) trees grown under different light regime. *Basic Appl. Ecol.*, 2, 145–154.
- Wittmann, C. & Pfanz, H. (2008). Antitranspirant functions of stem periderms and their influence on cortical photosynthesis under drought stress. *Trees - Struct. Funct.*, 22, 187–196.
- Wittmann, C. & Pfanz, H. (2018). More than just CO<sub>2</sub>-recycling: cortical photosynthesis as a mechanism to reduce the risk of an energy crisis induced by low oxygen. *New Phytol.*, 219, 551–564.
- Wu, H. & Tai, Y.-C. (2011). A novel phoswich imaging detector for simultaneous beta and coincidence-gamma imaging of plant leaves. *Phys. Med. Biol.*, 56, 5583–5598.
- Yamazaki, H., Suzui, N., Yin, Y.G., Kawachi, N., Ishii, S., Shimada, H., *et al.* (2015). Live-imaging evaluation of the efficacy of elevated CO<sub>2</sub> concentration in a closed cultivation system for the improvement of bioproduction in tomato fruits. *Plant Biotechnol.*, 32, 31–37.
- Yamori, W., Hikosaka, K. & Way, D.A. (2014). Temperature response of photosynthesis in C<sub>3</sub>, C<sub>4</sub>, and CAM plants: Temperature acclimation and temperature adaptation. *Photosynth. Res.*, 119, 101–117.
- Zanzonico, P. (2012). Principles of Nuclear Medicine Imaging: Planar, SPECT, PET, Multi-

- modality, and Autoradiography Systems. *Radiat. Res.*, 177, 349–364.
- Zeppel, M.J.B., Lewis, J.D., Phillips, N.G. & Tissue, D.T. (2014). Consequences of nocturnal water loss: A synthesis of regulating factors and implications for capacitance, embolism and use in models. *Tree Physiol.*, 34, 1047–1055.
- Zwieniecki, M.A., Melcher, P.J. & Holbrook, N.M. (2001). Hydrogel control of xylem hydraulic resistance in plants. *Science (80)*, 291, 1059–1062.



S

SUMMARY



Understanding and characterising variations in plant respiration is of utmost importance for global change science, as well as fundamental to plant ecology and physiology. This, because the efflux of CO<sub>2</sub> from plant respiratory processes is a meaningful yet uncertain component of plant, ecosystem, and global carbon budgets. As it was previously assumed that CO<sub>2</sub> produced by respiration in woody tissues escapes almost immediately to the atmosphere, observations over the last 20 years have demonstrated that a large quantity of respired CO<sub>2</sub> remains inside trees. This locally produced internal CO<sub>2</sub> is substantially higher in concentration (generally between 3 and 10%, and sometimes up to 26%) than the atmospheric CO<sub>2</sub> concentration (~0,04%). An emerging understanding of the involved processes also indicated that a considerable amount of the respired CO<sub>2</sub> dissolves in xylem sap to be transported upwards, away from the site of intake. Subsequently, a portion of this xylem-transported CO<sub>2</sub> can escape to the atmosphere via efflux while photosynthetic active cells in woody tissues or leaves can fix another portion. Although progress has been made, our understanding of xylem-transported CO<sub>2</sub> in relation to plant respiration can be expanded as its dynamic fate at small spatial and temporal scale is still uncertain. Additionally, its assimilation of internal CO<sub>2</sub> by woody tissue photosynthesis has to date only been assumed as the actual fixation and conversion to sugars has not been evidenced.

In this PhD thesis, the focus was to unravel the secrets of xylem-transported CO<sub>2</sub> by studying its dynamics on a submillimetre scale. This was enabled through application of medical imaging techniques based on the detection of positron-decaying isotopes. Two techniques were proposed, i.e. positron autoradiography and positron emission tomography (PET). Both positron-based imaging methods allow *in vivo* experiments to study and even visualise biological processes with high spatial resolution. Compared to their extensive application in clinical and pre-clinical setting, however, only limited number of research groups worldwide report positron-based studies which might be related to the complexity involved in these techniques. As we are confident that these techniques have immense potential in the way that they could contribute extensively to plant science, a broad outline was provided in this PhD thesis on how to design and execute positron-based experiments on plant tissues. Hereby the emphasis was centred around tracing radioactive <sup>11</sup>CO<sub>2</sub> by PET although some basics on positron autoradiography are provided.

Throughout this PhD thesis, research is conducted on 1-year old poplar tree species, i.e. *Populus × canadensis* Moench “Robusta” and *Populus tremula* L.. These species are characterised by rapid growth and a naturally high bark chlorophyll concentration making them ideal candidates to study xylem-transported CO<sub>2</sub> and its relation to woody tissue photosynthesis. In this research, four main steps were taken towards unravelling the dynamics of xylem-transported CO<sub>2</sub>:

- ◇ First, possibility of using both PET and positron autoradiography was tested towards studying internally transported CO<sub>2</sub> in leaves. Therefore, a method was developed to label plant tissues with <sup>11</sup>C in a half-open set-up. Labelling occurred through supplying an <sup>11</sup>C-enriched solution to the petiole of detached leaves. During labelling, air was continuously supplied to the leaves, as to maintain regular photosynthesis, while taking into account the hazards concerning radioactive <sup>11</sup>C that might potentially be released as a gas. Manipulating intern CO<sub>2</sub> transport, via light exclusion or prevented transpiration on leaf level, demonstrated applicability of both PET and autoradiography towards studying the dynamic behaviour of xylem-transported <sup>11</sup>C. With PET both qualitative images and dynamic <sup>11</sup>C-tracer profiles were obtained visualising the movement of internal CO<sub>2</sub> in leaves whereas positron autoradiography provided detailed insights on tracer distribution in the leaves under different conditions.
- ◇ Second, upon illumination with photosynthetic radiation, conversion of xylem-transported CO<sub>2</sub> to sugars via woody tissue photosynthesis was unequivocally demonstrated rather than CO<sub>2</sub> accumulation within tissues. Therefore, illuminated and light-excluded branch segments were labelled with <sup>13</sup>C which were subsequently analysed by liquid chromatography-mass spectrometry.
- ◇ Third, the developed <sup>11</sup>C-labelling method for leaves in the first step was translated to be performed on branches. Visualisation of xylem-transported <sup>11</sup>C in branches was realised through application of positron autoradiography. Vast response of woody tissue photosynthesis was observed when branches were illuminated. Light-exclusion experiments and <sup>18</sup>F-experiments (with <sup>18</sup>F being a proxy for water) confirmed that CO<sub>2</sub> is stripped from the xylem sap to be assimilated by woody tissue photosynthesis.



- ◇ Fourth, dynamic PET measurements were performed of which the data was used for compartmental modelling to successfully reveal the dynamics of xylem-transported CO<sub>2</sub> within branches. Two main findings were put forward; (i) analysis of the PET images allowed direct estimation of the CO<sub>2</sub> transport speed, which has not been described so far. (ii) Compartmental modelling revealed that a great part of the internal CO<sub>2</sub> (i.e. 38 %) gets assimilated by woody tissue photosynthesis in young branches while only 12 % was outgassed to the atmosphere via efflux. The remaining part of 49 % was found to be transported upward with the sap.



S

SAMENVATTING



Het begrijpen en in kaart brengen van plant respiratie is van groot belang voor de aardwetenschappen en uiterst fundamenteel voor plant ecologie en fysiologie. Dit omdat de efflux van CO<sub>2</sub>, bewerkstelligd door plant respiratie processen, een betekenisvolle maar steeds onzekere component is voor het plant-, ecosysteem- en mondiaal koolstofbudget.

Vroeger werd aangenomen dat gerespireerd CO<sub>2</sub> vrijwel meteen diffundeerde naar de omgeving. Observaties over de laatste 20 jaar hebben echter aangetoond dat een grote hoeveelheid van het gerespireerde CO<sub>2</sub> in de boom achterblijft. Dit lokaal gerespireerd CO<sub>2</sub> kan een aanzienlijk hogere concentratie (algemeen tussen 3 en 10 % en in uitzonderlijke gevallen tot 26%) aannemen in vergelijking met de atmosferische CO<sub>2</sub> concentratie (~ 0.04%). Een toenemende kennis van de betrokken processen toonde aan dat een ruime hoeveelheid van desbetreffend CO<sub>2</sub> oplost in het xylemsap om vervolgens opwaarts getransporteerd te worden, weg van de plaats van opname. Een deel van het xyleem-getransporteerd CO<sub>2</sub> kan vervolgens ontsnappen naar de atmosfeer via efflux terwijl een ander deel geassimileerd kan worden door fotosynthetisch actieve cellen in houtachtig weefsel en bladeren. Desondanks de reeds verworven vooruitgang, kan ons inzicht over xyleem-getransporteerd CO<sub>2</sub> met betrekking tot respiratie verder uitgediept worden. Tot op heden blijft er namelijk een grote onzekerheid bestaan over het dynamisch lot op kleine spatiale en temporale schaal. Daarnaast werd de assimilatie van intern CO<sub>2</sub> door fotosynthese in houtachtige weefsels slechts aangenomen gezien de eigenlijke fixatie en omzetting naar suikers niet vastgelegd werd.

In deze doctoraatsthesis ligt de focus op het ontrafelen van de geheimen van xyleem-getransporteerd CO<sub>2</sub> door het dynamisch gedrag ervan op een submillimeter schaal te bestuderen. Dit werd mogelijk gemaakt door toepassing van twee technieken binnen de medische beeldvorming, namelijk positron autoradiografie en positron emissie tomografie (PET). Beide positron-gebaseerde technieken laten *in vivo* experimenten toe voor het bestuderen en in beeld brengen van biologische processen met een hoge spatiale resolutie. Daar waar deze technieken uitgebreid toegepast worden op klinisch en preklinisch gebied, rapporteren slechts enkele onderzoeksgroepen wereldwijd positron-gebaseerde studies, hetgeen gerelateerd kan zijn aan de complexiteit ervan. Gezien wij ervan overtuigd zijn dat deze technieken danig potentieel hebben in hun extensieve

bijdrage tot de plantwetenschappen, werd in deze doctoraatsthesis een uitgebreid overzicht gegeven met betrekking tot het ontwerpen en uitvoeren van positron-gebaseerde experimenten op planten. Hierbij lag de nadruk op het traceren van radioactief  $^{11}\text{CO}_2$  in PET hoewel ook de basis van positron autoradiografie voorzien werd.

Het onderzoek doorheen deze doctoraatsthesis werd uitgevoerd op 1-jarige varianten van populier, namelijk *Populus × canadensis* Moench "Robusta" and *Populus tremula* L.. Deze species zijn gekenmerkt door een snelle groei en een hoge natuurlijke chlorofylconcentratie in de bast, waardoor dit ideale kandidaten zijn voor het bestuderen van xyleem-getransporteerd  $\text{CO}_2$  in relatie tot fotosynthese in houtachtige weefsels. In dit onderzoek werden vier belangrijke stappen genomen voor het ontrafelen van de dynamica achter xyleem-getransporteerd  $\text{CO}_2$ :

- ◇ Ten eerste, werd de mogelijkheid tot het gebruik van zowel PET als positron autoradiografie getest voor het bestuderen van intern  $\text{CO}_2$  in bladeren. Hiertoe werd een methode ontwikkeld om plantweefsel te labelen met  $^{11}\text{CO}_2$  in een halfopen systeem. Labelen gebeurde door een aangereikte  $^{11}\text{CO}_2$ -oplossing te voorzien aan de petiool van afgeknipte bladeren. Teneinde een normale fotosynthetische activiteit te behouden werd in deze methode een continue luchtstroom voorzien aan de bladeren, rekening houdend met de gevaren van radioactief gasvormig  $^{11}\text{CO}_2$  dat eventueel kan vrijkomen als gas. Door het beïnvloeden van intern  $\text{CO}_2$  transport met behulp van licht exclusie of het beletten van transpiratie op bladniveau, werd aangetoond dat zowel PET als autoradiografie toelaten om het dynamisch gedrag van xyleem-getransporteerd  $\text{CO}_2$  te bestuderen. Het gebruik van PET leverde kwalitatieve beelden en dynamische  $^{11}\text{C}$ -tracer profielen op terwijl positron autoradiografie gedetailleerde inzichten aanbracht over de tracerverdeling in bladeren bij de verschillende behandelingen
- ◇ Ten tweede, door belichting met fotosynthetische straling werd de omzetting van xyleem-getransporteerd  $\text{CO}_2$  tot suikers in houtachtige weefsel ontgensprekelijk aangetoond. Hiertoe werden belichte en donkere takken gelabeld met  $^{13}\text{CO}_2$  om vervolgens geanalyseerd te worden met vloeistofchromatografie-massaspectro-metrie. In eerdere studies werd de assimilatie van  $\text{CO}_2$  in houtachtige weefsels namelijk nooit getest waardoor er

enkel aangenomen kon worden dat accumulatie van CO<sub>2</sub> in deze weefsels te wijten was aan fotosynthese.

- ◇ Ten derde, werd de ontwikkelde <sup>11</sup>C-labelingsmethode voor bladeren vanuit stap één aangepast voor het labelen van takken. Door gebruik van positron autoradiografie kon het xyleem-getransporteerd CO<sub>2</sub> gevisualiseerd worden. Bij belichting van de takken, werd een uitgesproken respons van fotosynthese in houtachtige weefsels waargenomen. Behandeling met licht-exclusie en <sup>18</sup>F-experimenten (met <sup>18</sup>F een proxy voor water) bevestigden dat CO<sub>2</sub> gestript werd van het xyleemsap om geassimileerd te worden door fotosynthese in houtachtige weefsels.
- ◇ Ten vierde, werden dynamische PET-metingen uitgevoerd. De bekomen data werd gebruikt in een compartimenteel model teneinde het dynamisch gedrag van xyleem-getransporteerd CO<sub>2</sub> in takken te ontrafelen. Twee hoofdbevindingen werden naar voor gebracht. Enerzijds liet analyse van de PET-beelden toe om op eenvoudige wijze de transportsnelheid van CO<sub>2</sub> te schatten, hetgeen tot op heden niet beschreven werd. Anderzijds bracht compartimentele modellering het inzicht dat een groot deel van het intern CO<sub>2</sub> (i.e. 38%) geassimileerd werd door fotosynthese in houtachtige weefsel van jonge takken, terwijl 12% in de omgeving terecht kwam door efflux. De overgebleven 49% van het intern CO<sub>2</sub> werd opwaarts getransporteerd met het sap.





CV

CURRICULUM VITAE



---

**Personalia**


---

Jens Mincke

°28/06/1990, 9620 Zottegem

📍 Meulesteedsesteenweg 251 @ Jens.Mincke@UGent.be 📞 +32 (0)498 49 70 88  
9000 Gent, Belgium

**Education**


---

2015-2019 PhD student at the Laboratory of Plant Ecology, Department of Plant and Crops, Faculty of Bioscience Engineering, Ghent University

*PhD thesis* Unravelling xylem-transported CO<sub>2</sub> dynamics in trees using positron emission tomography and autoradiography

*Promoters* Prof. dr. ir. Kathy Steppe  
Prof. dr. Stefaan Vandenberghe

2013–2015 Master of Science in Biomedical Engineering, Faculty of Engineering and Architecture, Ghent University and Vrije Universiteit Brussel

*Master thesis* *Development and characterization of a methacrylate-based polymer as potential implantable 'glucose-sensor-packaging'*

*Promoters* Prof. dr. Peter Dubruel,  
Prof. dr. Sandra Van Vlierberghe

2011–2013 Master of Science in Bioscience Engineering: Chemistry and Bioprocess Technology, Faculty of Bioscience Engineering, Ghent University

*Master thesis* *Synthese en enzymatische hydrolyse van cis-3-alkoxy-2-(cyaanmethyl)azetidinen*

*Promoters* Prof. dr. ir. Matthias D'hooghe  
Prof. dr. Tom Desmet

2008–2011 Bachelor of Science in Bioscience Engineering: Chemistry and Food Technology, Faculty of Bioscience Engineering, Ghent University

2002–2008 Secondary school: Science-Mathematics, Viso Cor Mariae, Brakel

### Additional education

---

- 2016–2019    Doctoral schools Ghent University
- Effective graphical Display
  - Training school on Plant Modelling
  - PET methodology: Experimental Design and Data Analysis (King's College London)
  - Introduction to R
  - Leadership Foundation
- 2019            Career Management
- Managing your career: mapping out your route to success (Vlerick experience days)
  - Job market for young researchers
  - Applying for a postdoctoral job
  - Grant writing day

### Teaching and tutoring activities

---

- 2018 – 2019            Member of reading committee of four master theses
- 2017 – 2019            Reviewer for international peer reviewed journals Tree Physiology and Functional Plant Biology
- Teaching practical sessions on Monte Carlo simulation & SPECT and CT of for the course Biomedical Imaging
- 2017 – 2018            Tutor of master thesis Klaas De Backer on *“Improved insights into carbon fertilization and drought in Populus tremula through medical imaging”*
- Teaching of a special topic *“Phloem”* and excursion (use of ecophysiological instruments) of the course Ecofysiologie
- 2016 – 2017            Tutor of master thesis Dheepashri Kannan on *“Investigation of stem photosynthesis by tracing internal <sup>11</sup>C-labelled CO<sub>2</sub> in tomato plants”*

---

**Grants and award**


---

- Apr 2019 Travel grant from the Scientific Research Committee (CWO, Faculty of Bioscience Engineering, Ghent University) for participating in European Geosciences Union (EGU) General Assembly 2019, Vienna, Austria.
- May 2017 Student award for best oral presentation awarded by the International Society for Horticultural Science (ISHS) at 10<sup>th</sup> International Workshop on Sap Flow, Fullerton, California, USA.
- Jan 2016 – Dec 2019 PhD grant for Strategic Basic Research from Research Foundation Flanders (FWO) for project “*Traceren van <sup>11</sup>C-gelabeld CO<sub>2</sub> transport in het xyleem van bomen: belang en bijdrage tot het koolstofmetabolisme*”
- Sep 2015 – Dec 2016 PhD grant from FWO granted to Kathy Steppe for project “*<sup>11</sup>C combined with advanced plant-based measures to unravel the plant-carbon dynamics in current and future climatic conditions*”

---

**International publications with peer review (A1)**


---

- L. Decuyper, N. Piens, **J. Mincke**, J. Bomon, B. De Schrijver, K. Mollet, K. De Winter, T. Desmet, M. D'hooghe, *A nitrilase-mediated entry to 4-carboxymethyl-β-lactams from chemically prepared 4-(cyanomethyl)azetidin-2-ones*, RSC Advances **2016**, 6, 54573–54579.
- M. Hubeau\*, **J. Mincke\***, C. Vanhove, J. Courtyn, S. Vandenberght, K. Steppe, *Plant-PET to investigate phloem vulnerability to drought in Populus tremula under changing climate regimes*, Tree Physiol. **2018**, 39, 211–221.
- M. Hubeau\*, **J. Mincke\***, C. Vanhove, A.P. Gorel, A. Fayolle, J. Epila, O. Leroux, S. Vandenberghe, K. Steppe, *<sup>11</sup>C-Autoradiographs to Image Phloem Loading*. Front. For. Glob. Chang. **2019a**, 2
- M. Hubeau, M.R. Thorpe, **J. Mincke**, J. Bloemen, I. Bauweraerts, P.E.H. Minchin, V. De Schepper, F. De Vos, C. Vanhove, S. Vandenberghe, K. Steppe, *High-resolution in vivo imaging of xylem-transported CO<sub>2</sub> in leaves based on real-time <sup>11</sup>C-tracing*. Front. For. Glob. Chang. **2019b**, 2.

\*Equally contributing first authors

### International proceedings with peer review (P1)

---

**J. Mincke**, M. Hubeau, J. Courty, B. Brans, C. Vanhove, S. Vandenberghe and K. Steppe, *Normalization of  $^{11}\text{C}$ -autoradiographic images for semi-quantitative analysis of woody tissue photosynthesis*. Acta Horticulturae **2018**, 35-42

### Oral presentations

---

**J. Mincke**, M. Hubeau, C. Vanhove, J. Courty, S. Vandenberghe & K. Steppe, *Medical imaging to the rescue in assessing phloem vulnerability to drought in Populus tremula under changing climate regimes*, presented at the EGU General Assembly 2019, Vienna, Austria, 7-12 April 2019

**J. Mincke**, M. Hubeau, C. Vanhove, J. Courty, S. Vandenberghe & K. Steppe, *Visualization of dynamics in woody tissue photosynthesis via positron autoradiography of xylem-transported  $^{11}\text{CO}_2$* , presented at the 10<sup>th</sup> International Workshop on Sap Flow, Fullerton, California, USA, 22-26 May 2017

### Posters

---

**J. Mincke**, M. Hubeau, C. Vanhove, J. Courty, S. Vandenberghe & K. Steppe, *Rising atmospheric  $\text{CO}_2$  levels: a holy grail for trees or not?*, presented at the EGU General Assembly 2019, Vienna, Austria, 7-12 April 2019

D. Kannan, **J. Mincke**, K. Steppe, S. Vandenberghe, *Investigation of stem photosynthesis by tracing internal  $^{11}\text{C}$ -labelled  $\text{CO}_2$  in plants*, presented at UGent-VUB Biomedical Industry Day, Ghent, Belgium, 15 March 2017 – awarded with prize for best poster



